CHAPTER-1

Introduction

1.1 Photovoltaic and renewable energy resources

Most of the energy utilized today comes from fossil fuels. According to statistics, the current global energy consumption is around 13 terawatts (TW) per year which has yet no limit and has crossed all limits. With this consumption rate, the reserves of oil, natural gas and coal (Fig. 1.1) will last only for 30, 60 and 200 years respectively. Unfortunately, the demand of energy will grow quickly and is forecast to reach a value of 30 TW by 2050 which means that the energy sources will deplete even sooner.

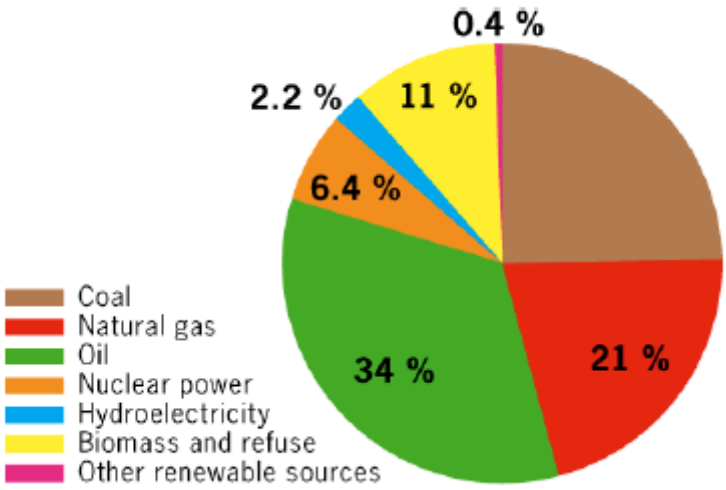

Figure 1.1 World – energy consumption using various energy resources

The biggest concern for the modern society is to find alternative energy sources before fossil fuels are depleted. Moreover, these fossil fuels are concerned with lot of negative impact on

our environment, particularly "Global Warming". Both nuclear power and solar power have the potential to provide huge amount of energy, but nuclear power is limited by mineral isotope conserves and safety concerns about nuclear reactions. It seems like solar energy would be the only energy source with such huge capacity of meeting with the increasing demand of energy in the long run. The sun rays supply the earth surface with ~125000 TW annually, which greatly exceeds the capacity of any energy resource on earth. The current annual global energy consumption only accounts for the amount of energy delivered to the earth by the sun in 1 hour. Therefore, solar energy has the potential to meet the energy demand of human society. However, the solar energy is quite unevenly distributed on the surface of the earth and efficient collection is still a technological challenge. The major strategies to utilize solar energy are to convert the incident sunlight into either electricity or chemical fuels. Two major techniques are available to generate electricity from sunlight. The technique involves direct conversion of incident photons into electricity, which can be achieved through device called photovoltaic (PV), or more commonly known as solar cells. Besides electricity generation, sunlight is also considered to be an energy source to provide chemical fuels .However, the substitution of fossil fuels by solar energy is still greatly limited by cost of energy conversion devices. The coal-based electricity gives us a bench mark cost value of $0.04/kWh ($0.67/W), while the cost of electricity for today's photovoltaic's is in the range of $0.25-$0.65/kWh ($3-$8/W). Undoubted, solar-based devices still need to improve significantly to compete with machines powered by fossil fuels.

1.2 Photovoltaic and Photovoltaic Cells

Photovoltaics (PV) comprise the technology to convert sunlight directly into electricity. The term "photo" means light and "voltaic," electricity. A photovoltaic (PV) cell, also known as

"solar cell," is a semiconductor device that generates electricity when light falls on it. Photovoltaic solar cells provide clean electrical energy because the solar energy is directly converted into electrical energy without emitting carbon dioxide. The solar energy is not limited, free of charge and distributed uniformly to all human beings.

1.3 Photovoltaic Effect

When sunlight strikes a PV cell, the photons of the absorbed sunlight dislodge the electrons from the atoms of the cell. The free electrons then move through the cell, creating and filling in holes in the cell. It is this movement of electrons and holes that generates electricity. The physical process in which a PV cell converts sunlight into electricity is known as the photovoltaic effect.

1.4 Working of photovoltaic cell/device

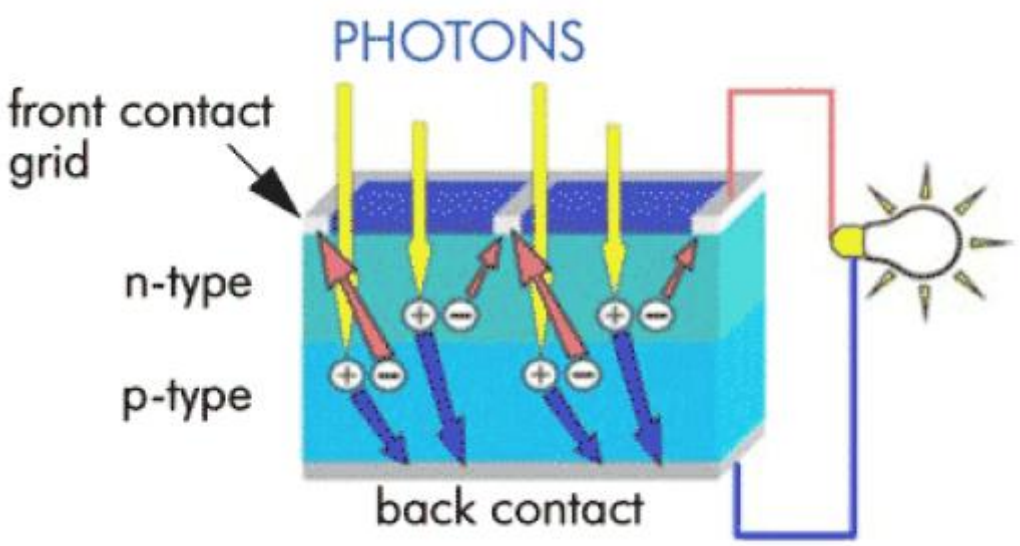

Figure 1.2 Working of a photovoltaic device

Solar energy conversion involves direct conversion of light energy from the Sun's rays into electricity. This occurs sequentially, firstly by the Generation of electrons followed by their transport inside a semiconductor material as positive and negative charges; or more precisely, as holes and electrons. The semiconductor material features two regions, one exhibiting excess of electrons, the other an electron deficit, referred to as n-type doped, and p-type doped respectively as shown in Fig. 1.2.

When the former is brought in contact with the latter, excess electrons from the n-doped region diffuses into p-doped region. The polarity of both the regions gets reversed. An electric field is thus set up between them, tending to force electrons back into the n-region and holes back into the p-region. This event sets up a p-n junction in the device.

By placing metallic contacts on n- and p- regions, a diode is obtained. When the junction is illuminated, photons having an energy equal to or higher than, the width of the forbidden band, or band gap, yield their energy to the atoms, each photon causing an electron to move around the material, thus giving rise to electron-hole pair. As the load is applied at the cell's terminals, electrons from the n-region migrate back and similarly holes migrate back to the p-region externally giving rise to a potential difference causing an electric current.

One single PV cell produces up to 2 watts of power, too small even for powering pocket calculators or wristwatches. To increase power output, many PV cells are connected together to form modules, which are further assembled into larger units called arrays. This modular nature of PV enables designers to build PV systems with various power output for different types of applications.

A complete PV system consists not only of PV modules, but also the "balance of system" or BOS - the support structures, wiring, storage, conversion devices, etc. i.e. everything else in a

PV system except the PV modules. Two major types of PV systems (Fig. 1.3) are available in the marketplace today: flat plate and concentrators. They can be distinguished as follows

Flat-plate PV Systems	Concentrators
• Flat-plate systems build the PV modules on a rigid and flat surface to capture sunlight. • Less complicated but employ a larger number of cells. • Able to focus even diffused sunlight.	• Concentrator systems use lenses to concentrate sunlight on the PV cells and increase the cell power output. • Use smaller areas of cells but require more sophisticated & expensive tracking systems. • Unable to focus diffused sunlight.

Figure 1.3 Comparison of Flat-plate and concentrator PV systems.

1.5 Types of PV cell materials

PV cells are made of semiconductor materials. The major types of materials are crystalline and thin films, which vary from each other in terms of light absorption efficiency, energy conversion efficiency, manufacturing technology and cost of production.

1.5.1 First Generation PV cells

First generation solar cells are the larger, silicon-based, photovoltaic cells that have, and still do, dominate the solar panel market. These solar cells, using silicon wafers, account for 86%

of the solar cell market. They are dominant due to their high efficiency but they have high manufacturing costs due to which alternatives are being sought for. First generation solar cells include the following PV materials:

1.5.1.1 Single-crystal silicon

Single-crystal silicon cells are the most common in the PV industry. The main technique for producing single-crystal silicon is the Czochralski (CZ) method as shown in Fig. 1.4. High-purity polycrystalline is melted in a quartz crucible. A single-crystal silicon seed is dipped into this molten mass of polycrystalline. As the seed is pulled slowly from the melt, a single-crystal ingot is formed. The ingots are then sawed into thin wafers about 200-400 micrometers thick (1 micrometer = 1/1,000,000 meter). The thin wafers are then polished, doped, coated, interconnected and assembled into modules and arrays. Single-crystal silicon has a uniform molecular structure.

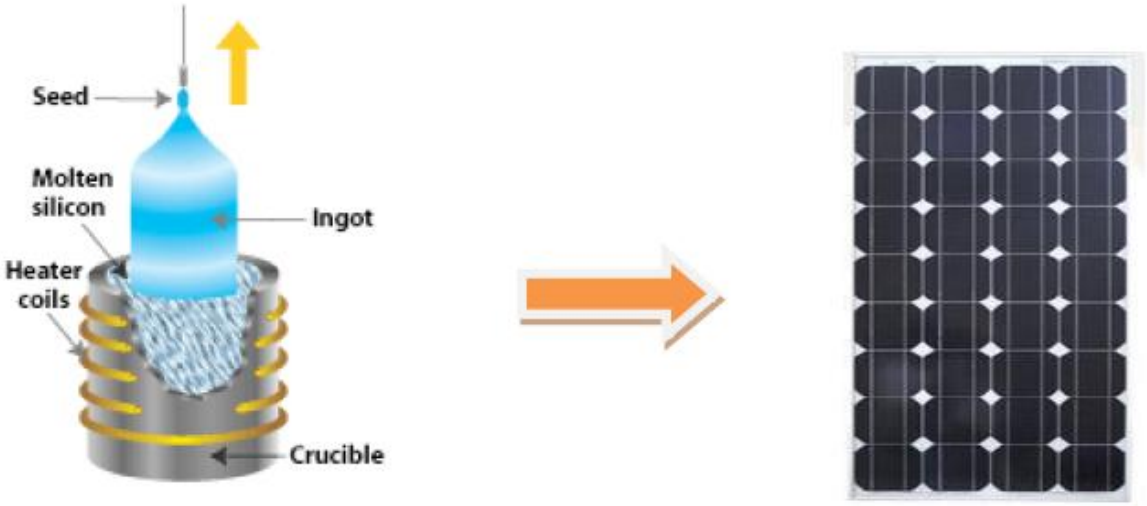

Figure 1.4 Schematics of the formation of Single-crystal silicon using Czochralski method

Compared to non-crystalline materials, the high uniformity of monocrystalline Si wafer exhibits higher energy conversion efficiency, i.e., the ratio of electric power produced by the cell to the amount of available sunlight power. The higher PV cells conversion efficiency, the more electricity it generates for a given area of exposure to the sunlight. The conversion efficiency for single-silicon commercial modules ranges between 15-20%. Not only are they energy efficient, single-silicon modules are highly reliable for outdoor power applications. But due to their time consuming procedures & high manufacturing costs where about half of the manufacturing cost comes from wafering, and costly batch process in which ingots are cut into thin wafers with a thickness about 200 micrometers thick, other alternatives are being sought after. Moreover, If the wafers are too thin, the entire wafer will break in wafering and subsequent processing. Due to this thickness requirement, a PV cell requires a significant amount of raw silicon and half of this expensive material is lost as sawdust in wafering.

1.5.1.2 Polycrystalline silicon

Polycrystalline Silicon comprises of small grains of single-crystal silicon. These PV cells are less energy efficient than single-crystalline silicon PV cells. The grain boundaries in polycrystalline silicon hinder the flow of electrons and reduce the power output of the cell.The energy conversion efficiency for a commercial module made of polycrystalline silicon ranges between 10 to 14%. A common approach to produce polycrystalline silicon PV cells is to slice thin wafers from blocks of cast polycrystalline silicon. Another more advanced approach is the “ribbon growth” method in which silicon is grown directly as thin ribbons or sheets with the approach thickness for making PV cells. Since no sawing is needed, the manufacturing cost is lower. The most commercially developed ribbon growth

approach is EFG (edge-defined film-fed growth). Compared to single-crystalline silicon, polycrystalline silicon material is stronger and can be cut into one-third the thickness of single-crystal material. It also has slightly lower wafer cost and less strict growth requirements. However, their lower manufacturing cost is offset by the lower cell efficiency.

1.5.1.3 Gallium Arsenide (GaAs)

A compound semiconductor made of two elements: gallium (Ga) and arsenic (As), GaAs has a crystal structure similar to that of silicon. An advantage of GaAs is that it has high level of light absorptivity. To absorb the same amount of sunlight, GaAs requires only a layer of few micrometers thick while crystalline silicon requires a wafer of about 200-300 micrometers thick. Also, GaAs has much higher energy conversion efficiency than crystal silicon, reaching about 25 to 30%. Its high resistance to heat makes it an ideal choice for concentrator systems in which cell temperatures are high. GaAs is also popular in space applications where strong resistance radiation damage and high cell efficiency are required. The biggest drawback of GaAs PV cells is the high cost of the single-crystal substrate that GaAs is grown on. Therefore it is most often used in concentrator systems where only a small area of GaAs cells is needed.

1.5.2 Second Generation Solar Cells

Second generation cells, also called thin-film solar cells, and are significantly cheaper to produce than first generation cells but have lower efficiencies. The great advantage of second generation, thin-film solar cells, along with low cost, is their flexibility. Thin-film technology has spurred lightweight, aesthetically pleasing solar innovations such as solar shingles and solar panels that can be rolled out onto a roof or other surface. It has been predicted that

second generation cells will dominate the residential solar market as new, higher-efficiency cells are researched and produced.

Thin Film Materials

In a thin-film PV cell, a thin semiconductor layer of PV materials is deposited on low-cost supporting layer such as glass, metal or plastic foil. Since thin-film materials have higher light absorptivity than crystalline materials, the deposited layer of PV materials is extremely thin (Fig. 1.5); from a few micrometers to even less than a micrometer (a single amorphous cell can be as thin as 0.3 micrometers). Thinner layers of material yield significant cost saving. Also, the deposition techniques in which PV materials are sprayed directly onto glass or metal substrate are cheaper. So the manufacturing process is faster, using up less energy mass production is made easier than the ingot-growth approach of crystalline silicon. However, thin film PV cells suffer from poor cell conversion efficiency due to non-single crystal structure, requiring larger array areas and increasing area-related costs such as mountings.

Figure 1.5 Flexible Polycrystalline silicon

1.5.2.1 Amorphous Silicon (a-Si)

a-Si is used mostly in consumer electronic products which require lower power output and cost of production. It has been the dominant thin-film PV material since it was first discovered in 1974. Amorphous silicon is a non-crystalline form of silicon i.e. its silicon atoms are disordered in structure. A significant advantage of a-Si is its high absorptivity, about 40 times higher than that of single-crystal silicon. Therefore only a thin layer of a-Si is sufficient for making PV cells (about 1 μm thick as compared to 200 or more μm thick for crystalline silicon cells). Also, a-Si can be deposited on various low-cost substrates, including steel, glass and plastic, and the manufacturing process requires lower temperatures and thus less energy. So the total material costs and manufacturing costs are lower per unit area as compared to those of crystalline silicon cells. Despite the promising economic advantages, a-Si still has two major roadblocks to overcome which can be listed as follows:

(1) Low cell energy conversion efficiency, ranging between 5-9%, and
(2) Outdoor reliability problem in which the efficiency degrades within a few months of exposure to sunlight, losing about 10 to 15%.

1.5.2.2 Cadmium Telluride (CdTe)

As a polycrystalline semiconductor compound made of cadmium and tellurium, CdTe has a high light absorptive level -- only about a micrometer thick can absorb 90% of the solar spectrum. Another advantage is that it is relatively easy and cheap to manufacture by processes such as high-rate evaporation, spraying or screen printing. The conversion efficiency for a CdTe commercial module is about 7%, similar to that of a-Si. The major drawbacks are the instability of cell and module performance. Cadmium is even having

toxicity issues. Although very little cadmium is used in CdTe modules, extra precautions have to be taken in manufacturing process.

1.5.2.3 Copper Indium Gallium Sulphide (CIGS), Copper Indium Sulphide CIS

A polycrystalline semiconductor compound of copper, indium, gallium and sulphur, CIGS/CIS has been one of the major research areas in the thin film industry. The reason for it to receive so much attention is that CIGS/CIS has the highest "research" energy conversion efficiency of nearly 19.9% is not only the best among all the existing thin film materials, but also came close to research efficiency of the polycrystalline silicon PV cells. Being able to deliver such high energy conversion efficiency without suffering from the outdoor degradation problem, CIGS/CIS has demonstrated that thin film PV cells are a viable and competitive choice for the solar industry in the future. CIGS/CIS is also one of the most light-absorbent semiconductors -- 0.5 micrometers can absorb 90% of the solar spectrum. CIGS/CIS is an efficient but complex material. Its complexity makes it difficult to manufacture. Also, safety issues might be another concern in the manufacturing process as it involves hydrogen sulphide, an extremely toxic gas.

1.5.2.4 Copper Zinc Tin Sulphide (CZTS)

Copper zinc tin sulfide (**CZTS**) is a quaternary semiconducting compound which has received increasing interest since the late 2000's for applications in solar cells. The class of related materials includes other I_2-II-IV-VI_4 such as copper zinc tin selenide (CZTSe) and the sulfur-selenium alloy CZTSSe. CZTS offers favourable optical and electronic properties similar to CIGS (copper indium gallium selenide) making it well suited for use as a thin film

solar cell absorber layer, but unlike CIGS(or other thin films such as CdTe), CZTS is composed of only abundant and non-toxic elements. Concerns with the price and availability of indium in CIGS and tellurium in CdTe, as well as toxicity of cadmium have been a large motivator to search for alternative thin film solar cell materials. Recent material improvements for CZTS have increased efficiency to just above 10% in laboratory cells, but more work will be needed for successful commercialization.

CZTS (Cu_2ZnSnS_4) offers to alleviate the material bottlenecks present in CIGS (and CdTe). CZTS is similar to the chalcopyrite structure of CIGS but uses only earth-abundant elements. Raw material costs are ~5x less than CIGS and estimates of global material reserves (for Cu, Sn, Zn and S) suggest we could produce enough energy to power the world with only 0.1% of the available raw material resources. In addition, CZTS doesn't have any concerns with toxicity unlike CdTe and to a lesser extent CIGS (although selenium is sometimes alloyed with CZTS and CdS is sometimes used as the n-type junction partner).

1.5.3 Third Generation Solar Cells

Third generation solar cells are the cutting edge of solar technology. Still in the research phase, third generation cells have moved well beyond silicon-based cells. Generally, third generation cells include solar cells that do not need the p-n junction necessary in traditional semiconductor, silicon-based cells. Third generation contains a wide range of potential solar innovations including polymer solar cells, nano-crystalline cells, and dye-sensitized solar cells.

1.5.3.1 Dye Sensitized Solar Cells

Invented in their high efficiency version in the early 1990s, dye-sensitised solar cells (DSCs) entered the global market in 2007 with the first commercial modules based on this versatile, hybrid (organic-inorganic) technology. The 6-7% efficiency of the first modules is a result of their good performance in diffuse light conditions, allowing for the production of electricity both under cloudy conditions and indoors.

These low-cost solar cells are manufactured by highly productive roll-to-roll printing methods over rigid or flexible substrates affording modules coloured in widely different tones (Fig. 1.6). These render DSC to be a photovoltaic technology particularly well suited for BIPV applications and for electrification in developing countries. These cells can surely give shorter pay-back times than other conventional and new PV technologies.

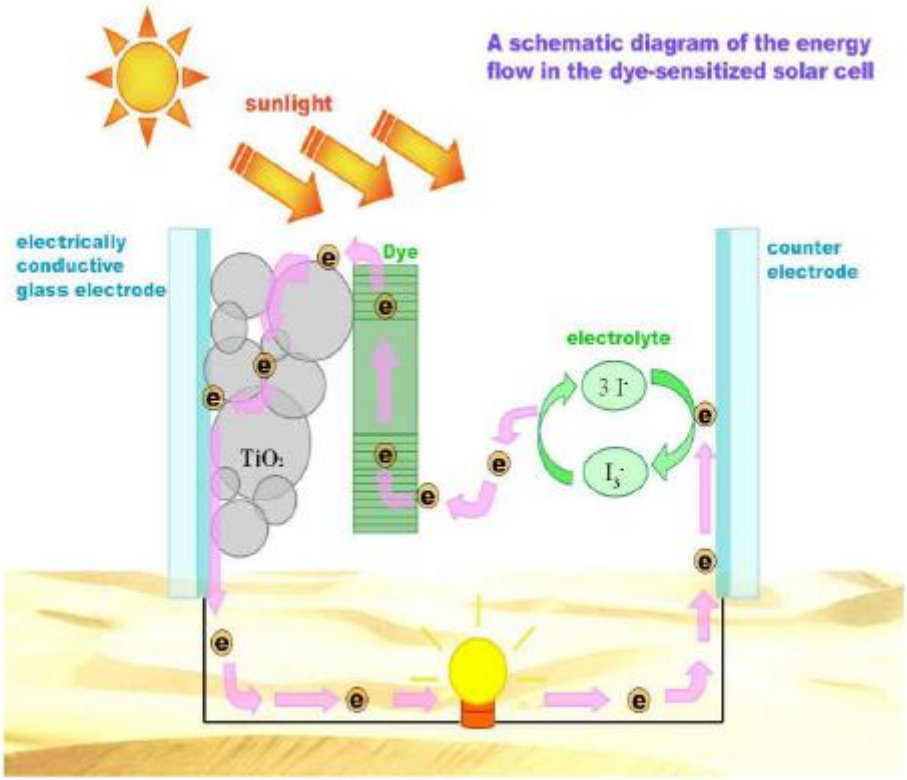

Figure 1.6 Schematics of a Dye-Sensitized Solar Cell

One of the major points of DSC technology is the technology's relative insensitivity to impurities. This, along with the intrinsically low cost of the constituents, allows for production costs much lower than those of conventional crystalline silicon. Advantages of the technology include its low cost - the materials are inexpensive, abundant and innocuous ease of production; transparency; and compared to Si-based cells, DSCs boast easy bifacial configuration - advantageous for diffuse light, and colour, which can be varied by selection of the dye, including invisible PV cells based on near-IR sensitizers. Furthermore, contrary to Si-based modules, the performance of dye PV modules increases with temperature. Hence, the global energy production of these modules is significantly higher than that of amorphous Si-based modules, despite their lower 5% efficiency.

1.5.3.2 Quantum-Dot Sensitized Solar Cells

Quantum dot sensitized solar cells (QDSCs) constitute one of the most promising approaches to third generation solar cells.[1-4] The intrinsic attractive properties of QDs (tunable band gap, high extinction coefficients,[5,6] and large intrinsic dipole organic dyes as alternative light absorbers. Moreover, the demonstration of multiple exciton generation by impact ionization in colloidal QDs could push the thermodynamic efficiency limit of these devices up to 44% instead of the current 31% of the Schokley-Queisser detailed balance limit. Although the efficiencies of QDSCs lag behind those of dye-sensitized solar cells (DSCs)[11] (DSC currently exceeds 11% at 1 sun illumination, QD-sensitized nanostructured solar cells are attracting increasing attention among researchers and are progressing very rapidly.

1.5.3.3 Organic Solar Cells

Solar cells based on conjugated polymers have been a rapidly developing area of research during the last decade. Since photoexcitations in conjugated polymers show diffusion lengths

of only around 5–20 nm, the structure of the polymeric nanophase within the photoactive layer has a large influence on the device properties and the solar power conversion efficiency. Considerably less effort and production energy is necessary if organic semiconductors are used because of simpler processing at much lower temperatures (20-200^{0}C) than the inorganic cells.

Another interesting alternative to inorganic cells is given by the semiconducting polymers, which combine the optoelectronic properties of conventional semiconductors with the excellent mechanical and processing properties of polymeric i.e. "plastic" materials. These can be processed from solution at room-temperature onto flexible substrates using simple and cheaper deposition methods like spin or blade coating.

1.5.4 Fourth-Generation Solar Cells

Much progress for the past decade has been made towards hybrid solar cells with advanced PV properties. An alternative to pure organic PVs is the class of organic-inorganic hybrid solar cells where hetero-junction is formed between inorganic semiconductors and organic compounds (small molecules, oligomers, polymers, carbon nanotubes). An advantage of hybrid PVs over organics PVs lies in the high carrier mobility of the semiconductor and the light absorption at longer wavelengths than for organic compounds. On the other hand, the existence of the organic component allows hybrid solar cells to be superior over conventional semiconducting PVs in terms of cost efficiency, scalable wet processing, the variety of organic materials (mismatch between inorganic components can be minimized or prevented), light weight, and flexibility. Moreover, the recent progress in advanced semiconducting nanostructures in combination with organic nanomaterials [e.g.,fullerenes and carbon

nanotubes (CNTs)] opens new opportunities to overcome the 10% barrier of conversion efficiency for hybrid solar cells in the near future.

1.6 Aim of Project

Aim of this project is to synthesize binary (Cadmium Sulphide,CdS ; Zinc Sulphide,ZnS),ternary (Cadmium Lead Sulphide,CdPbS),quaternary(Copper Zinc Tin Sulphide,CZTS) chalcogenides compounds semiconducting quantum dots of different sizes using single molecule precursors and form composites with polymer,P3HT to perform detailed study regarding solar cells applications.

The synthesized nanoparticles and nanocomposites were investigated using various characterization techniques-UV, PL, XRD, SEM, TEM, and TRF which are discussed in sufficient detail in upcoming chapters. All the used characterization techniques are studied in detail in chapter-2.

1.7 Conjugated Polymer P3HT

Poly (3-hexylthiophene) (P3HT) is a π-conjugated polymer, which in its undoped, pristine state is a semiconductor or insulator. It has attracted great interest because of its high carrier mobility, mechanical strength,efficiency, thermal stability, and compatibility with fabrication process. The essential structural characteristic of all conjugated polymers is their quasi-infinite π system extending over a large number of recurring monomer units, which results in materials with directional conductivity, strongest along the axis of the chain [12].

The alkyl side chains of the P3HT are aligned in a periodic structure as shown in Fig. 1.7. Functions of side chains are to make materials soluble in organic solvents like chlorobenzene, toluene, and chloroform and to modify electro-optical properties of the materials [12].It is

one of the most promising polymers in the fabrication and study regarding application of solar cell.

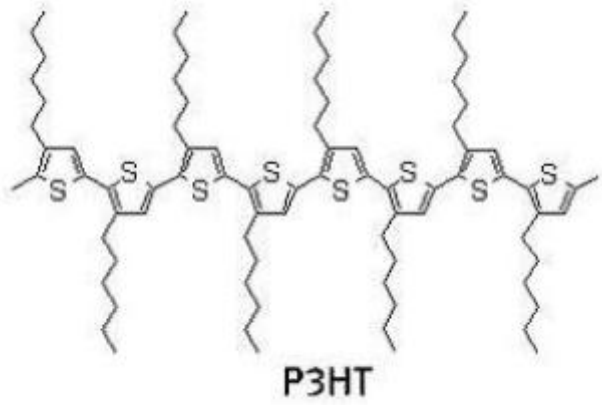

Figure 1.7 Chemical Structure of P3HT [13]

1.8 Novelty of project work-Single Molecule Precursor

It is now well known that the nature of the precursor will decide the quality of the nanocrystals produced. In the case of dithiocarbamates subtle changes in the substituents at the nitrogen atom can markedly affect the thermal decomposition of the precursor.

Our research has focused on a rational approach using single molecular-precursors to develop methods of nanoparticle synthesis. There are a number of potential advantages of using single-molecular precursors over other existing methods:

- Single source routes avoid the need for volatile, sometimes toxic and/or pyrophoric precursors.

- Some II-VI and III-V nanoparticles are air sensitive. All precursor synthesis is carried out under anaerobic conditions, with the resulting precursors being air and moisture stable.
- One involatile precursor is involved, purification of which is easier than that of two or more volatile precursors, and hence there is less chance of the incorporation of impurities into the nanoparticles.
- Low temperature deposition routes are possible.
- Although there are theoretical models predicting the optical properties of semiconductor nanoparticles, the properties of nanoparticles obtained by new synthetic routes are sometimes hard to anticipate and may lead to particles with unique and unanticipated, but useful, properties.

1.9 Scope and method of study

The objective of this research was the development of new chemical routes for the synthesis of nanoscale metal sulphides. This was accomplished by investigating a family of materials known as **Xanthates.** It was determined that metal xanthates were ideal single – source precursors for target product. A wide variety of metal centres and alkyl substituent were easily incorporated into xanthate species yielding new precursors with tunable properties. A systematic characterization of the various precursors by means of thermo gravimetric analysis indicated that the decomposition temperatures required to convert the xanthates into nanometric sulphides is lower than that of any other known single precursor. Detailed analyses were performed on the precursors and the sulphides using such tools as UV, PL, XRD, SEM, and TEM.

The major goal to develop metal sulphide materials with enhanced, tunable electrical and optical properties was envisioned.

1.10 Conclusion

Metal sulphide nanoparticles were obtained from different xanthate based precursors possessing distinctive properties such as ultra high surface area and intense emissivity. Cadmium, copper, silver, nickel, zinc and other metal sulphide quantum dots were easily prepared with little or no external stabilizing agents required since the thermal decomposition by-products of the xanthates act as capping agents. The xanthate precursors can also be used to prepare ternary sulphides such as $CuInS_2$ and $CuIn_{1-x}Ga_xS_2$.Succinctly; metal xanthate complexes are versatile compounds that can generate a wide array of useful metal sulphide semiconductor nanoparticles.

1.11 References:

1. Goetzberger, Adolf., Knobloch, Joachim., and Voss, Bernhard. Crystalline Silicon Solar Cells. England: John Wiley & Sons, 1998.
2. Howes, Ruth. and Fainberg, Anthony. The Energy Sourcebook: A Guide to Technology, Resources, and Policy. American Institute of Physics, New York. 1991.
3. Johansson, Thomas B., Kelly, Henry., Reddy, Amulya K.N. and Williams, Robert H. eds. Renewable Energy: Sources for Fuels and Electricity . Washing DC: Island Press, 1993.
4. Partain, Larry D, ed. Solar Cells and Their Applications. New York: John Wiley & Sons, 1995.
5. Zweibel, Ken. Harnessing Solar Power: The Photovoltaics Challenge. New York: Plenum Press,1990.

6. Zweibel, Ken. "Thin Films: Past, Present, Future." Progress in Photovoltaics 3, no. 5 (Sept/Oct1995, revised April 1997).
7. Gunes, S.; Neugebauer, H.; Sariciftci, N.S. Conjugated polymer-based organic solar cells. Chem.Rev. 2007, 107, 1324–1338.
8. Boucle, J.; Ravirajan, P.; Nelson, J. Hybrid polymer-metal oxide thin films for Photovoltaic applications. J. Mater. Chem. 2007, 17, 3141–3153.
9. Gledhill, S.E.; Scott, B.; Gregg, B.A. Organic and nano-structured composite photovoltaics: An overview. J. Mater. Res. 2005, 20, 3167–3179.
10. McGehee, M.D. Nanostructured organic-inorganic hybrid solar cells. Mater. Res. Soc. Bull. 2009, 34, 95–100.
11. Garnier, F. Hybrid organic-on-inorganic photovoltaic devices. J. Opt. A: Pure Appl. Opt. 2002, 4, S247–S251.
12. S. S. Sunkavalli, "Solar cell thesis", Master thesis, ODU, Norfolk, VA.
13. sunatech Inc. Product Catalog, biobay, Suzhou Industrial Park, Suzhou, China 2008.

CHAPTER-2

Experimental and Characterization Techniques

This chapter deals with the various experimental aspects of different semiconducting nanoparticles which include methods of preparation and synthesis strategy involved. We discuss the details pertaining to the various instruments used in our work for characterizing the nanomaterials. The working principle of these techniques along with their design and other specifications are explained. We also justify their usage in the reported work.

2.1 Route Adopted – Colloidal synthesis

Colloidal semiconductor nanocrystals are synthesized from precursor compounds dissolved in solutions, much like traditional chemical processes. The synthesis of colloidal quantum dots is based on a three-component system composed of: precursors, organic surfactants, and solvents. When heating a reaction medium to a sufficiently high temperature, the precursors chemically transform into monomers. Once the monomers reach a high enough supersaturation level, the nanocrystal growth starts with a nucleation process. The temperature during the growth process is one of the critical factors in determining optimal conditions for the nanocrystal growth. It must be high enough to allow for rearrangement and annealing of atoms during the synthesis process while being low enough to promote crystal growth. Another critical factor that has to be stringently controlled during nanocrystal growth is the monomer concentration. The growth process of nanocrystals can occur in two different regimes, “focusing” and “defocusing”. At high monomer concentrations, the critical size (the size where nanocrystals neither grow nor shrink) is relatively small, resulting in growth of

nearly all particles. In this regime, smaller particles grow faster than large ones (since larger crystals need more atoms to grow than small crystals) resulting in "focusing" of the size distribution to yield nearly monodisperse particles. The size focusing is optimal when the monomer concentration is kept such that the average nanocrystal size present is always slightly larger than the critical size. When the monomer concentration is depleted during growth, the critical size becomes larger than the average size present, and the distribution "defocuses" as a result of Ostwald ripening.

2.2 Synthetic Strategy

Synthesis of colloidal nanoparticles is succeeded by some synthetic strategies which were studied in order to understand the reaction mechanism. The general reaction mechanism can be described as follows:

Stage I: Nucleation

The very first step in the synthesis of nanoparticles is the nucleation of the particles. Successful nucleation is an indication of whether the reaction in question is appropriate for the formation of nanoparticles. For a monodisperse sample, the nucleation event must be well separated in time from the growth step, which generally means that nucleation must occur on a short time scale, of the order of a fraction of a second. In contrast, if nucleation is spread out in time such that nucleation and growth overlap, different nucleation sites will undergo growth of different durations, resulting in a broad size distribution. An effective way to achieve separation of nucleation from growth is the use of a method of injecting suitable precursors into the solvent at high temperature such that nucleation occurs immediately on contact with the hot solvent. Semiconductor nanoparticles include the need for prolonged

reaction times to overcome the high reaction barriers and the need for annealing at high temperature to achieve better crystallinity of the nanoparticles.

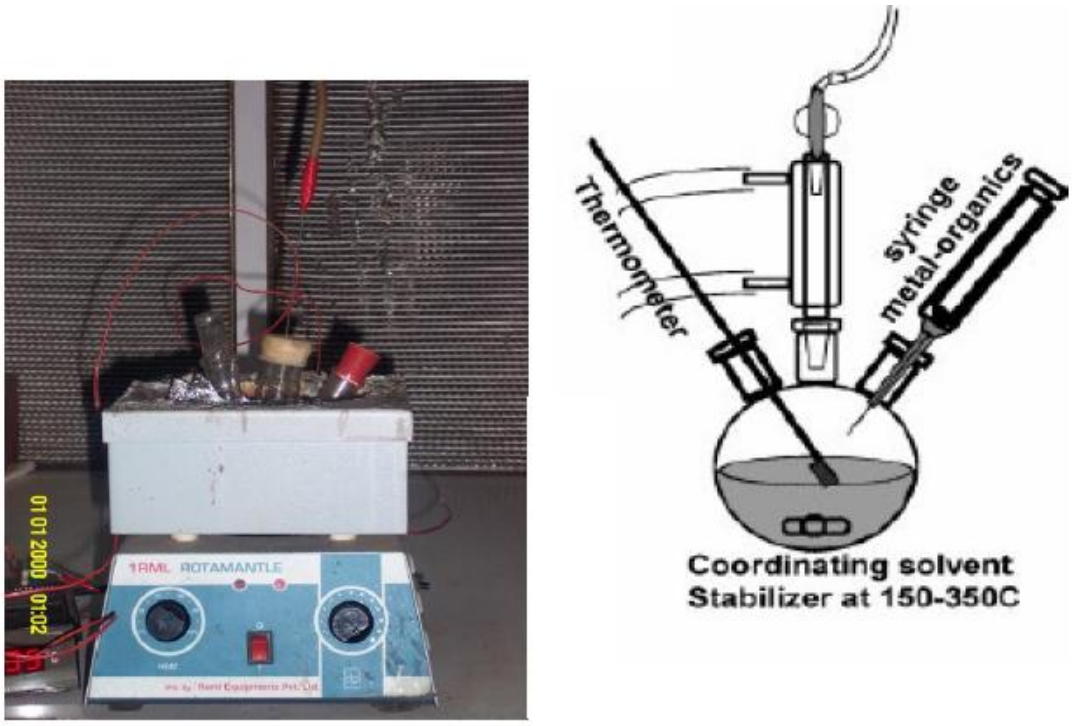

Figure 2.1 Schematic of the apparatus used during synthesis of different nanoparticles.

Stage II: Growth

The next stage in the nanoparticle synthesis is the growth of the particles. As with nucleation, intermediate species and the growing particle must stay in solution throughout the process. Growth is completed when the reagents are consumed, although additional high-temperature annealing time may be needed to obtain good crystallinity. Under prolonged high-temperature annealing, the possibility of Ostwald ripening arises – an undesired mechanism that will broaden the size distribution. Growth can also be effectively quenched by cooling the reaction mixture. This concept is based on the existence of a critical size that depends on the reaction conditions (concentration of reactants, temperature, solvent etc.). Above the

critical size, growth rate decreases with increased size, leading to a narrowing or focusing of the size distribution, while below the critical size, defocusing results because the growth rate of smaller particles is slower than that of the bigger particles. To achieve a narrow distribution, conditions should be optimized so that during growth the reaction remains within size focusing conditions.

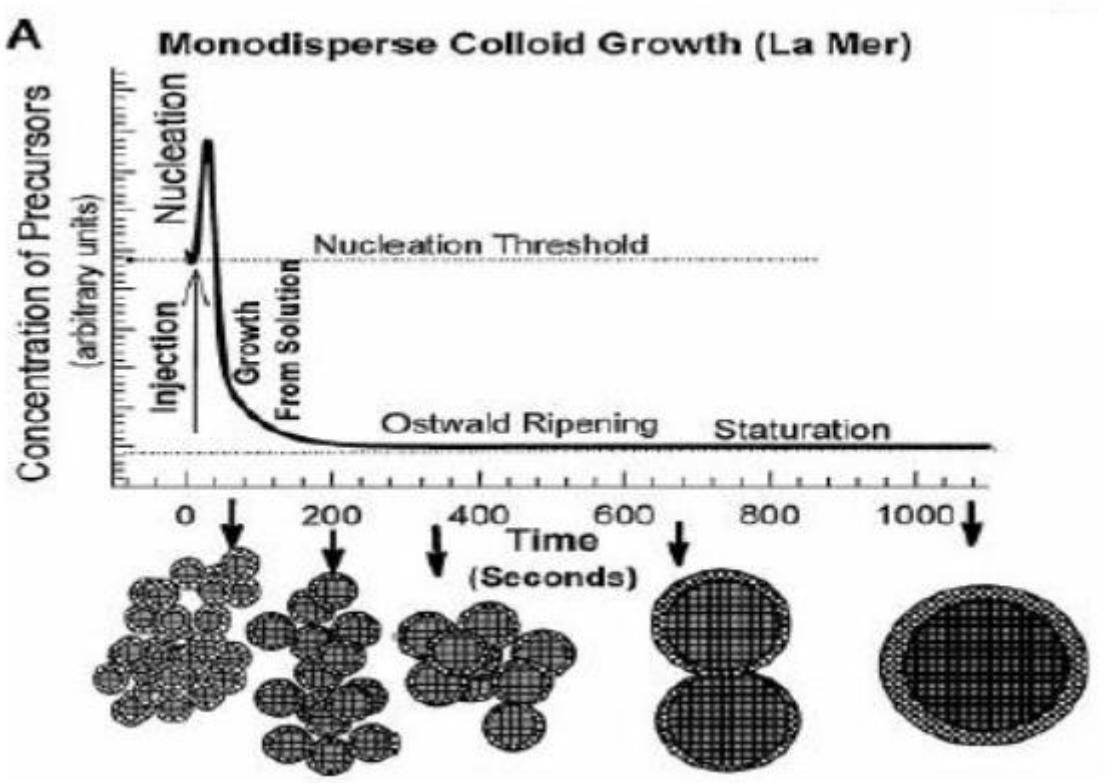

Figure 2.2 La Mer Diagram for the mechanism of colloidal nanoparticles

Surface Passivation: An additional critical issue for high quality nanoparticles is the passivation of the surface. During the synthesis, surface passivation helps to control the growth of the nanoparticles (Fig. 2.2), prevents agglomeration and fusing of particles, and provides for the solubility of the nanoparticles in common solvents. Solvation is important

not only for the nanoparticles, but also for the reactants and intermediates. Surface passivation is achieved by using an organic molecule to coordinate or bond to the nanoparticles surface. Most commonly, this organic molecule is the solvent for the reaction. This strategy benefits from having the capping molecule in huge excess and from having a common solvation medium for the reactants, intermediates, and nanoparticles. Capping groups typically contain an electron-rich donating group such as phosphine oxides, phosphines, amines, or thiols and behave as a Lewis base, which coordinates to the electron-poor Lewis acid-like metal of the semiconductor such as cadmium or indium. This coordination passivates the dangling orbitals at the nanoparticles surface, preventing further growth or agglomeration. The other end of the ligand imparts solubility to the nanoparticles by giving the particle a hydrophilic or hydrophobic surface. Surface passivation plays an important role not only during the synthesis. It can also be used to further derivatize the surface of the particles, providing additional chemical control to attach nanoparticles to a surface, to electrodes, to other nanoparticles, and to biomolecules . Because of the relatively weak coordination bonds of most surface-capping groups, these molecules can easily be exchanged after the initial synthesis. Many of the properties of nanoparticles, notably photoluminescence, are sensitive to the surface passivation, and manipulation of the surface-capping groups can be used to tune these properties. Improvement of the size distribution after the synthesis is also a widely used strategy for achieving monodisperse samples. Size-selective precipitation is commonly applied to obtain fractions of nanoparticles with improved size distribution from a given reaction. The method is based on the size-dependent solubility of the nanoparticles, which can be used to destabilize the dispersion of the large particles first. This is achieved by adding controlled amounts of a non-solvent to the solution of particles, thereby leading to precipitation of the large nanoparticles, which can be then

separated by either filtration or centrifugation. Such steps can be carried out consecutively to obtain a sequence of nanoparticles fractions with smaller and smaller diameters. A similar procedure may in principle be applied yet again to each fraction to further narrow the size distribution. While the precise chemical mechanisms of nanoparticles syntheses have not been investigated, several general comments can be made regarding the effect of the reaction mechanism on the nanoparticles product. To accomplish the ideal nucleation event discussed above, the reaction needs to be rapid and complete. These requirements suggest simple mechanisms using reagents with low barriers to reaction.

2.3 General description of characterization techniques used

The materials synthesized were characterized using Ultra violet(UV) absorption, Photoluminescence (PL),X-Ray diffraction (XRD),Scanning electron microscope (SEM), Transmission electron microscope(TEM),Fourier transform infra red (FTIR) and Time resolved florescence(TRF) spectroscopy .Optical properties are characterized by using UV 1800 SHIMADZU UV SPECTROPHOTOMETER and Photoluminescence measurement was carried out at room temperature using a home-assembled system developed at NPL.TRF measurements are recorded using Edinburgh Laser induspectrom Fls920 (wave length 480 pulse width 93.9).Structural and morphological properties are determined by using XRD done by using Rigaku Miniflex-II diffractometer (Cu Kα =1.54A°), TEM was carried out using a JEM-2100F(GEOL electron microscope) 200Kv and SEM was carried out by using (SEM, Zeiss EV MA-10).(FTIR) spectra was recorded with a single beam Perkin Elmer instrument (Spectrum BX-500) FT-IR Model spectrophotometer.

2.3.1 Optical Characterization

2.3.1.1 Theory of UV-Vis absorption spectra:

Optical spectroscopy is one of the powerful tools for the characterization of nanomaterials, in general and semiconductor nanocrystallites in particular. The absorption of ultraviolet/visible radiation by a molecule leads to transitions among the electronic energy levels of the molecule, and for this reason optical spectroscopy is alternately known as electronic spectroscopy. An absorption spectrum is a plot of the changes in absorption intensity against wavelength. The energy transition E1→ E2 corresponds to the absorption of energy exactly equivalent to the energy of wavelength absorbed (Fig.2.3).

$$\Delta E=(E_2-E_1)=hc/\lambda=h\upsilon$$

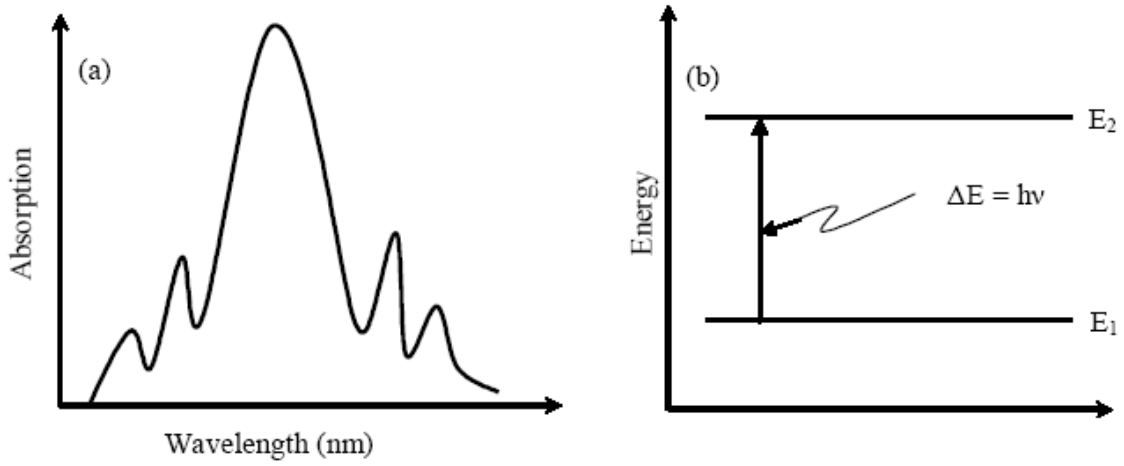

Figure 2.3 (a) A typical absorption spectrum (b) absorption involving two energy states E1 and E2.

A molecule can only absorb a particular frequency, if there exists, within the molecule an energy transition of magnitude $\Delta E = h\upsilon$. Wavelength range of the radiation absorbed for UV-Visible spectroscopy is 190- 800 nm (190-400nm for UV and 400-800nm for visible) which basically causes the changes in the electronic energy levels within the molecules. Practically

we would be concerned with the absorptions above 200nm because below 200nm oxygen present in the air begins to absorb strongly. The region below 200nm is required for studying bond energies, etc. and therefore, usually referred as the vacuum ultraviolet. With reduction in the particle size characteristic of materials a shift in the absorption edge can occur. The shift is usually to shorter wavelength and, therefore, known as blue shift. The theory of size dependent energy gap changes is explained by effective mass approximation. In case of semiconductors, particle size can be calculated by Brus equation.

$$\Delta E = \frac{\hbar^2 \pi^2}{2R^2}\left[\frac{1}{me} + \frac{1}{mh}\right] - \frac{1.8e^2}{\epsilon R} + \textit{polarisation energy}$$

Where,

ΔE=Difference of band gap of bulk and nano sized particle,

R= Radius of the particle,

me=Effective mass of electron,

mh=Effective mass of hole.

e = electronic charge

Theory

Laws of Light Absorption – Beer's and Lambert's Laws

These two early empirical laws govern the absorption of light by molecules. Beer's law relates the absorption to the concentration of absorbing solute, and Lambert's law relates the total absorption to the optical path length. In other words the Beer-Lambert law (also called the Beer-Lambert-Bouguer law or simply Beer's law is the linear relationship between absorbance and concentration of an absorber of electromagnetic radiation. The general Beer-Lambert law is usually written as

$$A = a_\lambda \times b \times c$$

Where, A is the measured absorbance, a_λ is a wavelength-dependent absorptivity coefficient,b is the path length, and c is the analyte concentration. When working in concentration units of molarity, the Beer-Lambert law can be written as:

$$A = \varepsilon_\lambda \times b \times c$$

Where, ε_λ is the wavelength-dependent molar absorptivity coefficient with units of $M^{-1}cm^{-1}$. The λ subscript is often dropped with the understanding that a value for ε is for a specific wavelength. If multiple species that absorb light at a given wavelength are present in a sample, the total absorbance at that wavelength is the sum due to all absorbers:

$$A = (\varepsilon_1 \times b \times c_1) + (\varepsilon_2 \times b \times c_2) + ...$$

Experimental measurements are usually made in terms of transmittance (T),

$$T = \frac{P}{P_0}$$

which is defined as:

where P is the power of light after it passes through the sample and Po is the initial light power. The relation between A and T is:

$$A = -\log(T) = -\log\left[\frac{P}{P_0}\right]$$

Fig. 2.4 shows the case of absorption of light through an optical filter and includes other processes that decrease the transmittance such as surface reflectance and scattering. The linearity of the Beer-Lambert law is limited by chemical and instrumental factors.

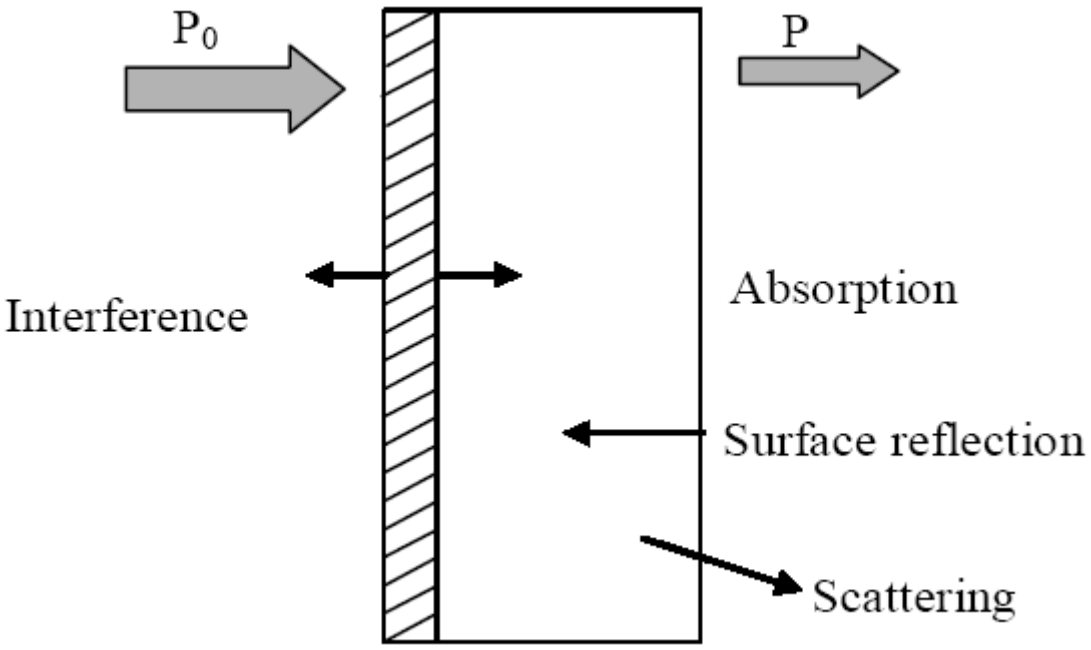

Figure 2.4 Various processes involved during the interaction of light with an optical Filter

Utility of UV-Visible Spectroscopy for Nanomaterials

An idea about the optical properties of any material can be obtained by its UV-Visible spectroscopy. The information about the changes in electronic energy levels within the molecule can thus be deduced. Researchers active in the field of nanomaterials have been employing the potential of UV-Visible spectroscopy for the investigation of band gap properties, particle size estimation and particle size distribution and so on. UV-Visible spectrum of any nanomaterial is different from its bulk counterpart. Band gap, for example,of

nanoscale material is greater than those in the corresponding bulk material. The reason being quantum confinement effects, which dominate in the case of nanomaterials. Generally a blue shift of band gap is observed in the case of nanomaterials. Moreover, we can have an idea about the size distribution of nanostructures depending upon the nature of peak, shoulder or edge. For example, smaller is the peak width; narrower is the size distribution of nanoparticles and vice versa. In our work, we have extensively used UV-Visible spectroscopy to characterize the semiconductor nanostructures to understand the change in band gap and band structure due to quantum mechanical confinement.

Instrumental Details

Basically the modern UV-Visible spectrometer consists of a light source, double beams (reference and sample beams), a monochromator, a detector and amplification and recording devices. Schematic layout of an UV-Visible Spectrometer has been depicted in Fig. 2.5. UV light (λ<400nm) can be detected on photographic film or in a photoelectric cell. The source usually incorporates a tungsten filament lamp for wavelengths greater than 375nm, a deuterium lamp for values below that, and a solenoid-operated mirror, which automatically deflects light from either one as the machine scans through the wavelengths. The detector is usually a photomultiplier (photomultiplier R-928 in our case), and the ratio of reference beam to sample beam intensities (I_0/I) is fed to a pen recorder (the optical null technique is not used). The recorder trace is invariably absorbance (A) against wavelength (λ) and photometric recording range for absorbance is 4 ~ 5 abs in the instrument used by us.

For the present study of nanomaterials, we have used the model UV-1800 UV-Visible spectrophotometer manufactured by Shimadzu Corporation, Kyoto, Japan. This spectrometer is operational at room temperature. Photometric system in this instrument is a double beam, direct ratio-measuring system employing the dynode feed-back method. With summing

feedback system, negative absorbance or more than 100% transmittance/reflectance can be accurately measured. The allowed wavelength range for this machine is 190-1100nm (effective scanning range 190-900nm). The halogen lamp for visible region and deuterium lamp for UV region are built in. Typically the deuterium lamp acts as a source for 190nm to light source switching wavelength and the halogen lamp ranges from light source switching wavelength to 900nm. For data acquisition we have normally selected a slit width of 1.0nm while the chosen value of sampling interval is 0.1nm. Resolution of this instrument is 0.1nm.A photograph of Spectrophotometer used is shown in Fig. 2.6.

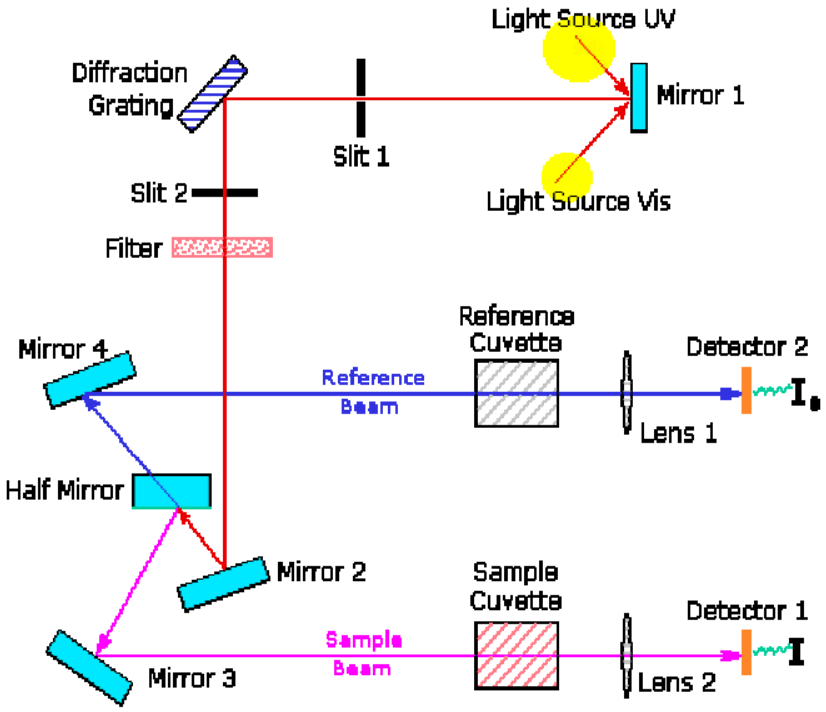

Figure 2.5 Schematic layout of an UV-Visible spectrometer

Figure 2.6 Photograph of a spectrophotometer

Samples Used and Their Preparation

Both colloidal suspensions and powder samples of nanomaterials were characterized by the UV-Visible spectrophotometer. For liquid solutions, quartz cuvettes of path length 1cm were used as the sample keeping cells. Utmost care was exercised, while cleaning the cells. The optical surfaces of the cell are never touched by hand. The cuvettes are cleaned with DI water and acetone. These are wiped with soft tissues dipped in methanol. For advanced cleaning, we carried out the entire cleaning procedure inside an ultrasonic bath. Sonication helps in scrubbing-off the firmly stuck dirt on the surface of cuvettes. In order to avoid the saturation of absorption intensity, we have usually acquired the UV-visible spectra for dilute solutions.

2.3.1.2 Photoluminescence Measurements

Photoluminescence (PL) spectroscopy is one of the most robust tools to study optical properties of semiconductors. A wealth of literature is available on the luminescent behaviour and band structure of semiconductor nanostructures. Optical properties of a material arise due to various transitions occurring within its band structure and can be elucidated with the help of a PL study.

Theory

A typical PL experiment in semiconductor can be divided into three stages: Firstly, the sample is excited from ground state, which is a completely filled valence band (VB) to the empty conduction band (CB). Energy pumped for excitation is $\hbar\omega$ pump. The laser creates electron-hole pairs due to a transfer of electrons from VB into CB. Secondly, the non-equilibrium electron and hole distributions tend to relax into the ground state. The initial intraband relaxation is caused by energy transfer to the crystal lattice, i.e. a step by step excitation of lattice vibration. Finally, the electron-hole pair recombines accompanied by the emission of light which is a photoluminescence process (Fig. 2.7)

Due to attractive Coulomb interaction between the charge carriers, the emission does not only contain contributions from states at or above the fundamental energy gap (Egap) but also sharp discrete lines (transitions) just below Egap, which originates from bound excitonic states.

Utility of PL Spectroscopy for Nanomaterials

The technique of photoluminescence (PL) has become a standard tool for obtaining information on the nature of nanostructures such as quantum dots. In bulk materials the luminescence often resembles a standard direct absorption spectrum, so there is little

advantage in studying the details of both. High photon excitation energies above the band gap can be most effective for luminescence studies of bulk materials, but it has been found that for the case of nanoparticles the efficiency of luminescence decreases at high incoming photon energies. Non radiative relaxation pathways can short-circuit the luminescence at these high energies, and it is of interest to investigate the nature of these pathways.

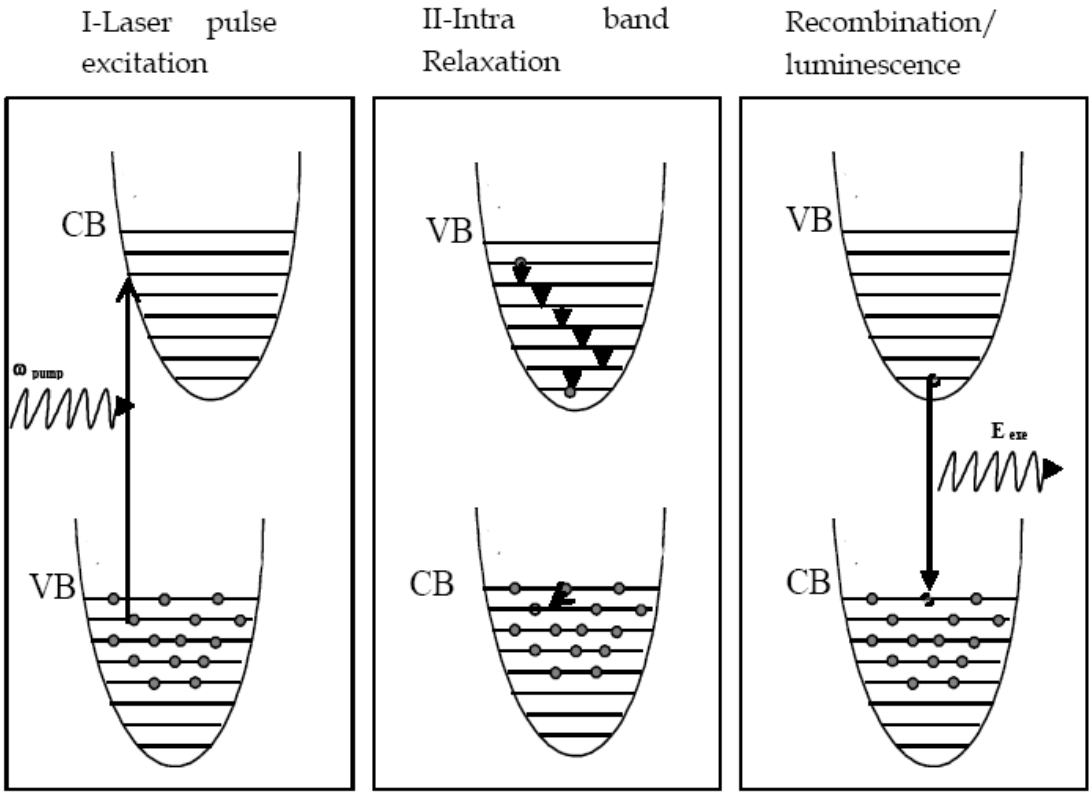

Figure 2.7 Sketch of the basic processes involved in a typical luminescence experiment in optically excited semiconductors

Photoluminescence is used for:

(i)Band Gap Determination

The most common radiative transition in semiconductors is between states in the conduction and valence bands, with the energy difference being known as the band gap. Band gap determination is particularly useful when working with new compound semiconductors.

(ii) Impurity Levels and Defect Detection

Radiative transitions in semiconductors also involve localized defect levels. The photoluminescence energy associated with these levels can be used to identify specific defects, and the amount of photoluminescence can be used to determine their concentration.

(iii) Recombination Mechanisms

The return to equilibrium, also known as "recombination," can involve both radiative and non-radiative processes. The amount of photoluminescence and its dependence on the level of photo-excitation and temperature are directly related to the dominant recombination process. Analysis of photoluminescence helps to understand the underlying physics of the recombination mechanism.

(iv) Material Quality

In general, non-radiative processes are associated with localized defect levels, whose presence is detrimental to material quality and subsequent device performance. Thus, material quality can be measured by quantifying the amount of radiative recombination.

Instrumental Details

PL is a static process in which input energy for excitation is fixed and output is varied i.e. response (PL emission intensity) is recorded for all available range of λ. The PL was measured using a home assembled system (Fig. 2.8), consisting of a two stage

monochromator, a photomultiplier tube (PMT) with a lock-in amplifier for PL detection, and an Ar^+ ion laser operating at 488 nm and 5mW (corresponding to 0.125 Wcm^{-2}) for excitation in all measurements. An optical chopper and a lock-in amplifier were employed to lock the whole system at a particular frequency. The entire system was automated with a desktop computer and an interface card was used for interfacing the experiment with the computer.

Figure 2.8 Home assembled PL system at NPL Delhi.

PL Quenching

Luminescence quenching refers to any process that decreases the luminescence intensity of a sample. There are two basic types of quenching: static and dynamic or (collisional). Both types require an interaction between the fluorophore and quencher. In the case of dynamic quenching, the quencher must diffuse to the fluorophore during the lifetime of the excited

state. Upon contact, the fluorophore returns to the ground state without emission of a photon. In the case of static quenching, a complex forms between the fluorophore and the quencher, and this complex is nonfluorescent. The formation of this complex does not rely upon the population of the excited state. In the simplest case of collisional quenching, the following relation, called the Stern-Volmer equation, hold

$$I_0/I = 1+ Ksv[Q]$$

Where, Io and I are the fluorescence intensities observed in the absence and presence, respectively, of quencher, [Q] is the quencher concentration, and Ksv is the Stern–Volmer quenching constant. In the simplest case, then a plot of Io/I Vs [Q] should yield a straight line with a slope equal to K_{sv}.

Samples Used and Their Preparation

Samples used for PL experiments are the same as those prepared for UV-Vis experiments (Refer UV-Vis Absorbance sample preparation section: 2.3.1.1).

2.3.1.3 Time Resolved Photoluminescence

The time-resolved photoluminescence (TRPL) technique is a contactless method to characterize recombination and transport in photovoltaic materials. The typical image of TRPL is shown in Fig. 2.9. TRPL is measured by exciting luminescence from a sample with a pulsed light source and then measuring the subsequent decay in photoluminescence (PL) as a function of time. A wide variety of experimental configurations can accomplish this. Most experiments excite the sample with a pulsed laser source and detect the PL with a photodiode, streak camera, or photomultiplier tube (PMT) set up for up-conversion or single-photon

counting. The system response time, wavelength range, sensitivity, operational difficulty and cost vary widely for each configuration. We most often use the single-photon counting technique. In this technique, the laser pulse is split into two beams with a beam splitter. The first beam triggers a time-amplitude converter (TAC) to start ramping up a voltage. The second beam excites PL from the sample. Some of the PL is passed through a long pass filter and monochromator onto a PMT. The first emitted photon to be detected by the PMT sends a stop signal to the TAC, and the TAC voltage is read and stored by a pulse height analyzer. The experiment is repeated at the repetition rate of the laser, typically 250,000 times per second with our new laser system. The optical system is configured so that a single photon is detected on the order of once every 200 pulses. Given these statistics, after a collection time on the order of 10 minutes, a histogram with on the order of 106 photon counts vs. time is generated that corresponds to the PL decay of the sample. The advantages of this technique are that, with appropriate electronics, the system response time is on the order of 30 ps to 100 ps, the sensitivity is excellent, and experimental versatility and sample throughput are fairly high. With this system, LMD group studied the PL decay of CdTe, CIGS, GaAs, InGaAsP, GaInP, GaAsN, GaInAsN, GaNP, GaInN, amorphous Si, carbon nanotubes, III-V quantum dots, and measured lifetimes ranging from tens of picoseconds to tens of microseconds. Indirect bandgap, such as Ge and Si, do not emit enough light to be suitable for TRPL.

The FLSP 900 is a complete fluorescence laboratory in a single instrument. It combines together with phosphorescence spectra and lifetime capabilities.

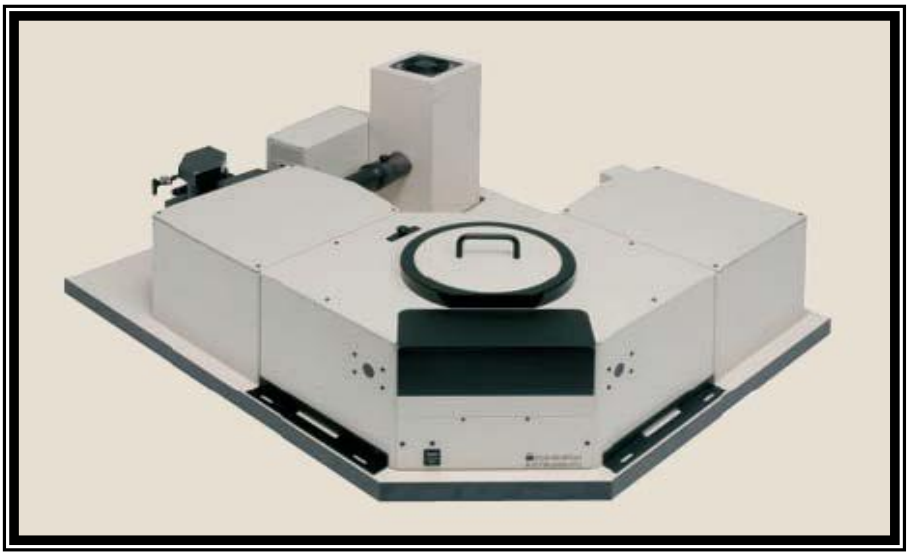

Figure 2.9 Combined steady state and Lifetime Spectrometer Model no.FLSP 900(Edinburg)

2.3.2 Structural and morphological characterization

2.3.2.1 X-ray Diffraction

X-ray diffraction (XRD) is a versatile, non-destructive analytical technique for identification and quantitative determination of the various crystalline forms, known as "phases" of compounds present in powdered and solid samples. The result of an XRD measure is a XRD pattern or diffractogram, showing phases present (peak positions), phase concentrations (peak heights), amorphous content (background bump) and crystallite size/strain (peak widths).

Identification is achieved by comparing the diffractogram obtained from an unknown sample with an internationally recognized database containing reference patterns called JCPDS.

Theory

A crystal lattice is a regular 3-dimensional distribution of atoms in space. These are arranged so that they form a series of parallel planes separated from one another by a distance d, which varies according to the nature of the material. For any crystal, planes exist in a number of different orientations, each with its own specific d-spacing.

When a monochromatic X-ray beam with wavelength λ is incident on lattice planes in a crystal at an angle θ, diffraction occurs only when the distance travelled by the rays reflected from successive planes differ by a complete number n of wavelengths. By varying the angle θ, the Bragg's law ($n\lambda = 2d \sin\theta$) (Fig. 2.10) conditions are satisfied by different d-spacing in polycrystalline materials.

Plotting the angular positions and intensities of the resultant diffraction peaks produces a pattern which is characteristic of the sample. Where a mixture of different phases is present, the diffractogram is formed by addition of the individual patterns.

Utility of XRD for Nanomaterials

Many structural properties of the nanostructures such as crystalline phase, particle size and structure evolution in Bragg planes, macroscopic stress/strain etc. can be revealed with the help of XRD. But here we shall mention few aspects directly relevant to our work.

Crystal identification:

A new methods has been attempted to prepare nanomaterials therefore it is important to identify these materials with the help of XRD data we can check the amorphous or crystalline nature of the newly formed material. If the prepared material is crystalline, we can determine

its basic lattice structure (e.g. cubic or hexagonal etc.) by indexing its lattice planes. One can also determine the changes in various lattice parameters of a particular bulk and nanosized material.

Crystallite Size:

A perfect crystal would extend in all directions to infinity, so we can say that no crystal is perfect due to its finite size. This deviation from perfect crystallinity leads to a broadening of the diffraction peaks. However, above a certain size (100-500 nm) this type of broadening is negligible.

Scherrer (1918) first observed that small crystallite size could give rise to line broadening. He derived a well- known equation for relating the crystallite size to the broadening, which is called Debye-Scherrer Formula.

$$Dv = \frac{k\lambda}{\beta Cos\,\theta}$$

Where, the symbols represent the following parameters:

Dv = Volume weighted crystallite size. D is the "average" dimension of the crystallites normal to the reflecting planes. We call it "average" because the x-ray beam irradiates a large number of crystallites, so that the value of D obtained represents the mean value of the actual size distribution present.

λ = wavelength of the radiation.

k = Scherrer constant. k varies from 0.89 to 1, but for most cases, is close to 1

β = the integral breadth of a reflection (in radians 2θ) located at 2θ commonly considered as the full width at half maxima (FWHM) in radians for a certain peak position 2θ. Value of Scherrer constant used at NPL is 0.89.

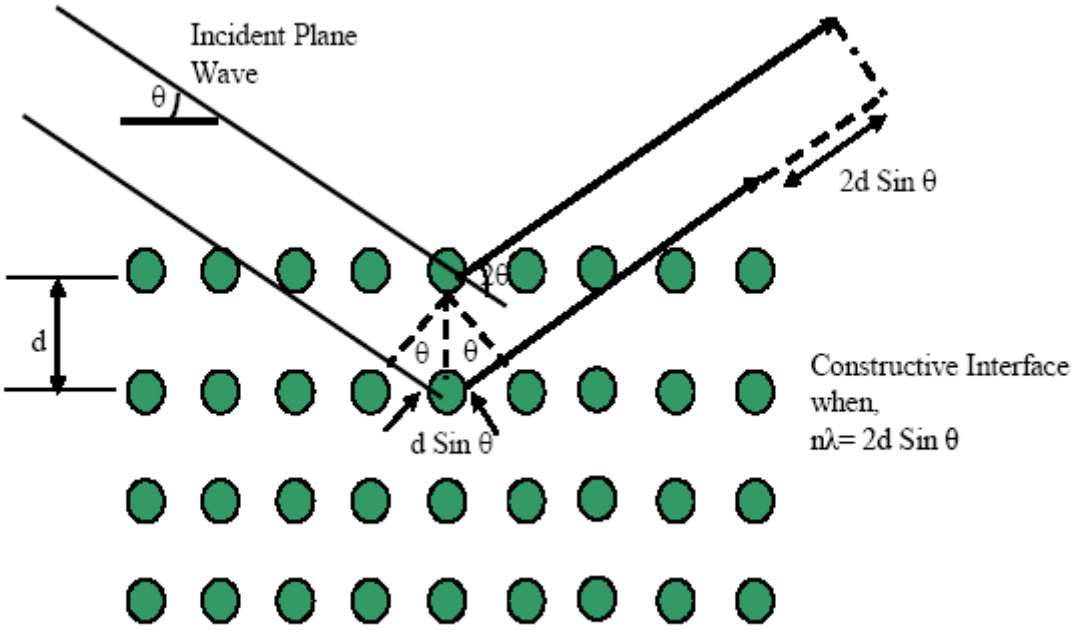

Figure 2.10 Schematic diagram showing Bragg diffraction from a set of planes

Crystallite size is a measure of the size of a coherently diffracting domain. Due to the presence of polycrystalline aggregates, crystallite size is not generally the same thing as particle size. When crystallites are less than approximately 100 nm in size, appreciable broadening in the x-ray diffraction lines will occur. These regions may, in fact, correspond to the actual size of the particles. At other times, however, these regions form "domains" in a larger particle and may be a distinguishing and important feature. In either case, the observed line broadening can be used to estimate the average size. In the simplest case where the

particles are stress-free, the size is estimated from a single diffraction peak. But in cases where stress may be present, a more robust method involving several diffraction peaks is required.

Instrumental Details

In an X-ray experiment, diffracted intensity is recorded as a function of the diffracted angle. All the reported XRD scans were taken on a_Rigaku Miniflex-II diffractometer (Cu Kα =1.54A°) from a rotating anode x-ray generator operating at 40kV (generator tension) and 30mA (generator current). A CPS 120 detector with Si (a= 0.543088nm) was used as an internal standard to record the patterns. Data has been collected normally at the scan rate of 2°-3° per minute keeping both incident and diffraction beam anti-scatter slit fixed at 1° with slit angle 1°. X-Ray diffractometer at NPL is shown in Fig. 2.11.

Samples Used and Their Preparation

All the diffractograms reported are for thin film samples. Normally we have made thin films on glass substrate from colloidal suspension of nanoparticles by the spin coating procedure. In this method we deposit the drops of the suspension with the help of a micropipette on a clean glass substrate which is slowly spinning. Spin motion of substrate considerably helps in uniform distribution of particles and prevents agglomeration of nanoparticles. Drops are deposited at a regular interval in order to obtain a uniform film. XRD patterns are recorded only when the sample is completely dry.

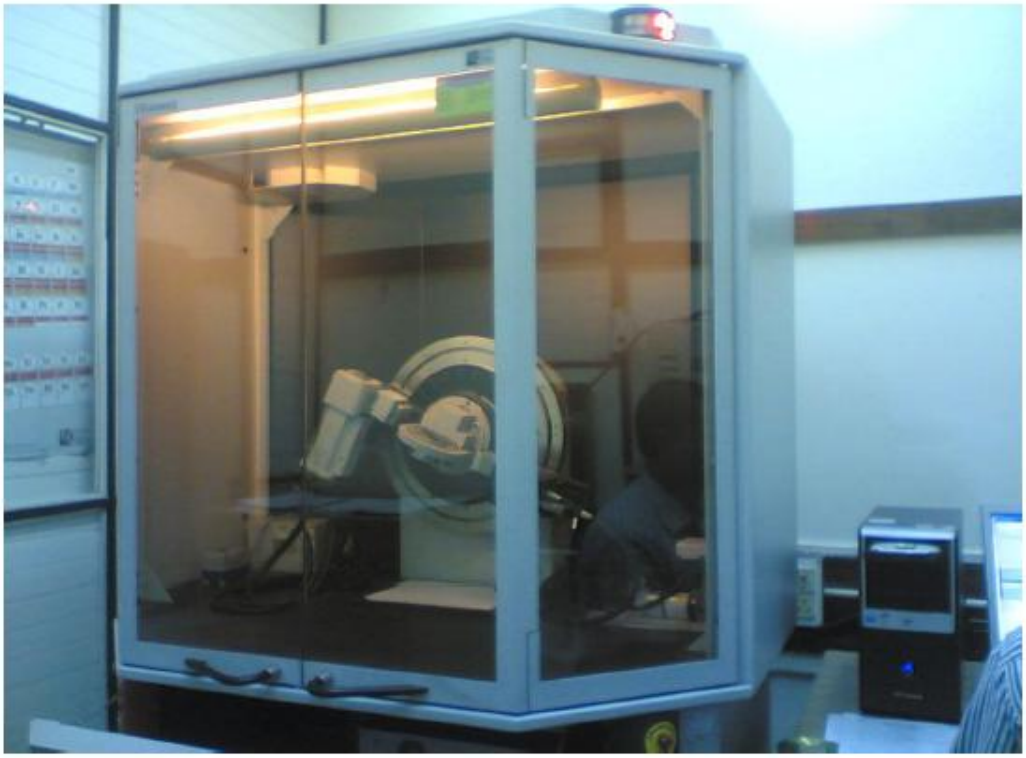

Figure 2.11 Siemens D-500 X-Ray diffractometer at NPL

2.3.2.2 Theory of Scanning Electron Microscopy

Scanning electron microscopy (SEM) is a powerful and popular technique for imaging the surfaces of almost any material with a resolution down to about 1 nm. The scanning electron microscope (SEM) uses a focused beam of high-energy electrons to generate a variety of signals at the surface of solid specimens. It utilizes the secondary electrons (SEs) and backscattered electrons (BSEs) being emitted from different areas of the specimen (as shown in Fig.2.12) as well as the trajectories they take in relation to the location of the detector. The signals that derive from electron sample interactions reveal information about the sample including its size, shape, external morphology (texture), of the three dimensional samples. The SEM is also capable of performing analyses of selected point locations on the sample,

this approach is especially useful in qualitatively or semi-quantitatively determining chemical compositions (using EDS), crystalline structure, and crystal orientations (using EBSD). The design and function of the SEM is very similar to the EPMA, and considerable overlap in capabilities exists between the two instruments.

The image resolution offered by SEM depends not only on the property of the electron probe, but also on the interaction of the electron probe with the specimen. Interaction of an incident electron beam with the specimen produces secondary electrons, with energies typically smaller than 50 eV, the emission efficiency of which sensitively depends on surface geometry, surface chemical characteristics and bulk chemical composition. The SEM has a large depth of field, which allows a large amount of the sample to be in focus at one time and produces an image that is a good representation of the three-dimensional sample.

The combination of higher magnification, larger depth of field, greater resolution, compositional and crystallographic information makes the SEM one of the most heavily used instruments in academic/national lab research areas and industry.

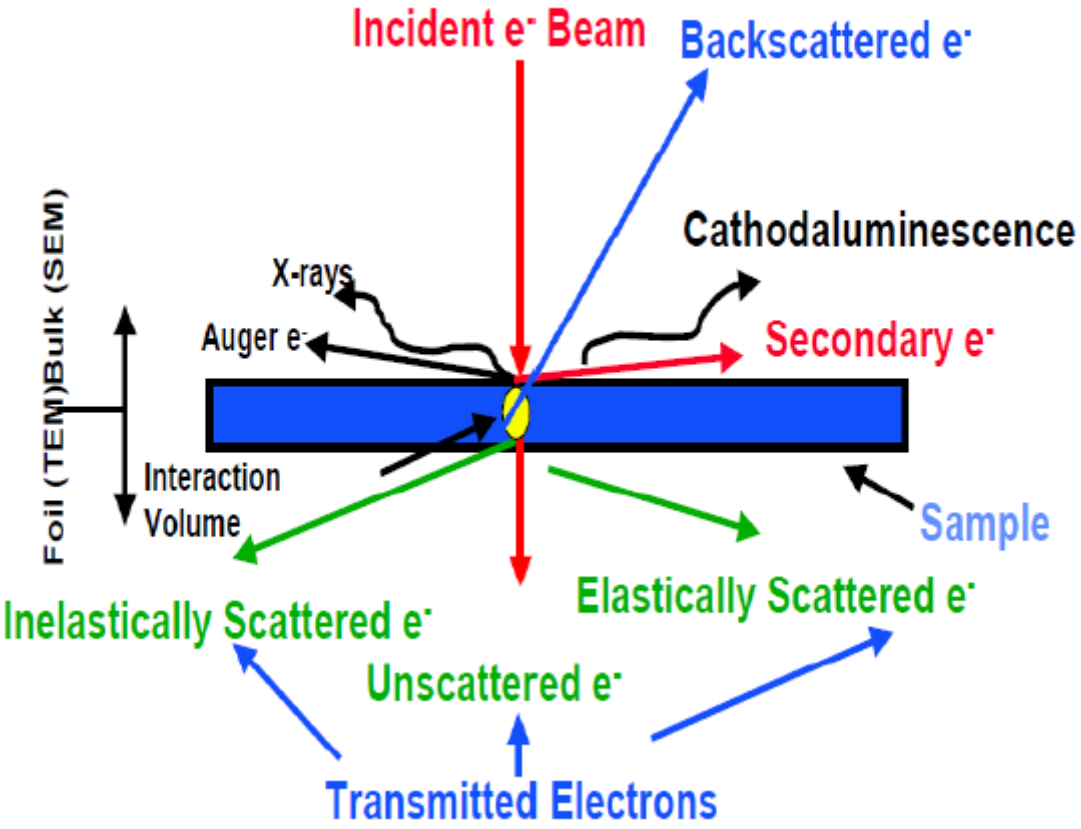

Figure 2.12 Interaction of high energy electrons with solid

The semiconducting nanoparticles were imaged using scanning electron microscopy (SEM, Zeiss EV MA-10 variable pressure SEM, Fig. 2.13) of resolution 3nm with probe current of 100 pico amp. It works in SEI mode i.e. it utilizes secondary electrons emitted from sample surface. Samples are scanned at accelerating voltage of 10.00 KV and WD of 12.00 mm at different magnifications from 1.00 KX - 30.00 KX under vacuum pressure of 10^{-6} Torr.

Figure 2.13 Zeiss EVO MA-10 variable pressure SEM at NPL

2.3.2.3 Transmission Electron Microscopy

The transmission electron microscopy is a powerful technique to study the microstructure of the sample. Using this technique grain size and shape, orientation of the grains, crystalline defects, lattice images, etc. can be investigated.

Theory

The basic principle of lattice imaging by TEM is discussed in the following subsections.

Direct Lattice Resolution

In this case two coherent beams, i.e., one undeviated and one diffracted beam reach the image plane after passing through the same point of the sample, and a periodic variation in the intensity is observed. This periodicity "d" is equal to the spacing between the planes of the atoms. Since the angle of the deviation for a diffraction beam is inversely proportional to the interplaner spacing, the smallest spacing requires the use of larger objective apertures. Even a small amount of contamination on the edge of the aperture can cause sufficient electrostatic charging and lead to a serious distortions of a beam passing close to its edge, and hence a loss of resolution. It us not worthwhile increasing the size of the objective aperture beyond a certain point, to allow higher angle diffracted beam to be used to form images, because the higher order beam results in sufficiently large aberrations to prevent the periodic structure in the image from being resolved. The use of more than one diffracted beam is an advantage when beams diffracted by more than one set of crystal planes, are included. Provided the spacing between these different planes is within the resolution limit of the microscope, this allows a two-dimensional, lattice image of a crystal to be formed. In this way all the periodicities perpendicular to the electron beam, are revealed on one image.

Indirect Lattice Resolution

The periodic structure of a crystal can be revealed by means of moiré patterns from overlapping crystals, even when the actual periodicities are below the resolution limits of the microscope. We therefore call this as the indirect lattice resolution.

If two overlapping gratings are parallel, but differ in spacing, so producing a structure with a double periodicity. Beats are formed between these two periodicities, with a spacing D given by,

$$D = \frac{d_1 d_2}{d_1 - d_2}$$

Where, d_1 and d_2 are the lattice spacing of the overlapping first and second crystals respectively.

In rotation moiré pattern the two gratings have identical spacing d but are rotated with respect to each other by a small angle. In this case the spacing D is given by,

$$D = \frac{d}{2Sin(\alpha/2)}$$

Instrumental Details

A transmission electron microscope (TEM), JEM-2100F (GEOL electron microscope)200K_v has been used to study the microstructure of the colloidal nanoparticles. The photograph of the TEM is shown in the Fig. 2.14. It has a resolution of 3.5Å (point to point) and 1.44 Å (lattice). The magnification of the instrument could be varied from 100X to 4, 50,000X while the accelerating voltage could be varied from 80, 100,120,160 and 200kV. Selected area diffraction pictures could be taken with the diffraction camera length varying from 160mm to 240mm. It is a fully automated vacuum system. The state of art electronics circuits, logical and compact design facilitates both operation and maintenance. For example, start up; shut down and photography can be executed by a simple push button operation. Magnification and camera length can be directly read out regardless of any change in the accelerating voltage and recorded together with the film number on the film. Moreover the microscope provides very stable and excellent images at low to high magnification and a variety of diffraction

patterns instantly. The available attachments can permit the specimen to be heated cooled, tilted in-situ and also enable various signals from the specimen to be observed.

The column of the microscope consists of an electron gun, two stage condenser lenses, and interlocking two stage beam reflector, specimen chamber, the image forming system which is normally composed of an objective lens, two stage intermediate lenses and a projector lens. Viewing chamber and camera chamber are also the parts of the column. The specimen chamber has a side entry stage. The specimen exchange device contains an air lock mechanism so that the specimen can be exchanged without breaking the column vacuum. The specimen holder has a capacity of holding two specimens. The specimen movement range in X and Y directions are ±1mm while along the Z direction it is ± 0.5 mm. The specimen can be tilted by an angle of ± 30^0C (X tilt).

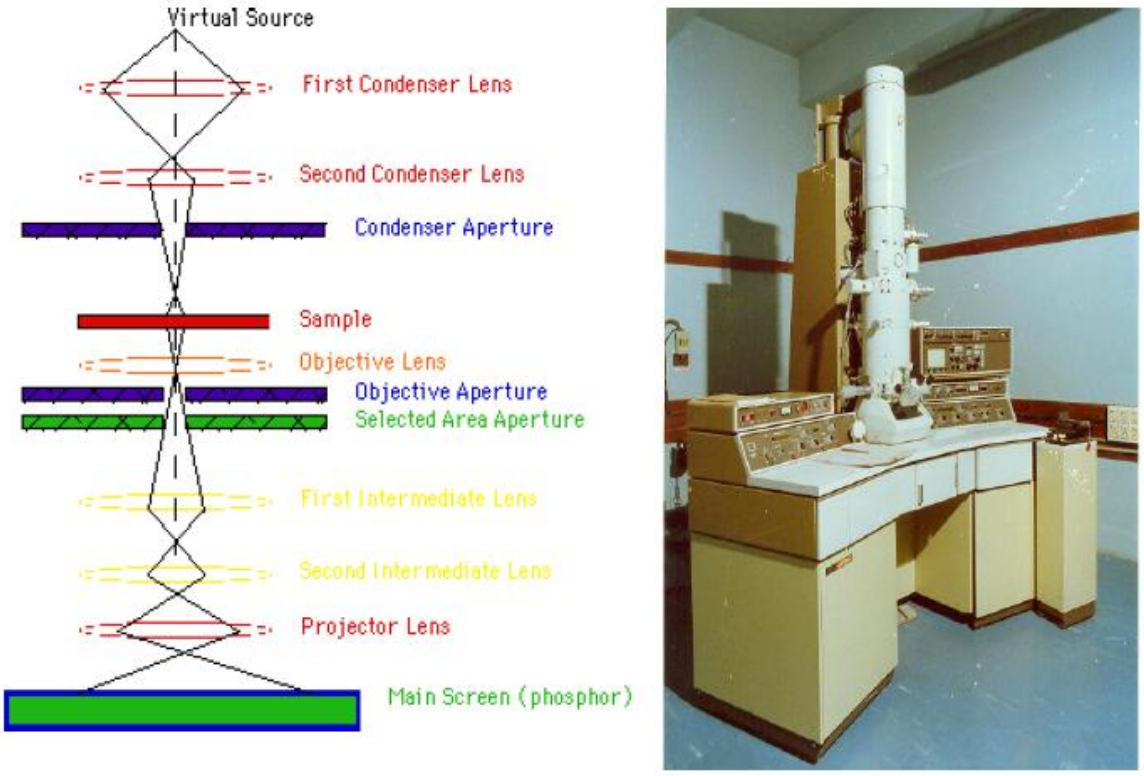

Figure 2.14 Transmission Electron Microscope

The viewing chamber consists of a viewing window to see image of the specimen formed on the fluorescent screen. A binocular with a clear field is also installed with it to see the ten times enlarged for image focusing purposes. The approximate size of an individual particle in the image of the specimen on a photographic screen can also be estimated with the help of small scale provided on the photographic screen. This instrument has a fully automatic camera complete with a data recording device and its specially designed automatic exposure mechanism ensures optimum exposure. Since this camera is equipped with an air lock mechanism, rapid film exchange can be executed without breaking the vacuum of the column. The camera chamber has films loading capacity up to 50. The cut film having a size 65mm X 90 mm, supplied by Eastman Kodak company USA were used for recording purpose.

Samples Used and Their Preparation

For viewing the morphology of the nanoparticles formed, nanoparticles were washed several times in methanol to remove the extra groups. Very dilute solutions of these washed nanoparticles in methanol were dropped on carbon coated meshed TEM grids and the solvent was allowed to evaporate leaving the nanoparticles on the grid. These grids were then loaded in the vacuum chamber of the microscope for viewing.

2.3.3 Spectral Study

2.3.3.1 Theory of FTIR spectroscopy:

FTIR (Fourier Transform Infrared) or simply FTIR Analysis, is most useful technique for identifying chemicals that are either organic or inorganic. It can be utilized to quantitate some components of an unknown mixture. It can be applied to the analysis of solids, liquids, and gasses. FTIR spectroscopy is a multiplexing technique, where all optical frequencies from the source are observed simultaneously over a period of time known as scan time. In this technique whole data is collected and converted from an interference pattern to a spectrum.

By interpreting the infrared absorption spectrum, the chemical bonds (functional groups) in a molecule or molecular structure of materials, whether organic or inorganic can be determined. FTIR spectra of pure compounds are generally so unique that they are like a molecular "fingerprint". While organic compounds have very rich, detailed spectra, inorganic compounds are usually much simpler.

The technique works on the fact that bonds and groups of bonds vibrate at characteristic frequencies.A molecule that is exposed to infrared rays absorbs infrared energy at frequencies which are characteristic to that molecule i.e. those frequencies where the infrared light affects the dipolar moment of the molecule. Thus monatomic (He, Ne, Ar, etc) and homopolar diatomic (H_2, N_2, O_2, etc) molecules do not absorb infrared light. During FTIR analysis, a spot on the specimen is subjected to a modulated IR beam. The specimen's transmittance and reflectance of the infrared rays at different frequencies is translated into an IR absorption plot consisting of reverse peaks. The resulting FTIR spectral pattern is then analyzed and matched with known signatures of identified materials in the FTIR library. IR absorption information

is generally presented in the form of a spectrum with wavelength or wave number as the x-axis and absorption intensity or percent transmittance as the y-axis. Transmittance, T, is the ratio of radiant power transmitted by the sample (I) to the radiant power incident on the sample (I_0). Absorbance (A) is the logarithm to the base 10 of the reciprocal of the transmittance (T).

$$A = \log_{10} \frac{1}{T} = -\log_{10} T = -\log_{10} \frac{I}{Io}$$

The transmittance spectra provide better contrast between intensities of strong and weak bands because transmittance ranges from 0 to 100% T whereas absorbance ranges from infinity to zero.

In our case all FTIR spectra were recorded with a single beam Perkin Elmer instrument (Spectrum BX-500) FT-IR Model spectrophotometer Fig. 2.15. This spectrometer allows us to collect spectra in mid-IR, far-IR and near-IR spectral ranges. The spectrum BX contains a CDRH Class II Helium Neon (HeNe) laser, which emits visible, continuous wave radiation at a wavelength of 633 nm and has a maximum output power of less than 1mW.

The recording abscissa range of this instrument is 400-4000cm^{-1}. Each spectrum was collected with 64 scans co-added at 4cm^{-1}resolution.

Figure 2.15 Perkin Elmer FTIR system

The normal operation mode of this spectrometer is temperature stabilized. The spectrometer utilizes continuous dynamic alignment to ensure exceptional high-resolution line shapes. Its compact optical path minimizes beam path length and improves spectral performance by limiting the number of beam reflections, which translates into extremely reproducible results with no instrument drift. Before measurement the instrument is properly sealed and desiccated. The desiccant protects the beam splitter and other optical components by reducing the amount of water vapour inside the spectrometer.

2.4 References

1. http://www.mems-exchange.org/MEMS/processes/deposition.html
2. S.R.C. Vivekchand Chemical Physics Letters 386, 313–318, **(2004).**
3 Journal of Optoelectronics and Advanced Materials Vol. 7, No. 2, p. 631 – 636, (**2005).**
4 B.D.Cullity,Elements of X-ray diffraction, Addison Wesley publishing co. lnd,London,**(1967).**
5 http://prism.mit.edu/xray.

6 J.W.Heal, J.T.Sparrow, P.M.Cross, in use of the Scanning Electron Microscopy, Pergaon Press, Oxford, **(1972).**

7 W.R.Wenk, Electron microscopy in mineralogy, Springer verlag , Berlin Heidelberg, Germany, **(1976).**

8 P.B.Hirsch, A.Howie, P.B. Nicholson,D.W.Pashley,M.J.Whelen, Electron Microscopy of thin crystals, Butler worths,London,**(1957).**

9 http://en.wikipedia.org/wiki/X-ray_photoelectron_spectroscopy.

10 http://en.wikipedia.org/wiki/Atomic_force_microscopy.

CHAPTER – 3

Synthesis of II - VI nanoparticles using single-source precursors

---

3.1 Synthesis of CdS nanoparticles using single source precursors

3.1(a) Introduction

In his 1915 publication, 'The World of Neglected Dimensions', Ostwald drew attention to the mesoscopic world, which bridges the gap between atoms and molecules on one hand and solid state science on the other hand[1].The early work on synthesis of nanoparticles was primarily based on classical colloidal chemistry[2-5].However, the first real breakthrough related to the synthesis of semiconductor nanoparticles in non-aqueons media was made by Bawendi's group[6-7]. In this method the controlled assembly of molecules is achieved by using a suitable capping agent which is functionally analogous to surfactants in the colloidal route.

Capping groups present a significant steric barrier to the addition of material to the surface of a growing crystallite and thus slowing the growth kinetics. The TOP solvent coordinates to the surface of the crystallites and permits slow and steady growth at high temperatures.Once the growth process is over, the mixture is cooled to about room temperature and methanol is added. The nanocrystallites are insoluble in methanol while the organic by-products are soluble. Therefore the precipitated crystallites can be separated by centrifugation.

It is now well known that the nature of the precursor will decide the quality of the nanocrystals produced. In the case of dithiocarbamates subtle changes in the substituents at the nitrogen atom can markedly affect the thermal decomposition of the precursor.

Our research has focused on a rational approach using single molecular-precursors to develop methods of nanoparticle synthesis. There are a number of potential advantages of using single-molecular precursors over other existing methods:

- Single source routes avoid the need for volatile, sometimes toxic and/or pyrophoric precursors.
- Some II-VI and III-V nanoparticles are air sensitive. All precursor synthesis is carried out under anaerobic conditions, with the resulting precursors being air and moisture stable.
- One involatile precursor is involved, purification of which is easier than that of two or more volatile precursors, and hence there is less chance of the incorporation of impurities into the nanoparticles.
- Low temperature deposition routes are possible.
- Although there are theoretical models predicting the optical properties of semiconductor nanoparticles, the properties of nanoparticles obtained by new synthetic routes are sometimes hard to anticipate and may lead to particles with unique and unanticipated, but useful, properties.

3.2 Synthesis of CdS nanoparticles using cadmium ethylxanthate

3.2(a) Introduction

Metal xanthates were known since 1815 when Zeise prepared xanthates of potassium, barium, lead and copper[8]. These compounds are formed by the reaction between a metal alkoxide and carbon disulphide. However, the detailed structural studies were carried out in the last three decades[9].Xanthates are expected to resemble dithiocarbamates in its bonding and coordination mode. In the solid state the 1:2 complex of cadmium with N, N-diethyldithiocarbamate is built from essentially molecular dimers of $Cd_2(S_2CNEt_2)_4$. Two of the dithiocarbamate groups act as bidentate chelating ligands, and the other two as bridging ligands.The cadmium atom is five-coordinate, the coordination polyhedron being intermediate between a tetragonal pyramid and a trigonal pyramid[10]. In contrast, in the case of cadmium ethylxanthate each cadmium atom is surrounded by four sulphur atoms arranged almost tetrahedrally around it.A major structural difference from the dithiocarbamates is that each sulphur atom is part of a different xanthate group, which in turn, bridges two adjacent cadmium atoms resulting in a two dimensional network consisting of the cadmium atoms and xanthate groups [9].

3.2(b) Synthesis of Cd $(C_2H_5OCS_2)_2$

Cadmium chloride (0.005 mol) dissolved in 20 mL distilled water was allowed to react with a solution of potassium ethylxanthate (0.01 mol) in 20 mL distilled water. The pale yellow precipitate formed was filtered, washed with distilled water and dried under vacuum.

3.2(c) Synthesis of CdS Nanocrystals

CdS nanoparticles were synthesised by the thermolysis of the precursor using standard Schlenck techniques. In the present work, CdS nanoparticles were synthesized using two routes.

Pyridine route:

60 mg of Cd-X was taken in a three neck flask, and a few drops of pyridine were mixed to convert it to a pyridium complex, 5 ml of DCB was added as solvent, and it was then heated to about 80-120^{0}C under an atmosphere of nitrogen, for 30 minutes. This synthesis is One Pot Synthesis route. The solution was then cooled to room temperature and an excess of methanol was added. The flocculent precipitate formed was centrifuged and washed with methanol followed by the measurement of the optical absorption spectrum as dispersion in toluene.

Oleylamine route (OLA):

10 ml of DCB along with 1ml TOP and 1ml Oleylamine was taken in a three neck flask.100 mg Cd-X along with 2 ml DCB, few drops of Pyridine and Oleylamine is mixed well in a culture bottle. The mixture in three neck flask was heated at different temperatures 60^{0}C,80^{0}C,120^{0}C and 150^{0}C.Solution in the culture bottle was injected immediately after attaining above temperatures. Entire synthesis is done under nitrogen atmosphere for 30 minutes. The solution was then cooled to room temperature and an excess of methanol was added. The flocculent precipitate formed was centrifuged and washed with methanol followed by the measurement of the optical absorption spectrum as dispersion in toluene.

3.2(d) Results and Discussions

In the present study Cd $(C_2H_5OCS_2)_2$ has been proven to be an efficient single-molecule precursor for the deposition of CdS nanocrystallites. This precursor is easy to synthesize, air stable and pyrolyzes cleanly to give good yields.

3.2(d)-(i) TGA and DSC studies

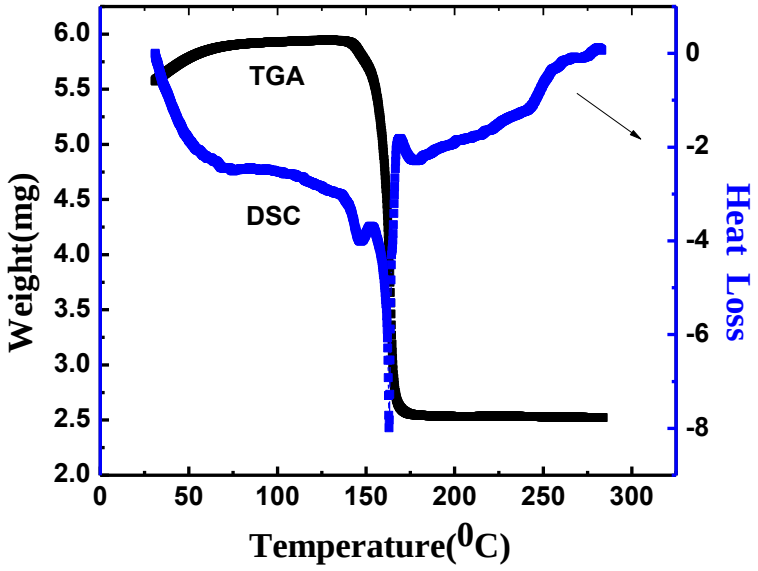

Figure 3.1 Thermo gravimetric Analysis and Differential Scanning Calorimetry of Cadmium ethylxanthate precursor.

Thermal decomposition of precursor was studied by Thermo gravimetric Analysis (TGA) and Differential Scanning Calorimetry (DSC) of samples. Thermo gravimetric analysis of cadmium ethylxanthate (CdX) was carried out from room temperature to 300^0C. The TGA curve in Fig. 3.1 shows that significant weight losses (WL) of 56% takes place in temperature region starting at 142^0C until 170^0C and is because of thermal decomposition of Xanthate complex into CdS. The end products are cadmium sulphide and volatile compounds. Since

the decomposition occurs around 142°C, the synthesis was carried out near to this temperature only.

The DSC plot in Fig. 3.1 reveals several peak and dips. The sharp dips at temperature 147^0C and 162^0C represents that the reaction is endothermic and dip at temperature 170^0C represents that the reaction is exothermic The enthalpy changes associated with the events occurring are given by the area under the sharp dips. In general, the heat capacity will also change over the region.

3.2(d)-(ii) Optical Property – Photoluminescence(PL) Study

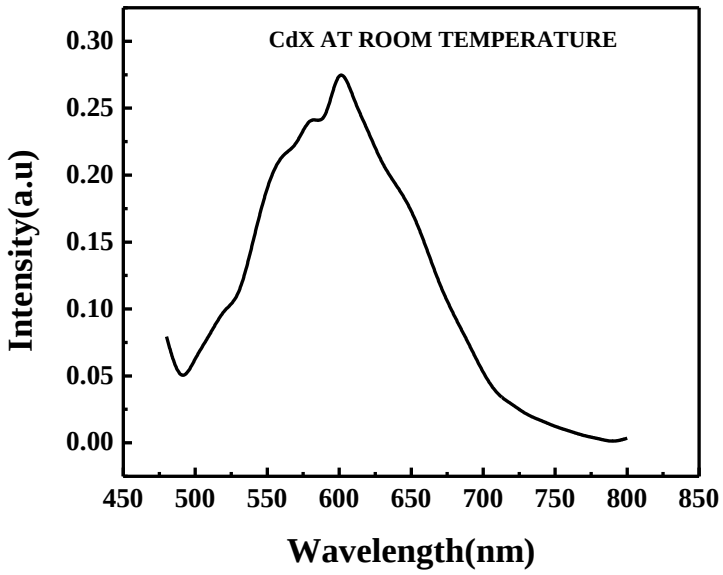

Figure 3.2 Photoluminescence spectra of CdS at room Temperature

Bulk CdS has a broad emission with a maximum in the 500-700 nm region of the luminescence spectrum as shown in Fig. 3.2. The emission is believed to be due to recombination from surface defects. We were able to synthesize CdS even at room

temperature with the oleylamine route. This is also evident from the absorption and taucs plot that we are able to synthesize CdS in nanoregime even at room temperature.

3.2(d)-(iii) Optical property- UV absorption study

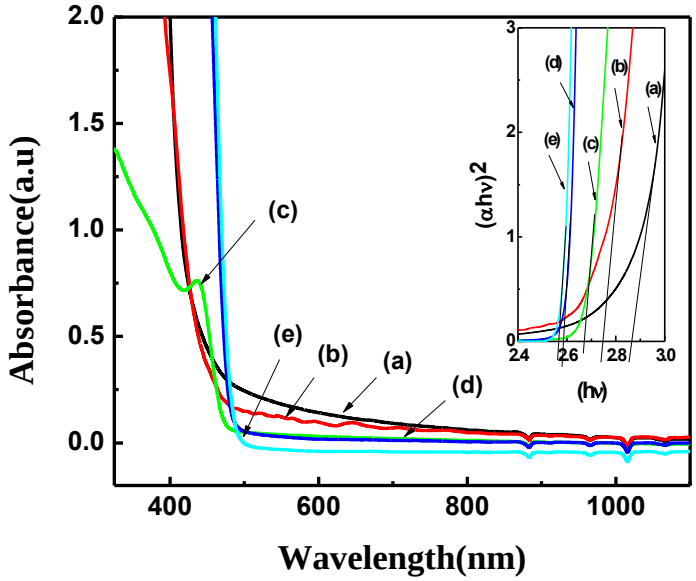

Figure 3.3 UV plot of CdS at different conditions –OLA Route (inset shows Tauc's plot)

(a)-Room Temperature (b)-60^0 (c)-80^{0}C (d)-120^{0}C (e)-150^{0}C

For the bulk crystallites we usually observe the interband absorption spectrum with a band edge around 515nm.As the crystallite size decreases there is a blue shift of the absorption edge. In the present case from Fig. 3.3 and Fig. 3.4 the band edge is observed at 465nm in OLA route and 460nm in Pyridine route. The absence of any substantial change in the band gap of the samples at different temperatures is an indication that nucleation and growth takes place very rapidly at the temperature of injection through first route i.e. OLA route. The particles grow to an optimum size within five minutes of injection. As Pyridine route is one pot synthesis route so nucleation and growth simultaneously takes place at 120^{0}C.Pyridine

plays an important role in decreasing the decomposition temperature. There is a change in the band gap in Fig. 3.3(inset) and Fig. 3.4(inset) from 2.56eV (bulk sample) to 2.86eV through

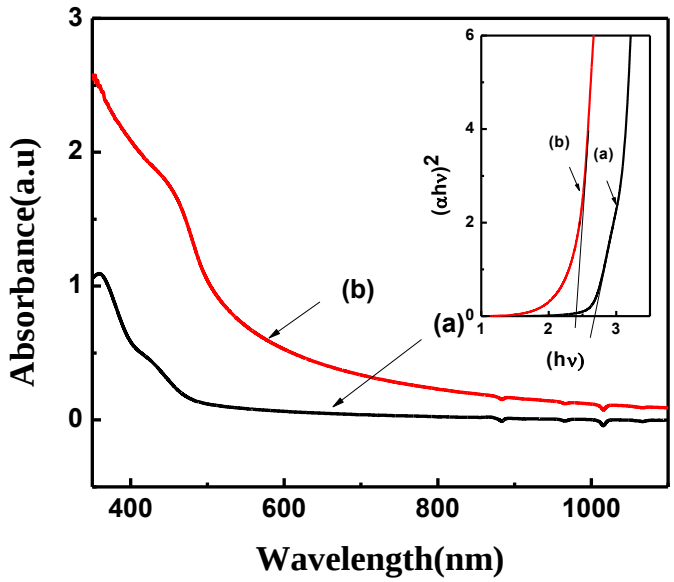

Figure 3.4 UV plot of CdS at different conditions –Pyridine Route(inset shows Tauc's plot) (a)-80^{0}C (b)-120^{0}C

OLA route and from 2.4eV (bulk sample) to 2.7eV through Pyridine route, a significant shift in the band gap. The diameters of the nanoparticles can be calculated from the absorption edges by using an effective approximation method called Brus equation[11-12] as follows:

$$\Delta E = \frac{\hbar^2 \pi^2}{2R^2}\left[\frac{1}{\text{me}} + \frac{1}{mh}\right] - \frac{1.8e^2}{\epsilon R} \qquad (1)$$

where ΔEg is the shift of band gap of the nanoparticle with respect to the bulk semiconductor, R is the particle size, ε is the dielectric constant of the bulk material, me is the effective electron mass, and mh is the effective hole mass..Particle size for Pyridine treated

samples as evident from taucs plot is found to be 5nm for sample prepared at 80^0C and 7nm for sample prepared at 120^0C.

3.2(d)-(iv) Structural Characteristic-XRD Study

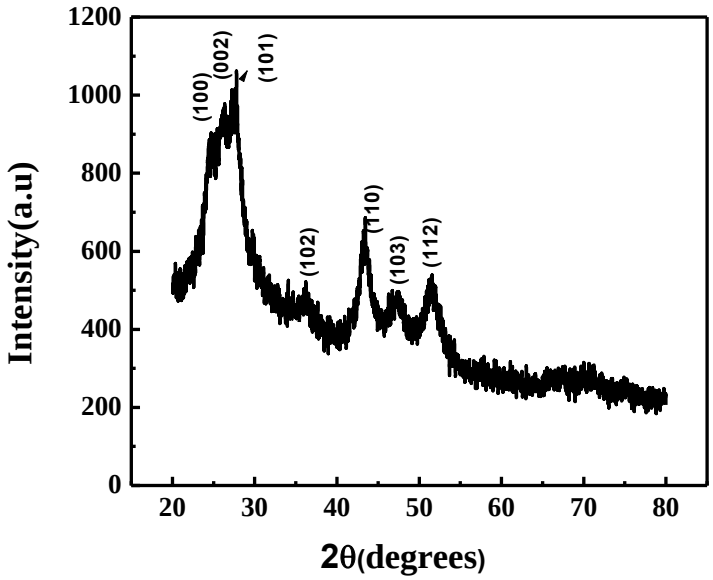

Figure 3.5 X-ray diffraction pattern of CdS nanoparticles synthesized using Cd $(C_2H_5OCS_2)_2$ at 120^0C stabilized for 30 minutes.

Bulk CdS usually exists in the hexagonal phase from room temperature to the melting point. However, CdS nanocrystallites can exist as either cubic or the hexagonal phase. The wide-angle powder X-ray diffraction pattern of the nanocrystallites is shown in Fig. 3.5 and Fig. 3.6 above.The XRD peaks are broadened compared to those of the bulk CdS which is an indication that the particles are in the nanosize regime. However, the(110), (103), and (1l2) planes of wurtzite CdS are clearly distinguishable in the diffraction pattern,other hexagonal peaks are observed at (100),(002),(101)and (102) which are consistent from JCPDS card(no.65-3414).

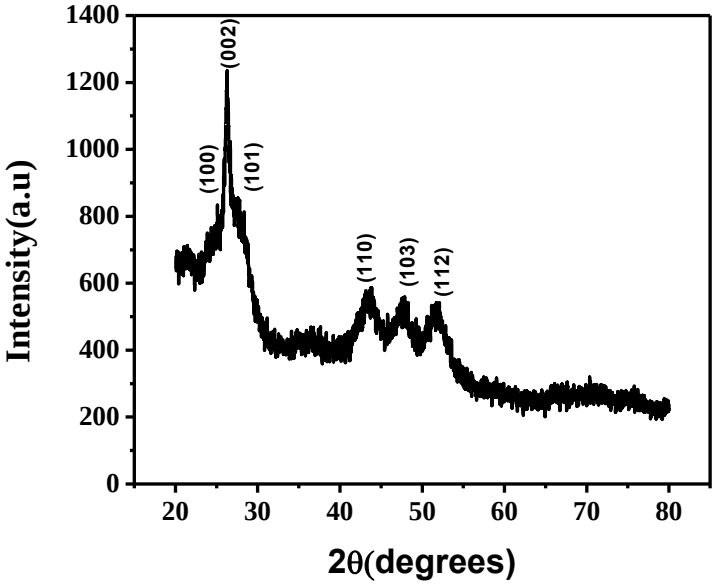

Figure 3.6 X-ray diffraction pattern of CdS nanoparticles synthesized using Cd $(C_2H_5OCS_2)_2$ at 80^0C stabilized for 30 minutes.

The mean crystallite diameter,d, can be calculated by the Scherrer formula[13],

$$d=0.9\lambda/\beta\text{Cos}\theta$$

where λ is the X-ray wavelength,and β is the full width at half maximum of the diffraction peak on the 2θ scale.The size of the crystallites was determined using the (110) reflection at 43.25^0 (2θ) and the calculated value is found to be 7nm for Fig. 3.5 and 5nm for Fig. 3.6.

3.2(e) Conclusion

In the present work the synthesis of CdS nanocrystallites with a relatively narrow size distribution could be achieved by the thermolysis of cadmium ethylxanthate. The average particle size of the crystallites was estimated by two different methods viz.optical absorption and XRD. X-ray diffraction studies reveal that the CdS nanocrystallites exist as the hexagonal

phase.Optical absorption measurements show that the band edge is blue shifted indicating the quantum confinement of the particles. The optical absorption measurements of samples formed at different temperatures after the injection of the precursor in OLA route and single pot synthesis i.e. pyridine route was used to monitor the growth of the particle with temperature.

3.3 Synthesis of ZnS nanoparticles using single source precursors

3.3(a) Introduction

Bulk ZnS is an important semiconducting material which is commercially used as a phosphor and also in thin film electroluminescent devices[14-16]. ZnS doped with various transition metal ions such as manganese is an efficient light emitting material. When such dopants are inserted into nanometre sized ZnS matrix, they exhibit interesting magneto-optical properties[17,18].

In order to obtain well-defined and optimised properties, it is necessary that the synthesised particles have a narrow size distribution; a higher crystallinity and a lower defect density. The bulk of the studies on ZnS quantum crystallites in the past have been those in the form of colloids, with the main interest being the study of their photocatalytic and photochemistry aspects[19,20].The photocatalytic activity of the colloids is enhanced by varying the size of the crystallites owing to the shift of the valence and conductance bands. Therefore the redox potential of the crystallites changes as a function of their size. This has been demonstrated by Kanemoto et al.[21] in the case of photo reduction of CO_2 by ZnS nanocrystallite in organic solvents.Rosetti et al.[22] and Henglein and co-workers[23] have studied the evolution of the optical and electronic properties of ZnS nanocrystallites with varying sizes. These colloids

however, are stable only for a short duration of time, as they are prone to photo-corrosion and also agglomerate into larger particles[24-26]. There have also been attempts to obtain free standing powders of ZnS nanocrystallites by using suitable surface passivating agents such as thiols or surfactants that covalently bind to the surface atoms of the nanocrystallites, making them stable under normal atmospheric conditions[27]. However, most of these synthetic procedures, whether used to form colloids or capped free-standing powders, yield crystallites having a large size distribution. This is most commonly evident from the UV-vis optical absorption spectra which, in many reported cases, are broad and featureless. There are also reports of the synthesis of nano-sized ZnS in structured media such as polymer[28.29] and gel films[30,31]. Good quality ZnS nanocrystallites are prepared by the thermolysis of elemental zinc and sulphur in a coordinating solvent[32].

3.3(b) Preparation of Zinc ethylxanthate

Zinc chloride (0.1 mol) dissolved in 50 mL distilled water was allowed to react with a solution of potassium ethylxanthate (0.05 mol) in 200 mL distilled water. The white precipitate formed was filtered, washed with distilled water and dried under vacuum.

3.3(c) Synthesis of ZnS Nanocrystals

ZnS nanoparticles were synthesised by the thermolysis of the precursor using standard Schlenck techniques. 60 mg of Zn-X was taken in a three neck flask, and a few drops of pyridine were mixed to convert it to a pyridium complex, 5 ml of DCB was added as solvent, and it was then heated to about 80-120^{0}C under an atmosphere of nitrogen, for 30 minutes. This synthesis is One Pot Synthesis route. The solution was then cooled to room temperature and an excess of methanol was added. The flocculent precipitate formed was centrifuged and

washed with methanol followed by the measurement of the optical absorption spectrum as dispersion in toluene.

3.3(d) Results and Discussions

3.3(d)-(i) TGA-DTA studies

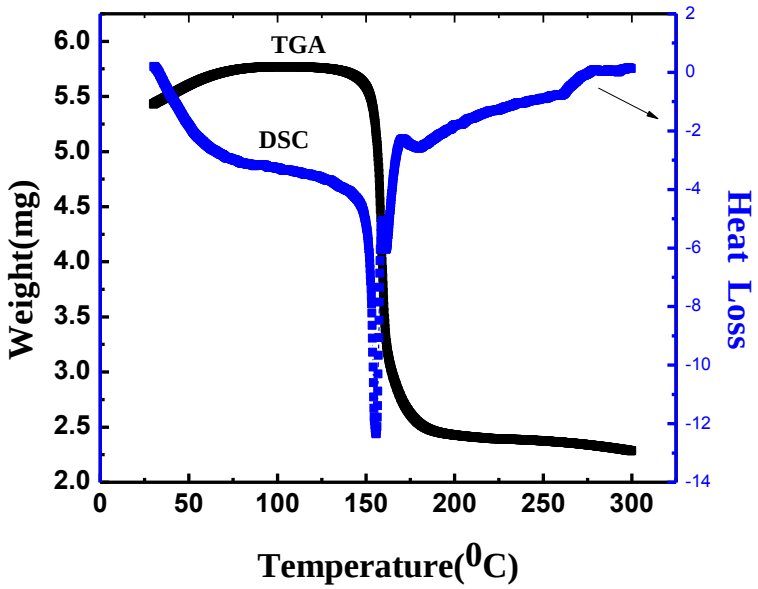

Figure 3.7 Thermo Gravimetric Analysis and Differential Scanning Calorimetry of Zinc ethylxanthate precursor.

Thermal decomposition of precursor was studied by Thermo gravimetric Analysis (TGA) and Differential Scanning Calorimetry (DSC) of samples. Thermo gravimetric analysis of Zinc ethylxanthate (ZnX) was carried out from room temperature to 300^{0}C. The TGA curve in Fig. 3.7 shows that significant weight losses (WL) of 56% takes place in temperature region starting at 148^{0}C until 174^{0}C and is because of thermal decomposition of Xanthate complex into ZnS. The end products are Zinc sulphide and volatile compounds. Since the decomposition occurs around 148°C, the synthesis was carried out near to this temperature only.

The DSC plot in Fig. 3.7 reveals several peak and dips. The sharp dips at temperature 156^0C represents that the reaction is endothermic and dip at temperature 170^0C and 272^0C represents that the reaction is exothermic The enthalpy changes associated with the events occurring are given by the area under the sharp dips. In general, the heat capacity will also change over the region.

3.3(d)-(ii) Spectral study-FTIR study

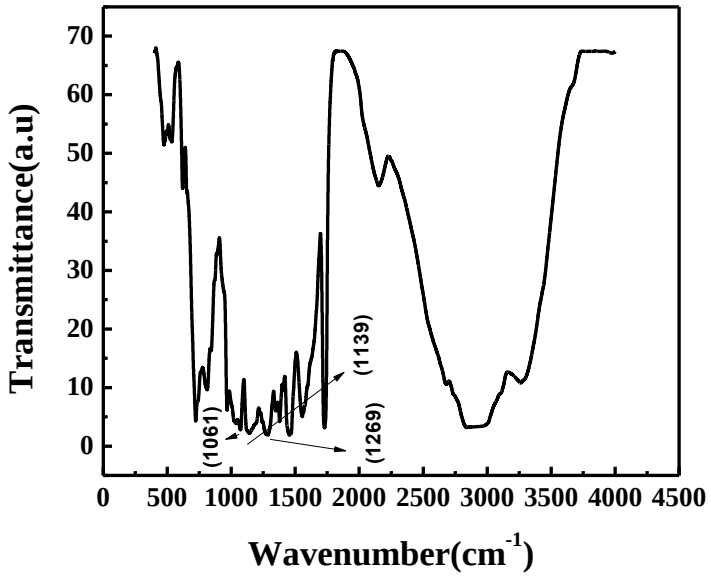

Figure 3.8 FTIR spectra for ZnS

The coordination action of the ligand molecules on monomer and resultant ZnS nanocrystals were investigated by FTIR technique(Fig. 3.8).It has been well proven that the ligands containing N-donor or P- donor can coordinate with the central metal atom in metal Xanthates to form corresponding adducts.The IR spectra shows C-O asymmetric vibration(at 1269cm^{-1}) and C-O symmetric vibration (at 1139cm^{-1})both shift to lower frequency, while its

C-S stretching vibration (at 1061cm^{-1}) shift to higher frequency. The bands at 1300-1400cm^{-1} can be assigned to the stretching vibrations and bending vibrations of C-H.

3.3(d)-(iii) Structural Property-EDS analysis

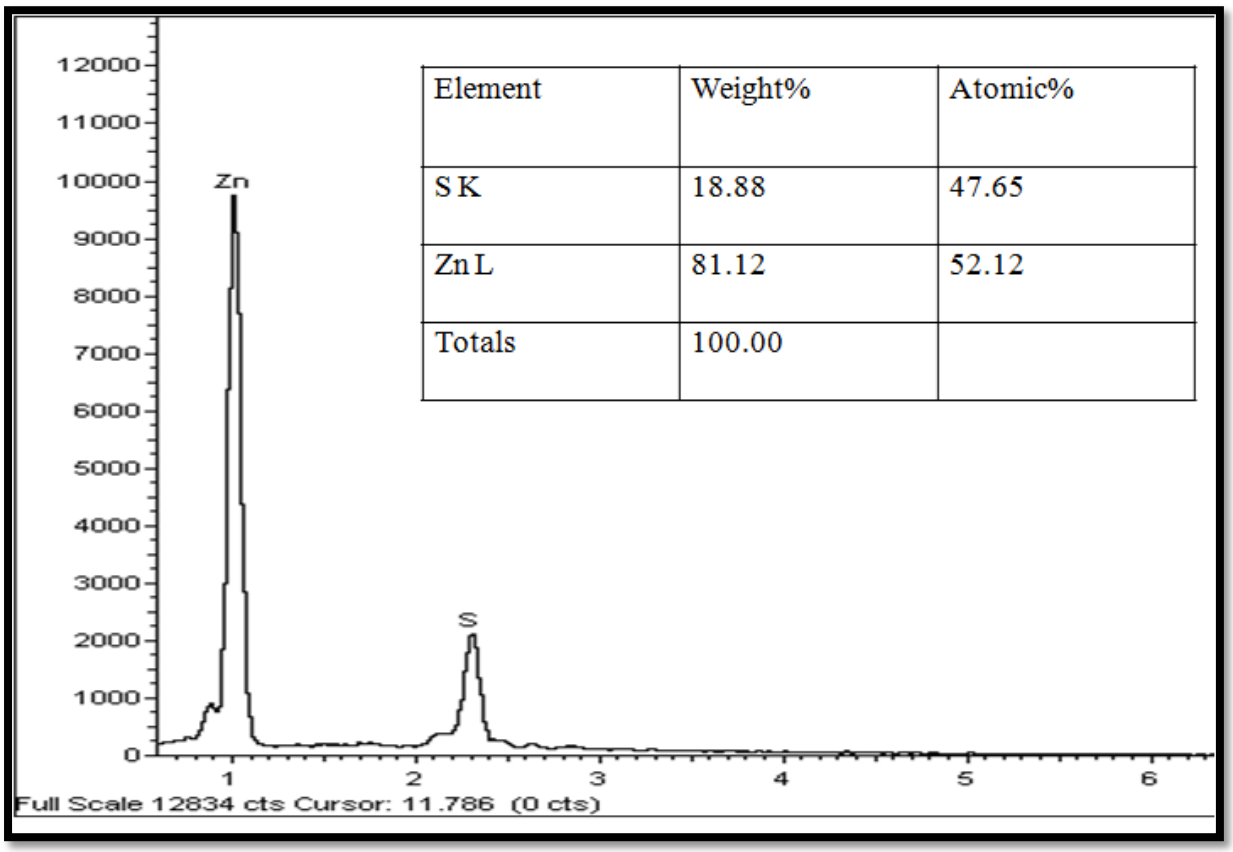

Element	Weight%	Atomic%
S K	18.88	47.65
Zn L	81.12	52.12
Totals	100.00	

Fig 3.9 EDS pattern for ZnS

To further investigate the composition of the ZnS, the energy dispersive X-ray spectroscope (EDS) spectrum (Fig 3.9) was obtained. EDS analysis of the ZnS demonstrates that the chemical component consists of Zn and S and Table shows approximate relative ratio of Zn: S~1:1. This ratio agrees with the nominal ZnS statiometry.

3.3(d)-(iv) Optical Property – UV Absorption study

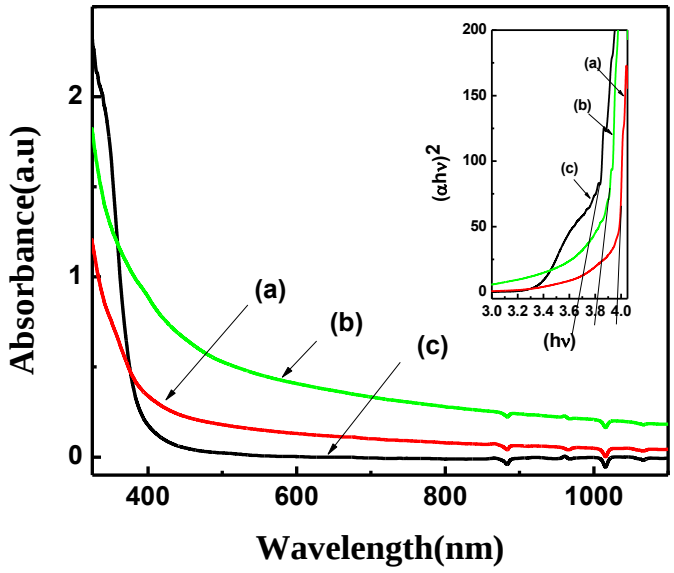

Figure 3.10 UV Plot of ZnS at different conditions OF ZnS(inset Tauc's plot) (a)-80^{0}C (b)-100^{0}C (c)- 120^{0}C

The absorption spectra of ZnS samples of different sizes prepared by the colloidal route has been analyzed in Fig. 3.10.The absorption edges (or peaks) of the samples all display an obvious blue shift compared to the bulk ZnS (335nm) because of the quantum confinement. Obviously, the intensity of quantum confinement in the nanocrystals is determined by their diameters no matter whether they are nanorods or nanodots. They have also shown that the excitonic peak maximum shifts towards higher energy (Fig. 3.10(inset)) with a decrease in the nanocrystallite size due to quantum size effect that enhances the band gap with decreasing particle size. Though the binding energy of the exciton also increases with decreasing size due to an increasing Coulombic overlap enforced by enhanced spatial localisation of the wave functions, the shift in the band gap with size dominates the spectral changes. There is a change in the band gap in Fig. 3.10(inset) from 3.67eV (bulk sample) to 3.9eV, a significant

shift in the band gap The diameters of the nanoparticles canbe calculated from the absorption edges by using an effective approximation method called Brus equation[11,12] as follows:

$$\Delta E = \frac{\hbar^2 \pi^2}{2R^2}\left[\frac{1}{\text{me}} + \frac{1}{mh}\right] - \frac{1.8e^2}{\in R} \qquad (1)$$

where ΔEg is the shift of band gap of the nanoparticle with respect to the bulk semiconductor, R is the particle size, ε is the dielectric constant of the bulk material, me is the effective electron mass, and mh is the effective hole mass.Particle size for Pyridine treated samples as evident from taucs plot is found to be 8nm for sample prepared at 120^0C.

3.3(d)-(v) Optical Property – Photoluminescence(PL) study

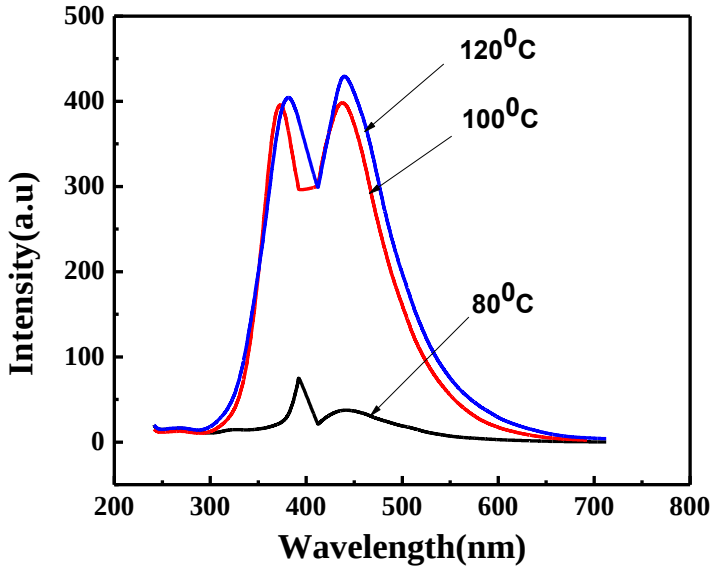

Fig 3.11 PL spectra of ZnS nanocrystals

Luminescence is one of the most important methods to reveal the energy structure and surface states of nanoparticles. The fluorescence of nanoparticles have been studied extensively[33-39]. It is reported that the fluorescence process in semiconductor nanoparticle is very complex and most nanoparticles exhibit broad, Stokes-shifted luminescence arising from the deep traps of surface states. Only those clusters with good surface passivation may

show high band-edge emission. The absence of band- edge emission was attributed to a large non-radiative decay of free electrons to the deep-trapped states[40,41]. As the particles become smaller, the surface/volume ratio and the surface states increase rapidly, thus reducing the excitonic emission via non-radiative surface recombination.

Photoluminescence spectra of the ZnS nanoparticles prepared in the present study are shown in Fig. 3.11.The photoluminescence of ZnS nanocrystals is intricate, because it is sensitive to synthetic conditions and crystal sizes and shapes, Usually, two emission peaks can be observed from semiconductor nanoparticles-excitonic and trapped luminescence. The excitonic emission is sharp and locates near the absorption edge of the particle while the trapped emission is broad and stoke-shifted. In above PL spectra, two broad emissions takes place-one around 380 nm and the other around 438nm, which can be attributed to sulphur vacancies emission and trapped surface states emission respectively.)

3.3(d)-(vi) Structural Characteristic-XRD Study

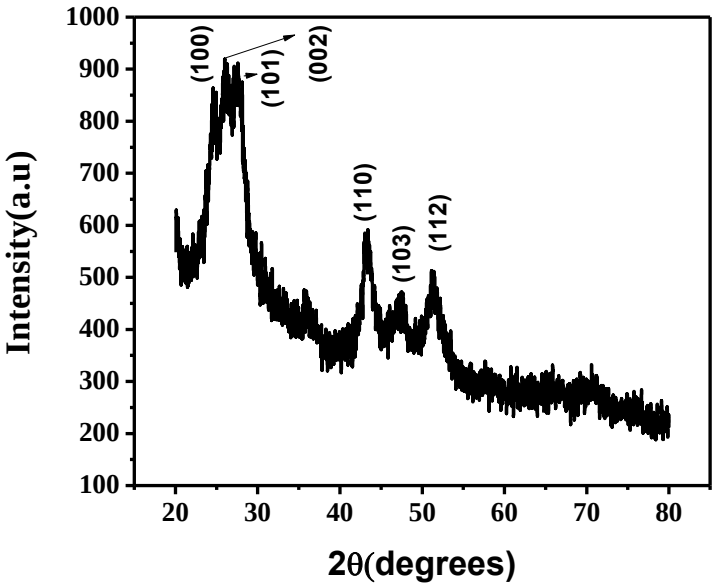

Figure 3.12 X-ray diffraction pattern of ZnS nanoparticles synthesized at 120^0C stabilized for 30 minutes.

The XRD pattern of the ZnS nanoparticles synthesised show broadened diffraction peaks compared to those of the bulk ZnS crystals, signifying the finite size of these crystallites. The (110), (103) and (112) of wurtzite Zns are clearly visible in Fig. 3.12 which are consistent from JCPDS card(no.89-7386)The mean crystallite diameter, can be calculated by the Scherrer formula[27],

$$d=0.9\lambda/\beta\text{Cos}\theta$$

where λ is the X-ray wavelength, and β is the full width at half maximum of the diffraction peak on the 2θ scale. The size of the crystallites was determined using the (110) reflection at 43.25^0 (2θ) and the calculated value is found to be 8nm.Other hexagonal phase peaks exists at (100), (101) and (002).

3.3(e) Conclusions

ZnS nanoparticles have been prepared by thermolysing the precursor compounds. The particles synthesized show blue shifts in the absorption spectra in relation to bulk ZnS. Significant shift in the band gap from3.67eV (bulk) to 3.9eV has been also observed. The photoluminescence spectra show broad emission peaks due to emission from surface traps. The XRD pattern of particles synthesized show broad peaks indexed to wurtzite ZnS.EDS pattern finally confirms the composition of ZnS.

3.4 References

1. Ostwa1d, Die Welt der vemachlassigten Dimensionen, Steinkopf, Dresden, 1915.
2. C. R Berry, Phys. Rev., 1967,161,848.
3. R Rossetti, J. L. Ellison, J. M. Gibson and L. E. Bros, J. Chem. Phys., 1984,80,4464.
4. R Rossetti, R Hull, J. M. Gibson and L. E. Bros, J. Chem. Phys., 1985, 82,552
5. A.Henglein, PureAppl. Chem., 1984, 56, 1215.
6. C.B. Murray, D. J. Noms and M.G. Bawendi, J. Am. Chem. Soc.,1993, 115,8706
7. C.B. Murray, C. R Kagan and M. G. Bawendi, Ann. Rev. Mater., Sci., 2000, 30,545.
8. W. C. Zeise, Recuil de Memoires del' Acad. Roy des Science de Copenhagen,1815,1,1.
9. RA. Zingaro and J. C. White,J. Inorg.Nucl. Chem., 1960, 12,315.
10. A. Domenicano,1. Torelli, A. Vaciago and1. Zambonelli, J. Chem. Soc., (A), 1969, 1351.
11. L.E. Brus,J. Chem. Phys., 1983,97,5566.
12. L.E. Brus, J. Chem. Phys., 1984,80,4403.
13. B. Cullity, Elements of X-ray Diffraction, 2nded. Addison-Wesley, Redding, 1978.
14. G.F.J. Garlick, A.F. Gibson, J. Opt .Soc. Am., 1949,39,935.

15. M. Ohring, The Materials Science ofThin Films, Academic, San Diego, 1992.

16. LP. McClean, C.B. Thomas, Semicond. Sci. Technol., 1992,7,1394.

17. R.N. Bhargava, D. Gallagher, X. Hong, and A. Nurmikko, Phys. Rev. Lett.,1994,72,416.

18. T.A Kennedy, E.R Glaser, P.B. Kellen, and RN. Bhargava, Phys. Rev. B,1995,52, 14356.

19. S.Yanagida,Y.Masahisa,T. Shiragami,andC.Pac,J. Phys. Chem., 1990,94,3104.

20. D.E. Dnnsyan, A. Hagfeldt, M. Alrnegren, H.O.G. Siegbahn, and E. Mukhtar,J. Phys. Chem., 1990,94, 6797.

21. M. Kanemoto, T. Shiragami, C. Pac, and S.Y anagida, J. Phys. Chem., 1992,96,3521.

22. R Rosetti,R Hull, lM. Gibson, andL.E. Bms,J. Chem. Phys., 1895,82,552.

23. A. Henglein, and M. Gutierrez, Ber. Bunsen-Ges. Phys. Chem., 1983, 87, 852.

24. R Rosetti,JL. Ellison,JM. Gibson, andLE. Brus,J. Chem. Phys.1984, 80,4464.

25. C.B. Murray, C.R Kagan, and M.G. Bawendi, Science, 1995,270, 1335.

26. AA Khosravi, M. Kundu, B.A. Kuruvilla, G.S. Shekhawat, RP. Gupta,P.D. Vyas, and S.K. Kulakarni, Appl. Phys. Lett., 1995,67(17),2506.

27. A. Y. Nakaoka, and Y. Nosaka, Langmuir, 1997, 13,708.

28. W. Mahler, Inorg. Chem., 1988, 112, 6858.

29. J.Yue,V.Sankar.m,RE.Koheo,andR.R.Scbrock,J.Am. Chem.Soc.,1993,115,4409.

30. J. Yu, H. Liu, Y. Wang, F.E. Femandez, W. Jia, L. Sun, C. Jin, D. Li, and S. Huang, Optics Letters, 1997,22(12), 1913.

31. Y. Yang, J. Huang, S. Liu, and J. Shen,J. Mater. Chem., 1997, (10), 131

32. Y. Li, Y. Ding, Y. Qian,Y. Zhang, andL. Yang,Inorg. Chem., 1998,37,2844.

33. M.G. Bawendi, D.J. Carro1, W.L. Wilson, and L.E. Bros, J. Chem. Phys.,1992,96, 946.

34. M. O'Nei1, J. Marohn, and G. Mclendon, J. Phys. Chem., 1990,94,4359.

35. L. Sphanel, M. Hase, H. Weller, and A. Hengelein, J. Am. Chem. Soc., 1987,109,5649.

36. A. Eychmuller, A. Hasselbarth, L. Katsikas, and H. Weller, J. Phys. Chem.,1991,95,79.

37. M. Tomita, and M. Matsuoka, J. Opt. Soc. Am. B 7., 1990, 1198.

38. Y. Wang, andN. Herron, J. Phys. Chem., 1988,92,4988.

39. K. Misawa, H.Yao, T. Hayashi, and T. Kobayashi,J. Lumin., 1991,48/49,269.

40. P. Roussignol, D. Ricard, K.C. Rustagi, and C. Flytzanis, J. Opt. Soc. Am. B.4, 1987,5.

41. N. Chestnoy, T.D. Harris, R. Hull, and L.E. Bros,J. Phys. Chem., 1986,90,3393.

CHAPTER – 4

Band gap engineering in nanostructured CdS thin films from visible range to near infrared by in situ Pb-doping

---

4.1 Introduction

The synthesis and characterization of semiconductor nanoparticles have attracted much interest because of their novel properties as a consequence of the large number of surface atoms and the three-dimensional confinement of the electrons. Altering the size of the particles alters the degree of the confinement of the electrons and affects the electronic structure of the solid, especially the band gap edges, which are tunable with particle size. Among a variety of semiconductor materials, the binary metal chalcogenides of group II have been extensively studied. They have outstanding potential applications, owing to their nonlinear optical and luminescence properties, quantum size effect, and other important physical and chemical properties. Nanocrystalline thin films of CdS are attractive materials in photoconducting cells and optoelectronic devices such as solar cells and photo detectors. The function of cadmium sulphide (CdS) is to allow energetic shorter wavelength photons to pass for the incidence at the hetero-interface with minimum absorption loss. The high optical bandgap of CdS (~2.4 eV) assists in this function. The other use of CdS is to provide a junction field for separation of photogenerated minority carriers before recombination.

Lead sulfide (PbS) is a prominent direct narrow gap semiconductor with a room temperature band gap of 0.41eV and finds a wide range of potential applications in various devices such

as infrared photodetectors, optical switches, sensors, and solar cells[1-3]. Because of relatively large Bohr exciton radius of 18nm [3], its band gap can be engineered over a wide range by reducing the particle size. These properties make the quantum confinement effects more notable in PbS compared to other lead chalcogenides, even for relatively larger particle sizes. In this viewpoint, PbS has been grown in various forms by different techniques such as chemical bath deposition (CBD), vacuum evaporation, spray pyrolysis, electrodeposition, colloidal route etc[3-6]. Among these techniques, Colloidal route offers simple, cost effective, and industrially scalable route for the production of high-quality films, without the need for high-deposition temperatures.

Recently, growth of mixed nanostructures based on PbS and CdS i.e ($Cd_{1-x}Pb_xS$) finds immense interest, because it offers the advantage of tuning the optical and the opto-electronic properties of CdS, viz. band gap, electrical conductivity, thermo electric power, etc., in a controlled manner [7-9]. In the present work, attempt has been made to prepare PbS and Pb-doped CdS nanoparticles by Colloidal Route. Addition of Pb is found to strongly affect the nanoparticles optical properties. We observed quantum size effect in both pure PbS and Pb-doped CdS nanoparticles and the results are discussed in detail.

4.2 Experimental

4.2(a) Preparation of Lead ethylxanthate

Lead acetate (0.001 mol) was allowed to react with potassium ethyIxanthate (0.001mol) in distilled water at room temperature. The solid formed is immediately filtered, washed with distilled water and finally dried.

4.2(b) Synthesis of PbS Nanocrystals

PbS nanoparticles were synthesised by the thermolysis of the precursor using standard Schlenck techniques. 100 mg of Pb-X was taken in a three neck flask, and a few drops of pyridine were mixed to convert it to a pyridium complex, 10 ml of DCB was added as solvent, and it was then heated to about 80-120^{0}C under an atmosphere of nitrogen, for 30 minutes. The solution was then cooled to room temperature and an excess of methanol was added. The flocculent precipitate formed was centrifuged and washed with methanol. The growth of the PbS nanoparticles was monitored as a function of time by withdrawing aliquots from the reaction mixture at different time intervals, isolating the particles followed by the measurement of the optical absorption spectrum and as dispersion in toluene.

4.2(c) Preparation of Cadmiun Lead ethylxanthate

Different concentration of Cadmium Chloride and Lead acetate was allowed to react with potassium ethyIxanthate in distilled water at room temperature to form four different precipitate mixtures as $Cd_{0.95}Pb_{0.05}X$, $Cd_{0.9}Pb_{0.1}X$, $Cd_{0.8}Pb_{0.2}X$, $Cd_{0.7}Pb_{0.3}X$ i.e. 5%,10%,20%,30% lead doping in CdS nanomaterial. The precipitate formed is immediately filtered, washed with distilled water and finally dried.

4.2(d) Synthesis of CdPbS Nanocrystals

CdPbS nanoparticles of different concentrations were synthesised by the thermolysis of the precursor using standard Schlenck techniques. 100 mg each of 5%, 10%, 20%, 30% CdPb-X was taken in a three neck flask, and a few drops of pyridine were mixed to convert it to a

pyridium complex, 10 ml of DCB was added as solvent, and it was then heated to 120^0C under an atmosphere of nitrogen, for 30 minutes. The solution was then cooled to room temperature and an excess of methanol was added. The flocculent precipitate formed was centrifuged and washed with methanol followed by the measurement of the optical absorption spectrum and as dispersion in toluene.

4.3 Results and Discussions

4.3(a) TGA-DTA Studies

Thermal decomposition of precursor was studied by Thermo gravimetric Analysis (TGA) and Differential Scanning Calorimetry (DSC) of samples.

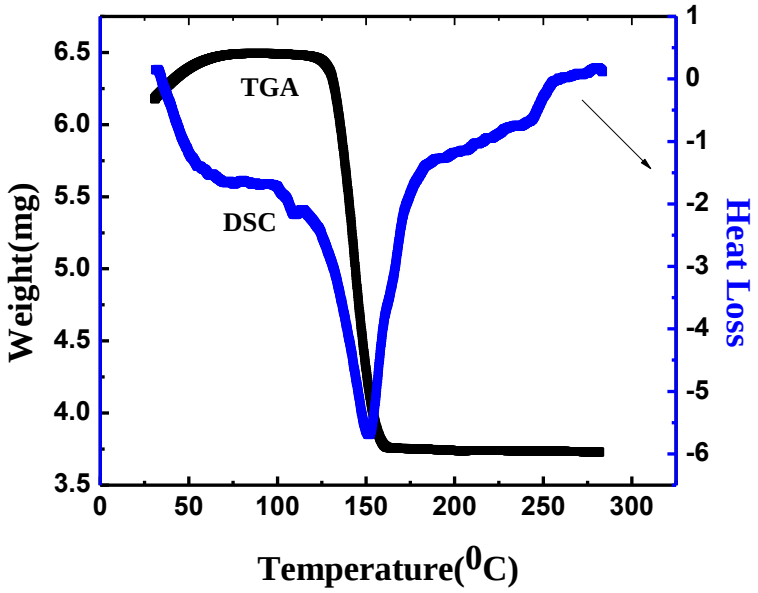

Figure 4.1 Thermogravimetric Analysis and Differential Scanning Calorimetry of Lead ethylxanthate Precursor

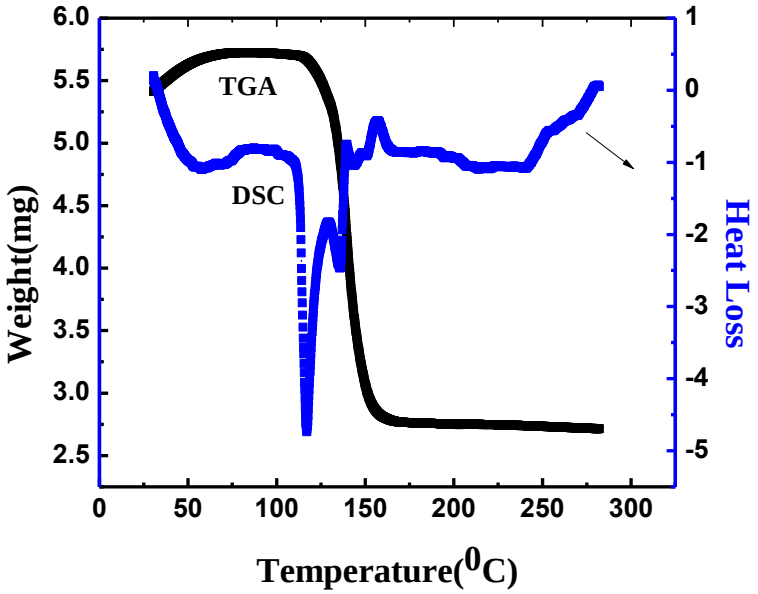

Figure 4.2 Thermo gravimetric Analysis and Differential Scanning Calorimetry of Cadmium Lead ethylxanthate precursor.

Thermo gravimetric analysis of Lead ethylxanthate (PbX) and Cadmium Lead ethylxanthate (CdPbS) was carried out from room temperature to 300^0C.

The TGA curves in Fig. 4.1 and Fig. 4.2 shows that significant weight losses (WL) of 23% and 35% takes place in temperature region starting at 128^0C until 158^0C and 118^0C until 160^0C respectively and is because of thermal decomposition of Xanthate complex into PbS and CdPbS. The end products are lead sulphide and cadmium lead sulphide and volatile compounds. Since the decomposition occurs around 128°C and 118^0C, the synthesis was carried out near to this temperature only.

The DSC plot in Fig. 4.1 and Fig. 4.2 reveals several peak and dips. The sharp dips at temperatures 108^0C, 150^0C and 244^0C in Fig5.1 and dips at temperatures 117^0C,137^0C and

243^0C in Fig. 4.2 represents that the reaction is endothermic and peaks at temperature 141^0C and 157^0C in Fig. 4.2 represents that the reaction is exothermic The enthalpy changes associated with the events occurring are given by the area under the sharp dips. In general, the heat capacity will also change over the region.

4.3(b) Optical property – UV Absorption study

Fig.4.3 exemplifies the absorption spectra of PbS and CbPdS nanocrystalsS deposited at a temperature of 120^0C. It can be seen from the spectra that Pb-doping results in a strong blue shift in the absorption onset. The band gap energy, Eg, was calculated using the Tauc's relation, $(\alpha h\upsilon)^{1/n} = A(h\upsilon - E_g)$, where A is a constant and n is equal to 1/2 for direct allowed transitions.

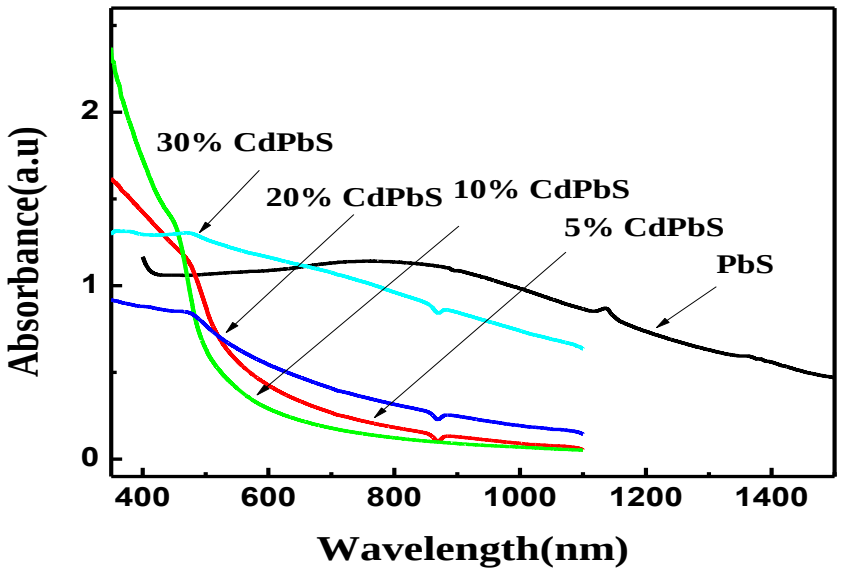

Figure 4.3 Absorption spectra of PbS and Different concentrations of CdPbS deposited at 120^0C.

The estimation of band gap from the plot of $(\alpha h\upsilon)^2$ verses $(h\upsilon)$ is shown in Fig. 4.4. Band gap values are obtained by extrapolating the linear part of the absorption curves to intercept the energy axis ($\alpha h\upsilon=0$). The estimated Eg of PbS and CdS nanocrystals is found to be 0.7eV and 2.8eV respectively for nanocrystals grown at 120^0C. Moreover, the decrease in Eg with increase in PbS concentration in CdS can be attributed to grain size effect.

The band gap of CdPbS films was also estimated. In this case, the estimated Eg values are found to be 2.4, 2.28, and 2.02, 1.42 eV, respectively, for nanocrystals deposited at 120^0C for different concentrations i.e 5%,10%,20%,30% of PbS doped in CdS respectively. This clearly indicates a considerable decrease in the band gap as a result of Pb-doping. Doping of PbS with Cd is expected to alter the optical band gap between 2.8eV (Eg of CdS) and 0.7eV (Eg of PbS) in the resulting ternary CdPbS alloy. Thus, the observed large modification in the

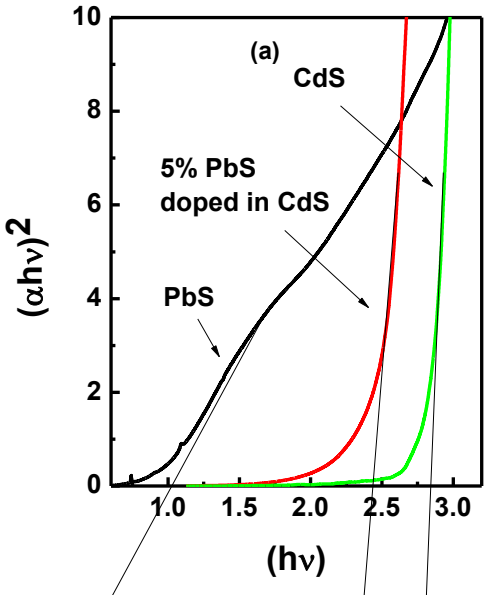

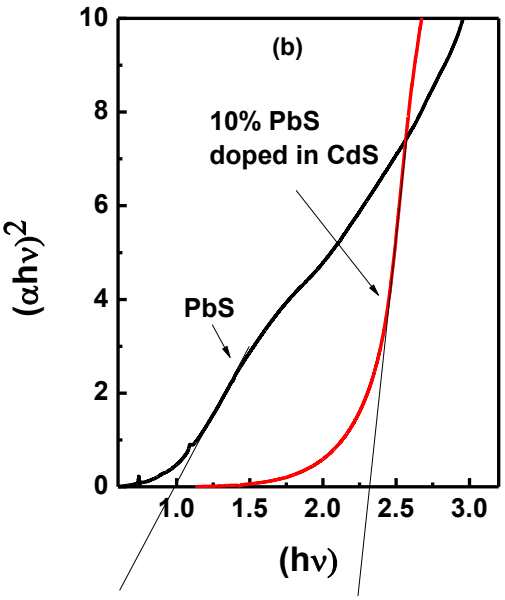
(b)
10% PbS
doped in CdS
PbS
$(\alpha h\nu)^2$
$(h\nu)$
10
8
6
4
2
0
1.0
1.5
2.0
2.5
3.0

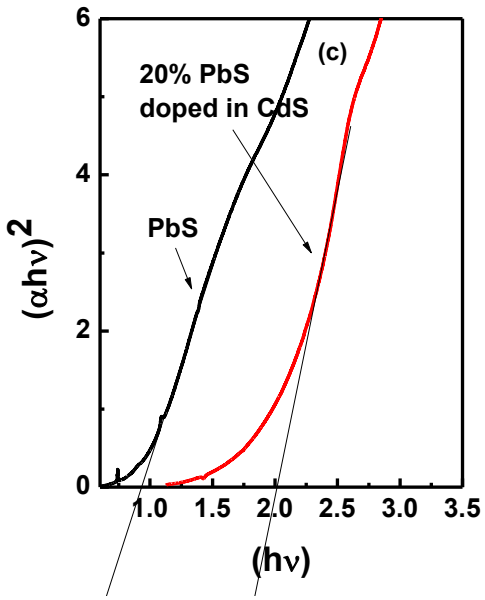
(c)
20% PbS
doped in CdS
PbS
$(\alpha h\nu)^2$
$(h\nu)$
6
4
2
0
1.0
1.5
2.0
2.5
3.0
3.5

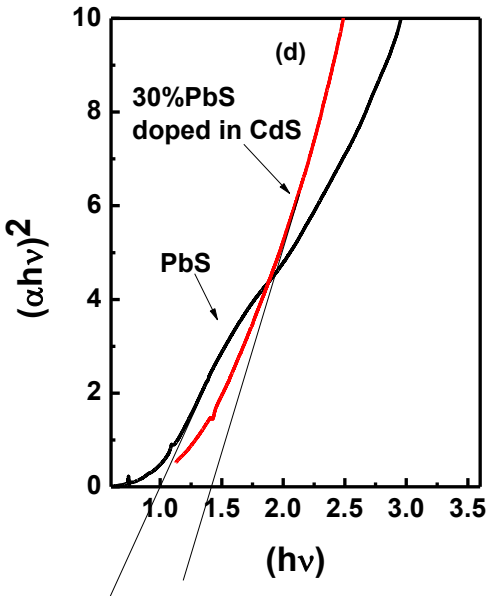

Figure 4.4 Estimation of band gap from Tauc's Plot.

band gap confirms the formation of ternary CdPbS alloy and the existence of strong quantum confinement in this system. This could probably be attributed to a decrease in the effective mass and an increase in the binding energy over that in PbS nanocrystals. As mentioned earlier, we observe a systematic increase in the crystallite size with increasing concentrations of PbS in CdS. Since the estimated mean crystallite size in this case being approximately half the value of the exciton Bohr radius in PbS, we observe a strong confinement in CdPbS nanocrystals. Besides, the crystallite size decreases with increasing concentration, which is contrary to the result observed for PbS nanocrystals. This leads us to understand that when concentration increases more Pb^{2+} ions are replaced by Cd^{2+}, which as a result increases the internal strain. As already mentioned, this built in strain would result in a reduction of grain size. In this situation, the composition x of the ($Cd_{1-x}Pb_xS$) solid solution would also increase, and hence an increase in the band gap is anticipated.It obviously enlightens that the large shift in the band gap of CdPbS in our case is a combined result of confinement effect and formation of ternary CdPbS.

4.3(c) Structural Property –XRD study

Fig. 4.5 (i) shows the XRD spectra of pure CdS and Pb-doped CdS nanoparticles synthesized at a temperature of 120^0C. Fig. 4.5(ii) shows XRD spectra of pure PbS nanoparticles synthesized at a temperature of 120^0C. In the case of PbS, we observe sharp peaks at $2\theta = 26.6^0$, 30.7^0, 43.6^0, and 51.5^0. The observed peak positions are consistent with the fcc structure of PbS (JCPDS-65-0241) and they are represented by their corresponding Miller indices (111),(200),(220) and (311) in the spectra. The appearance of sharp peaks reveals the bulk nature of these nanoparticles. However, we noticed a small shift (~0.5%) in the position of all the peaks towards higher values, compared to the standard values of bulk PbS. Such a marginal shift in the diffraction peaks can be attributed to lattice strain resulting due to any structural disorder generated during the nanoparticles growth. Moreover, the absence of any other peaks corresponding to metallic clusters and/or impurities reveals good quality of the material. The average crystallite size (D) was estimated using the Debye–Scherrer formula [5]. The value of D was found to be 32nm for PbS nanocrystals corresponding to plane (220) at $2\theta = 43.75^0$. A comparison of XRD line shapes of PbS and CdPbS nanoparticles clearly indicates a significant broadening after doping. There are two main possible causes for the peak broadening. The first is increase in heterogeneity of the films due to the occupation of Cd into the host lattice. A second cause is a decrease in crystallite size. It can be mentioned that the stable crystal structure of PbS (fcc) differs from that of CdS (hexagonal close packed) However, the(110), (103), and (1l2) planes of wurtzite CdS are clearly distinguishable in the diffraction pattern at $2\theta = 24.69^0$,$26.29^0$and 27.67^0 respectively,other hexagonal peaks are observed at (002),(100) and(101) at $2\theta = 43.42^0$,47.02^0 and 51.4^0respectively which are consistent from JCPDS card(no.65-3414). As a result, when Cd^{2+} occupies more and more sites of Pb^{2+} in the host lattice, internal strain would arise, and the crystal structure of the

CdPbS solid solution becomes unstable. In order to stabilize the crystal structure, the grain size is reduced to release the strain .As the Pb concentration is increased, the diffraction peaks become broader due to a reduction in the grain size[10]. The value of D calculated for CdPbS nanoparticles was found to be in the range of 8-16nm corresponding to plane (220) at $2\theta=43.75^0$. It is also noted that the intensity of the diffraction peaks decreases after doping. This can be attributed to doping induced structural disorder in the nanocrystals.[11]. . Moreover, we observed a decrease in the lattice d spacing of CdPbS nanocrystals compared to the corresponding values in PbS nanocrystals. This confirms the formation of CdPbS, because when Cd^{2+} occupies the Pb^{2+} sites in the lattice, the lattice would undergo a contraction due to smaller ionic radii of Cd^{2+}[12].

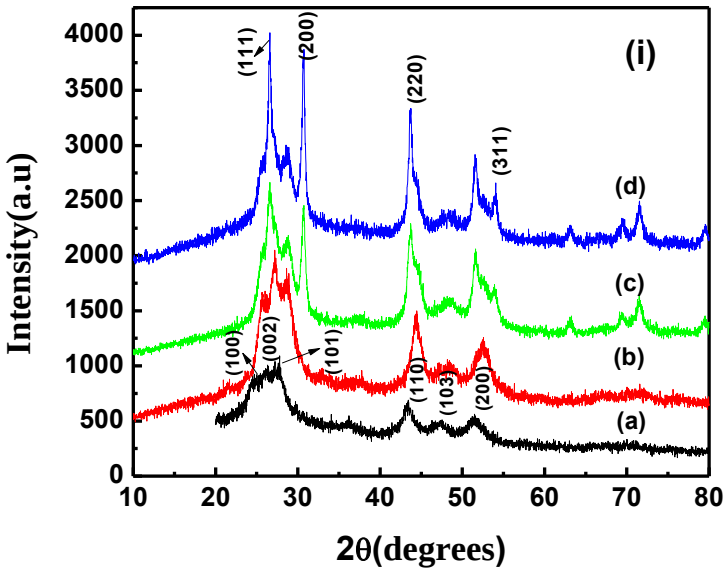

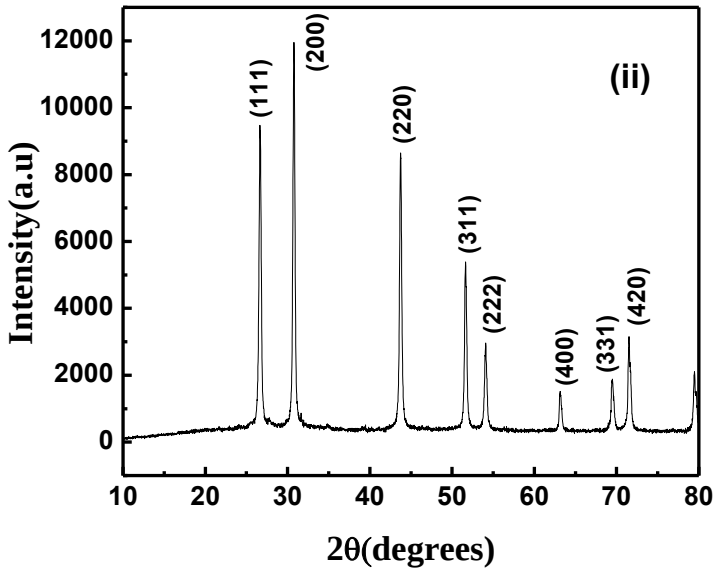

Figure 4.5 X-ray diffraction spectra of (i) (a)CdS (b)10% CbPdS (c)20%CdPbS (d)30%CdPbS nanocrystalline thin films deposited at a temperature of 120^{0}C . (ii) X-ray diffraction spectra of PbS deposited at a temperature of 120^{0}C.

4.3(d) Structural Property-SEM and EDS studies

SEM images of PbS and CdPbS nanoparticles grown at 120^{0}C are shown in Fig. 4.8 along with EDS shown in Fig. 4.6 and Fig. 4.7. It can be seen that the surface of undoped PbS nanoparticles is composed of pyramidal and disc-shaped nanocrystals of different dimensions and sizes. It should be noted that the average crystallite sizes deduced from the Scherrer formula are much lower than the grain sizes observable in the SEM pictures. However, grains in the sizes less than a 100nm are also evident in the micrograph. The observed discrepancy can be probably due to the non-spherical geometry of the

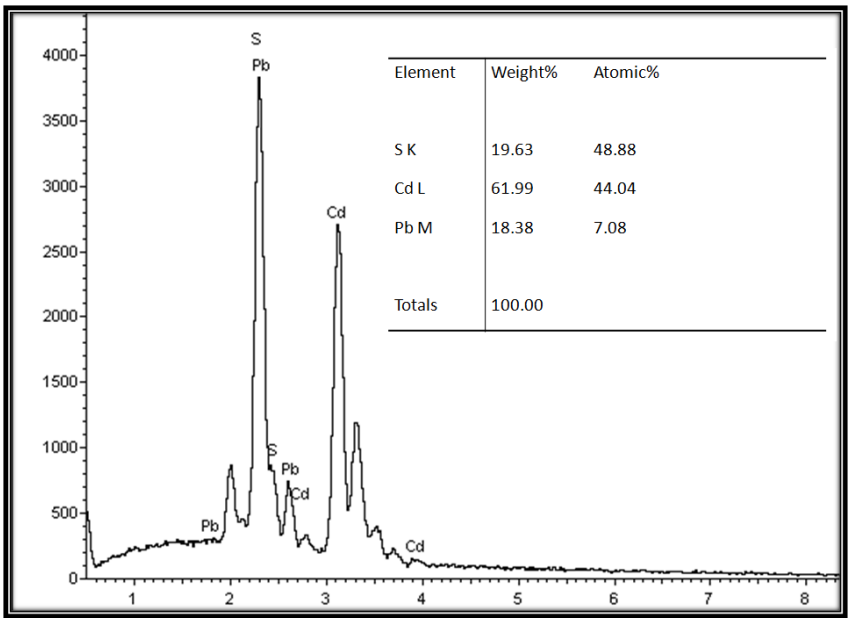

Figure 4.6 EDS spectrum of CdPbS

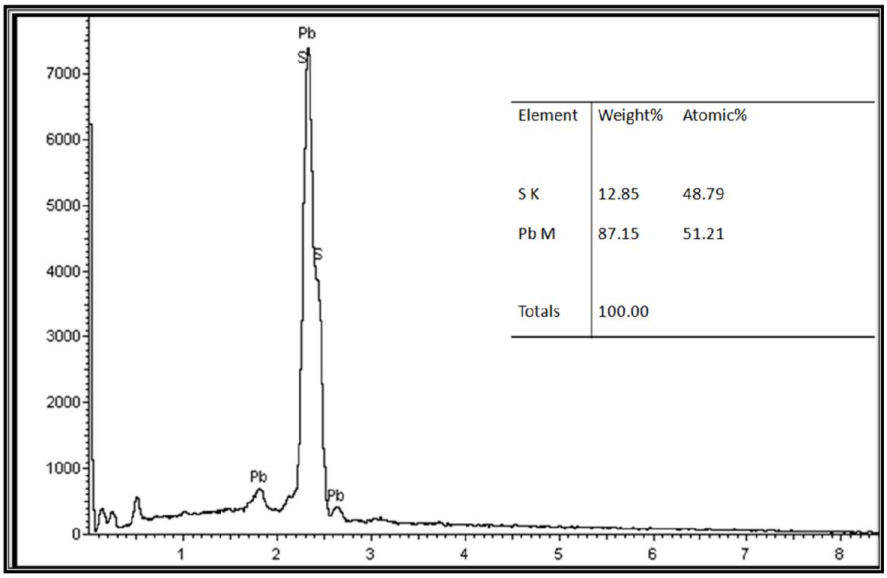

Figure 4.7 EDS spectrum of PbS

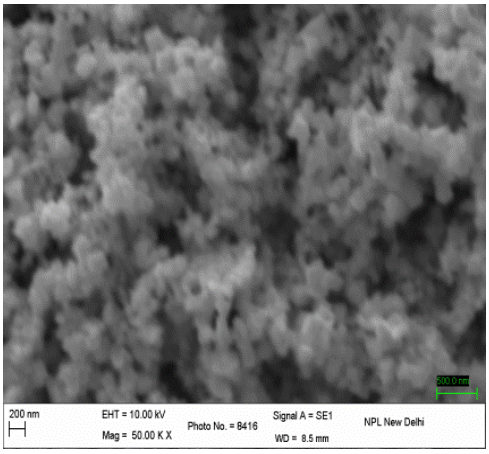

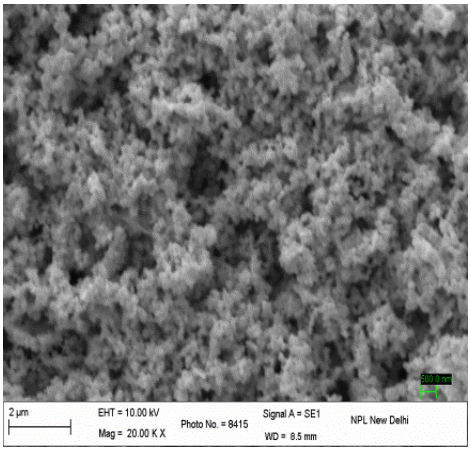

(a)

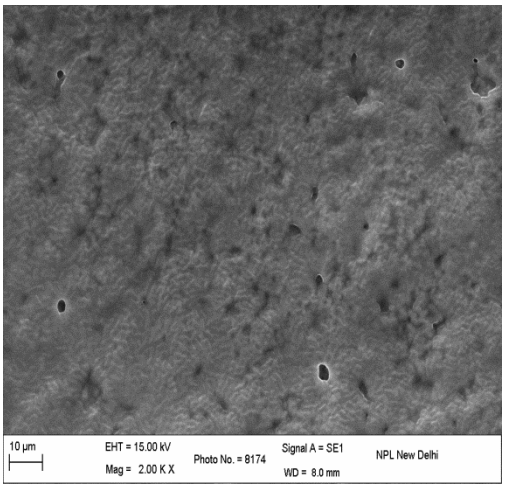

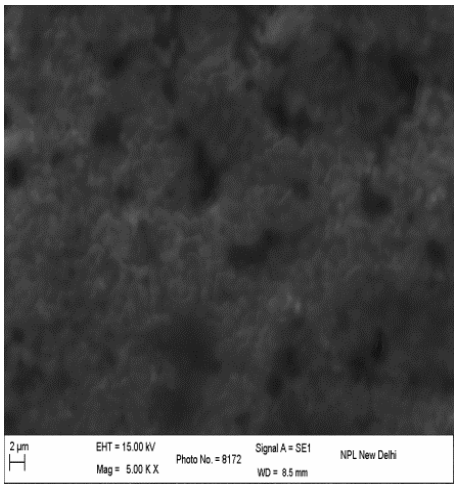

(b)

Figure 4.8 SEM Images of (a)PbS (b) CdPbS prepared at 120^0C

nanocrystallites. In fact, it is anticipated in the case of nanocrystalline thin films that the domains have a tendency to increase its size near the film surface, thus SEM images representing the surface features of the film, give maximum possible size of grains[13]. On the other hand,crystallite sizes calculated using the XRD data is thickness averaged magnitude, which usually dominated by the smallest crystallites[14].

Similar discrepancy has been reported for various thin films. The addition of Cd into the solution modifies the thin film growth. Here, any pyramidal- or disc-shaped structures have not been observed and the morphology of the films how shows aggregates of finite particles. Although individual particles are not clearly visible with this magnification, the morphology clearly reveals a strong agglomeration of finite particles.To further investigate the composition of the PbS and CdSPb in composite film, the energy dispersive X-ray spectroscope (EDS) spectrum Fig. 4.6 and Fig. 4.7 was obtained. EDS analysis of the PbS and CdPbS demonstrates that the chemical component consists of Pb,S and Cd, Pb, S. and Table shows approximate relative ratio of Pb: S~1:1 and Cd:Pb:S~6:1:6. This ratio agrees with the nominal PbS and CdPbS statiometry.

4.3(e) Structural Property- TEM Study

Transmission electron microscopy (TEM) image and electron diffraction patterns of the synthesized CdPbS nanoparticles at 120 °C are shown in Fig. 4.9. Fig. 4.9(a) and Fig. 4.9(b) shows the formation small sized monodispersed circled CdPbS nanoparticles of average size 8-16nm. Fig. 4.9(c) shows the high magnification images of corresponding nanoparticles ,the presence of sharper lattice fringes in high-resolution image shows crystallnity of nanoparticles and these results are good agreement with XRD results nanoparticles.

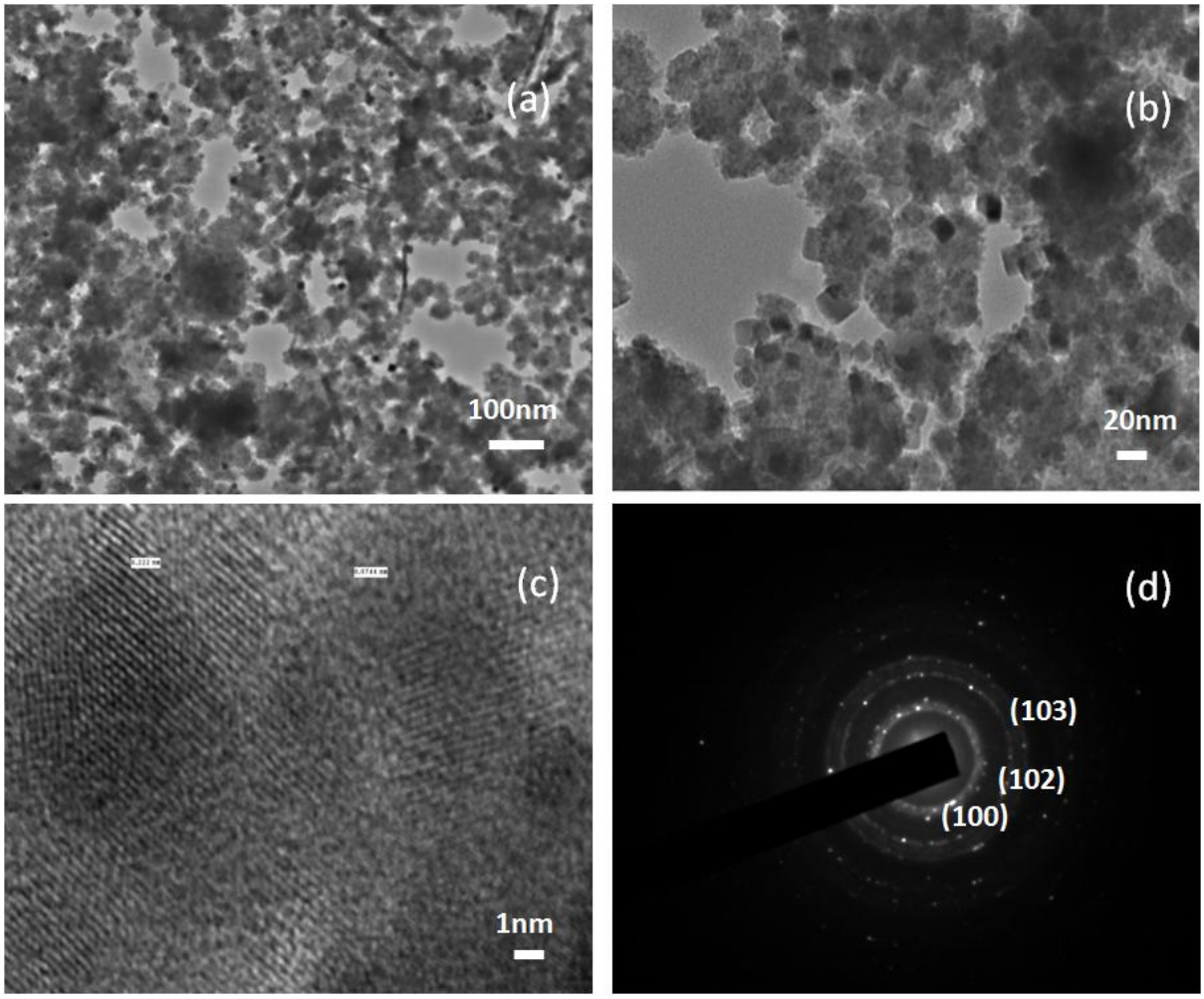

Figure 4.9 (a),(b)TEM Images of 30%PbS doped in CdS (c)-HRTEM images of CdPbS nanocrystals (d)-SAED pattern of CdPbS nanocrystals.

The selected area electron diffraction pattern (SAED) of CdPbS nanocrystal in Fig. 4.9(d) confirms the single crystalline nature of nanoparticles and the CdPbS nanoparticles with plane (100), (102) and (103) of diffraction rings, corresponding to d spacing 3.5nm, 2.45nm and 1.9nm.

4.4 Conclusions

In situ Pb-doping is found to induce considerable modifications in theoptical bandgap of CdS nanocrystalline thin films.It is experimentally shown that the band gap of CdS can be engineered over a wide range (2.7eV–0.7eV) by changing the deposition conditions and introducing the Pb metal impurities.We observed strong quantum confinement effect in the case of CdPbS films. These properties could potentially be utilized to harvest maximum photon energy from the sunlight to enhance the photovoltaic performance. Since the band gap could be tuned to cover the entire visible region, CdPbS nanostructured films would be a promising candidate for solar cell applications.

4.5 References

1. S.A. McDonald, G. Konstantatos, S. Zhang, P.W. Cyr, E.J.D. Klem, L. Levina, E.H.Sargent, Nature Mater. 4 (2005) 138.
2. K.W. Johnston, A.G. Pattantyus-Abraham, J.P. Clifford, S.H. Myrskog, D.D. MacNeil, L. Levina, E.H. Sargent, Appl. Phys. Lett. 92 (2008) 151115.
3. Shu Fen Wang, Feng Gu, Meng Kai Lu, Langmuir 22 (2006) 398.
4. R.K. Joshi, A. Kanjilal, H.K. Sehgal, Appl. Surf. Sci. 221 (2004) 43.
5. K.K. Nanda, S.N. Sahu, Adv. Mater. 13 (2001) 280.
6. G. Zhou, M. Lü, Z. Xiu, S. Wang, H. Zhang, Y. Zhou, S. Wang, J. Phys. Chem. B 110(2006) 6543.
7. E. Rabinovich, E. Wachtel, G. Hodes, Thin Solid Films 517 (2008) 737.
8. A.Ounissi, N. Ouddai, S. Achour, Eur. Phys. J. Appl. Phys. 37 (2007) 241.

9. E. Pentia, V. Draghici, G. Sarau, B. Mereu, L. Pintilie, F. Sava, M. Popescu,J.Electrochem. Soc. 151 (2004) G729.
10. C.T. Tsai, S.H. Chen, D.S. Chuu, Phys. Rev. B 54 (1996)11555
11. H.K. Yadav, K. Sreenivas, R.S. Katiyar, V. Gupta, J. Phys. D: Appl. Phys. 40 (2007) 6005.
12. N. Badera, B. Godbole, S.B. Srivastava, P.N. Vishwakarma, L.S.S. Chandra, D. Jain,M. Gangrade, T. Shripathi, V.G.Sathe,V.Ganesan, Appl. Surf. Sci. 254 (2008)7042.
13. G.Korotcenkov,A.Cornet,E.Rossinyol,J.Arbiol,V.Brinzari,Y.Blinov,ThinSolidFilms 471 (2005) 310.
14. K.P. Acharya, J.R. Skuza, R.A. Lukaszew, C. Liyanage, B. Ullrich, J. Phys.: Condens.Matter 19 (2007) 19622

CHAPTER-5

Direct synthesis of CdS/CdPbS nanocrystals in poly (3-hexylthiophene) polymer for photovoltaic application

5.1 Introduction

Among various semiconductor materials used in solar cells ,CdS/CdPbS and related chalcogenide compounds have attracted a great deal of interest due to their large absorption coefficients, adjustable band gap, low toxicity and long-term stability. They are mostly fabricated *via* a high-cost vacuum-based process such as evaporation and sputtering on Mo coated glass substrates. Vacuum-based set-ups and control systems require large capital investment. In contrast, nanocrystals (NCs) can be used as nanocrystal ink that is coated on a substrate to yield a low-cost solar cell, so the synthesis of CdS/CdPbS NCs has attracted great attention. Several synthetic methodologies for the production of CdS/CdPbS NCs have been explored, including hot-injection[1-3], hydrothermal method[4-6] , chemical transformation route[7], thermal decomposition of precursors[8-10] and microwave-assisted synthesis.[11]

An in situ synthetic method was employed to synthesize CdS/CdPbS nanocrystals with P3HT composite and showed that the polymer chains can act sterically to stabilize nanocrystal growth in solution[8-9]. Therefore, development of semiconductor nanocrystals, without the use of surfactants and/or ligands, should be more technically interesting with

improved power-conversion efficiency for a quantum-dot-based photovoltaic device. The P3HT can act here to as a macromolecule that is acting as a structure-directing template to manipulate the geometrical development of CdS/CdPbS nanocrystals and, in the meantime, becoming an efficient photoelectron conductor when the final CdS/CdPbS−P3HT composite structure can be well constructed and is highly plausible for solar cell application.

Hybrid nanocomposites are potential organic photovoltaic device system because of the desirable characteristics of both organic and inorganic components can be included within a single composite material. Such composites show advantage of tunability of photophysical properties of the quantum dots (QDs) and retained the polymer properties like solution processing, fabrication of devices on large and flexible substrates. Due to different electron affinities of QDs and polymer, a built in potential is generated at polymer-QDs interfaces which assist in the charge transfer between polymer and QDs. Up to now, the organic-inorganic hybrid thin film solar cells have shown power conversion efficiency of ∼3% -5%. In conventional synthesis of QDs (CdTe, CdSe), the QDs were capped with organic ligands, such as tri-n-octylphosphine oxide (TOPO) or oleic acid. It is well known that if the QDs are capped with organic ligands, they hinder the efficient electron transfer from the photoexcited polymer to the nanoparticles. To remove the organic ligands, polymer-nanoparticles were usually treated with pyridine. However, pyridine is an immiscible solvent for the polymer and flocculation of the P3HT chains in an excess of pyridine may lead to the large-scale phase separation resulting in poor photovoltaic device performance. To overcome the effects of the capping ligands on charge transport, researchers have directly synthesized uncapped nanoparticles inside the polymer matrix. The *in situ* growth of the nanocrystals in polymer templates controls the dispersion of the inorganic phase in organic phase, thus ensuring a

large, distributed surface area for charge separation. Moreover, nanocrystals are uniformly distributed to the entire device thickness and thus contains a built in percolation pathway for transport of charge carriers to the respective electrodes. Solution-processed photovoltaic devices offer a route for harvesting solar energy that is appealing because of simplified and low-cost device fabrication, large-area coverage, and the possibility of producing mechanically flexible devices. Conjugated polymers have been widely investigated for this purpose and have achieved 6.1% solar power conversion efficiency [12]. Recently, new photovoltaics based on solution-processed inorganic nanocrystals (NCs) have attracted considerable attention, and photovoltaic devices based on systems such as CdTe[13], CdSe[14], Cu_2S[15], PbS[16-17], $Pb(S_x,Se_{1-x})$[1-2], $CuInSe_2$, $CuInS_2$[3-4], $CuInGaS_xSe_{1-x}$[5], and Cu_2ZnSnS_4[6-7] have been demonstrated. Despite their appealing advantages over conjugated polymer technologies, (e.g., a significantly larger carrier mobility), many of the approaches utilizing NCs suffer from the need to synthesize the NC capped with long-chain ligands that act as an insulator in photovoltaic devices, or include an additional ligand-exchange processing step to shorter and more volatile ligands[13-17]. Here we present a simple route for the fabrication of optoelectronic devices that involves film deposition with in situ synthesis, thereby circumventing the need to first synthesize the NCs and then perform a ligand exchange.

The CdS/CdPbS nanocrystal conducting polymer composites used in these opto-electronic applications are produced either by synthesizing the CdS/CdPbS nanocrystals separately and then blending with a conducting polymer or by synthesizing the CdS/CdPbS nanocrystals directly in the conducting polymer. The conventional method for preparing a

nanocrystal−conjugated polymer composite is by mixing a given polymer with nanocrystals through the use of surfactants, where the surfactants would form an insulating interface, even in a nanometric length, between the polymer matrix and the nanocrystals, further deteriorating charge transfer ability[13-14].A variety of methods exists in the literature for the synthesis of ligand-capped metal chalcogenide nanocrystals with controlled size and shape[5-7]. Although the incorporation of the surface ligands into an organic/inorganic composite can improve distribution of nanocrystals in a conjugated polymer, two significant drawbacks ruin the efficiency considerably. First, the ligands inhibit charge transfer between the polymer and the nanocrystals[15]. Second, mixing pyridine-capped nanocrystals and polymer requires the use of cosolvent, which can adversely affect nanocrystal solubility and polymer chain orientation. These problems can be bypassed by directly growing nanocrystals in a conducting polymer solution without surfactants or ligands[8,16].Synthesizing the CdPbS nanocrystals directly in a conducting polymer eliminates the need for mixing and blending and represents the simplest technique for forming nanocomposite materials suitable for opto-electronics. Here we show a new approach to synthesizing monodisperse CdS/CdPbS nanocrystals in a conducting polymer that overcomes the problem of large size distributions that are normally associated with the one-pot procedures. The CdS/CdPbS nanocrystals are synthesized in high temperature boiling point solvent DCB, which allow CdS/CdPbS nucleation to occur at 120°C. In the present protocol, nucleation starts at the decomposition temperatures of the precursor compound in the one pot synthesis, which results in highly crystalline and monodisperse CdS/CdPbS nanocrystals well dispersed in the polymer matrix. In addition, the synthesis strategy reported in this work is a simple one-pot route and may be used as a general process for synthesis of pure or doped NCs. In summary, a facile one-pot synthetic procedure of preparing CdS/CdPbS NCs has been described.

In surfactant-assisted synthesis, nanoparticles growth is controlled by electrostatic interactions of the surfactant functional group and steric hindrance of surfactant side alkyl chains. P3HT provides a combination of both effects as it contains an electron donating sulfur functionality, a potential anchorage for the nucleation, and growth of nanoparticles along with steric hindrance due to long hexyl side chains.

The present investigation reports the synthesis of CdS/CdPbS nanocrystals in P3HT matrix with different concentrations of P3HT and CdS/CdPbS (1:1, 1:2, 1:4 and 1:8). These P3HT-CdS/CdPbS nanocomposites can be synthesized in common solvents for the polymer DCB or chlorobenzene, from which thin films can be readily cast. Structural and morphological study revealed that CdS/CdPbS nanoparticles have been successfully synthesized in P3HT matrix. Optical measurements of nanocomposites films show that photoinduced charge separation occurs at the P3HT-CdS/CdPbS interfaces, indicating this is a promising approach for the fabrication of efficient organic-inorganic hybrid photovoltaic devices.

5.2 Experimental

Synthesis of CdS/CdPbS-P3HT composite

CdS/CdPbS-P3HT nanocomposite of different concentrations were synthesised by the thermolysis of the precursor using standard Schlenck techniques .Different concentrations of P3HT-CdS/CdPbS(1:1, 1:2, 1:4 and 1:8) was taken in a three neck flask, and a few drops of pyridine were mixed to convert it to a pyridium complex, 5 ml of DCB was added as solvent, and it was then heated to 120^0C under an atmosphere of nitrogen, for 30 minutes. The solution was then cooled to room temperature and an excess of methanol was added. The

flocculent precipitate formed was centrifuged and washed with methanol followed by the measurement of the optical absorption spectrum and as dispersion in toluene.

5.3 Results and discussions:-CdS/P3HT nanocomposite

5.3(a) Spectral study (FTIR)

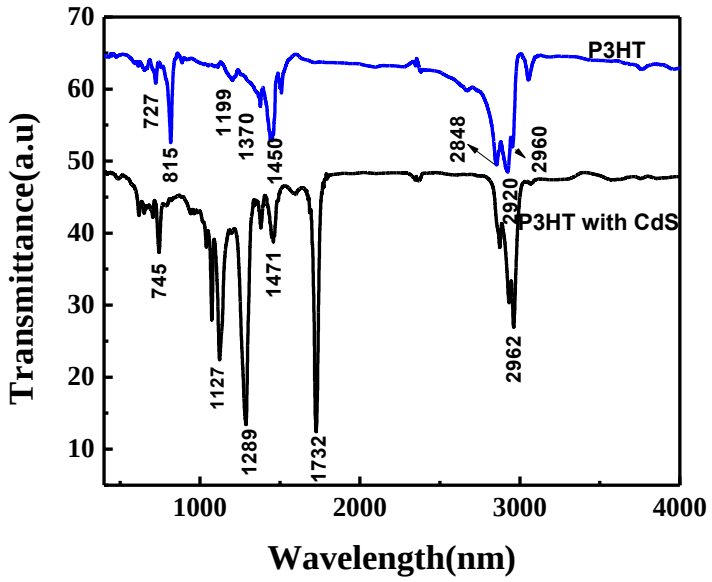

Figure 5.1 FTIR spectra of CdS nanoparticles in P3HT and P3HT

In our case all FTIR spectra were recorded with a single beam Perkin Elmer instrument (Spectrum BX-500) FT-IR Model spectrophotometer.The success of formation of P3HT-CdS nanocomposites have been confirmed by the Fourier transform infra-red (FT-IR) spectra as shown in Fig. 5.1. Strong absorption bands of P3HT at 2960, 2920 and 2848 cm^{-1} have been assigned to the asymmetric C–H stretching vibrations in $–CH_3$, $–CH_2$, and the symmetric C–H stretching vibration in $–CH_2$ respectively. They are ascribed to the alkyl-side chains. The bands at 1450, 1370 cm^{-1} are due to the thiophene ring stretching and methyl deformation respectively. The C-C vibrations appear at 1199 cm^{-1} while absorption band 815 cm^{-1} and

727 cm^{-1} have been assigned to the aromatic C-H out-of plane stretching and methyl rocking respectively. In nanocomposites of P3HT-CdS, the intensity of peaks corresponding to C-S bond and aromatic C-H out-of plane stretching decreases. Also a shift by 25 cm^{-1} (from 1110 to 1135 cm^{-1}), to the higher energy region of C-S characteristic band has been observed in P3HT-CdS, indicating the enhancement of the C-S bond energy. Moreover, the characteristic band of thiophene ring shows a redshift from 822 to 816 cm^{-1} with the increase of concentration of CdS in polymer matrix. These findings suggest additional intermolecular interaction between polymer and nanocrystals which arises due to strong dipole-dipole interaction between the Cd^{2+} ions and S atoms as shown in Fig. 5.1.

5.3(b) Optical Property-UV Study

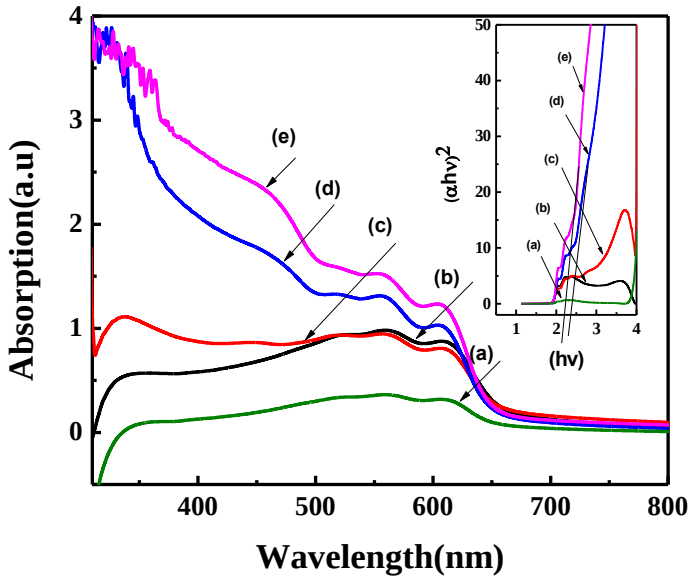

Figure 5.2 Absorption spectra (inset shows Taucs plot) of P3HT and P3HT-CdS nanocomposites films synthesized at different ratio of P3HT and CdS (a) P3HT (b) P3HT with CdS 1:1 (c) P3HT with CdS 1:2 (d) P3HT with CdS 1:4 (e) P3HT with CdS 1:8.

CdS nanocrystals synthesized directly in the conducting polymer, P3HT, are specifically designed for opto-electronic applications. This makes it important to examine the changes in the steady-state absorption and photoluminescence spectra due to the formation of the CdS nancorystals. Fig.5.2 shows the UV–Visible absorption spectra of CdS-polymer nanocomposite. The heating to 110ºC starts decomposition of xanthates and CdS nucleation and the consequent formation of CdS nanocrystals. The CdS nanocrystals absorb well from the near-IR through to the UV and thus add significantly to the total absorbance measured in the composite solution as compared to the pure P3HT solution. Care was taken to ensure that the concentration of P3HT in all solutions was kept constant. This allows any changes in the optical spectra to be attributed to the CdS nancorystals. The peaks in the absorption spectra in Fig.5.2, at 450 and 610 nm, are attributed to the P3HT [12] which corresponds to the π-π* transition of the conjugated chain in the P3HT [11,16]. The samples with CdS additions however present a strong adsorption within a broad range between 400 and 600 nm, the intensity of which increases with the concentration of CdS additive, which is the characteristic absorption of the CdS material. Since CdS is a direct transition semiconductor, its absorption coefficient (α) and bang-gap (E_g) satisfy the equation:

$$(\alpha h\nu)^2 = A(h\nu - E_g) \qquad (1)$$

The band gap (E_g) is obtained by extrapolation of the plot of $(\alpha h\nu)^2$ *vs.* ($h\nu$) as in Fig 5.2(inset) and the taucs plot shows the band gap of CdS –polymer nanocomposite changes from 3.7 eV, to 2.2 eV as we increase the concentration of CdX from 0 to 120 mg these results revels with increase in polymer concentration the particle size of CdS is decreases as the band gap increases.

5.3(c) Optical Property-PL Study

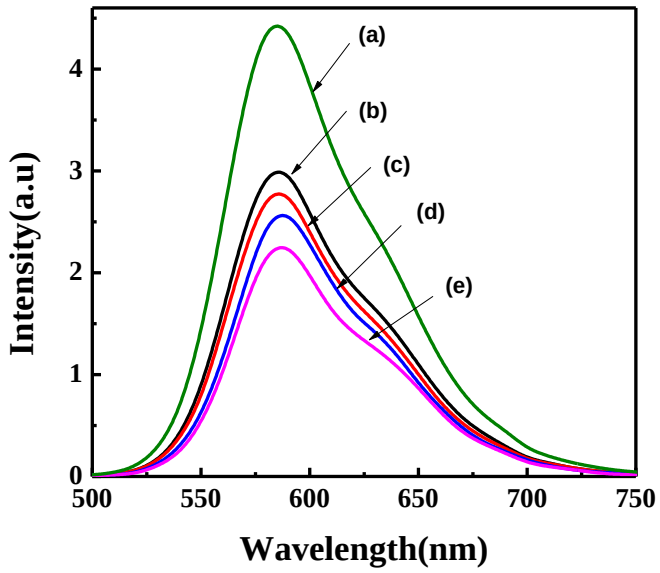

Figure 5.3 PL spectra of P3HT and P3HT-CdS nanocomposites synthesized at different ratio of P3HT and CdS (a) P3HT (b) P3HT with CdS 1:1 (c) P3HT with CdS 1:2 (d) P3HT with CdS 1:4 (e) P3HT with CdS 1:8

Fig. 5.3 show the photoluminescence emission spectra of P3HT and CdS/P3HT composites.fig. shows there is a decrease in the intensity of this photoluminescence as we increase the concentration of CdX and the reduction of PL intensity is increased with increasing concentration of CdS in the composite matrix This reduction of PL intensity is due to the CdS nanocrystals formation in polymer matrix also due to photogenerated charge transfer between the CdS and P3HT[19]. The photoluminescence quenching can be used as a powerful tool for evaluation of charge transfer from the excited polymer to the nanoparticles. Once the photogenerated excitons are dissociated, the probability for recombination should be significantly reduced. Reduced PL intensity of the composites relative to the pristine

P3HT indicates that charge transfer, thereby exciton dissociation at interface of CdS and P3HT occurred. This PL quenching experiment provides us with good evidence that the nanoparticles will be able to transfer their excited state hole to the polymer. Charge transfer takes place in conjugated polymer-semiconductor nanocrystals composites at the interface where the P3HT with a higher electron affinity transferred electron onto CdS with relatively lower electron affinity. In conversion, the polymer absorb the solar photons (charge generation), the electron is transferred to the CdS nanocrystals and the hole potentially can transfer to the polymer (charge separation). This is a well known effect of the ultrafast electron transfer from the donor to acceptor, and it is expected to increase the exciton dissociation efficiency in photovoltaic devices.

5.3(d) Optical Property-Time Resolved Fluoroscence Study

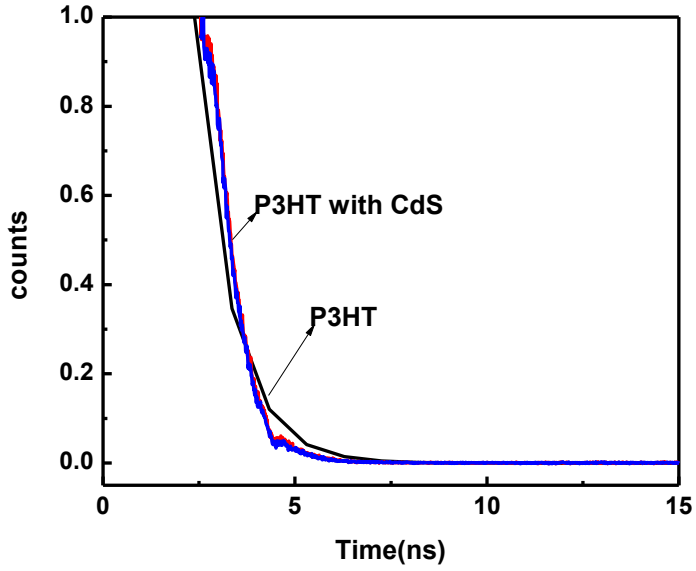

Figure 5.4 Time Resolved Fluorescence studies of P3HT and P3HT with CdS

In order to understand electron transfer dynamics, lifetime measurement studies were performed. Fig. 5.4 shows the PL decay curves for P3HT and P3HT–CdS nanocomposites. The rate of PL decay times at which the PL intensity decreases to 1/e of its initial value are used to compare the life time of P3HT and P3HT-CdS.

The emission intensity recorded at the emission maximum exhibited a monoexponential decay

$$I(t) = A \exp(-t/\Gamma)$$

where I is the normalized emission intensity, A is pre-exponential factor, t is the time after pulsed-laser excitation, and Γ is lifetime. The decays of both samples are fitted with single exponential. Excitation Wavelength used in these measurements is 480nm.The kinetic parameters of the P3HT and P3HT-CdS emission decay analysis are summarized in Table 1.

These result shows the life time of P3HT decreased from 0.92 ns to 0.8 ns on addition of CdS indicates efficient charge transfer in P3HT-CdS nanocomposite. Also there is more decrease in lifetime values inP3HT–CdS nanocomposites as we increase the amount of CdS .These results commensurate well with PL quenching results were higher PL quenching was obtained for nanocomposites with CdS(60 mg) as compared with CdS(15 mg).

.

	Γ(ns)
P3HT	0.92115
P3HTwith CdS(15 mg)	0.82137
P3HTwith CdS(60 mg)	0.80389

Table 1: TRF data

5.3(e) Structural Property-XRD Study

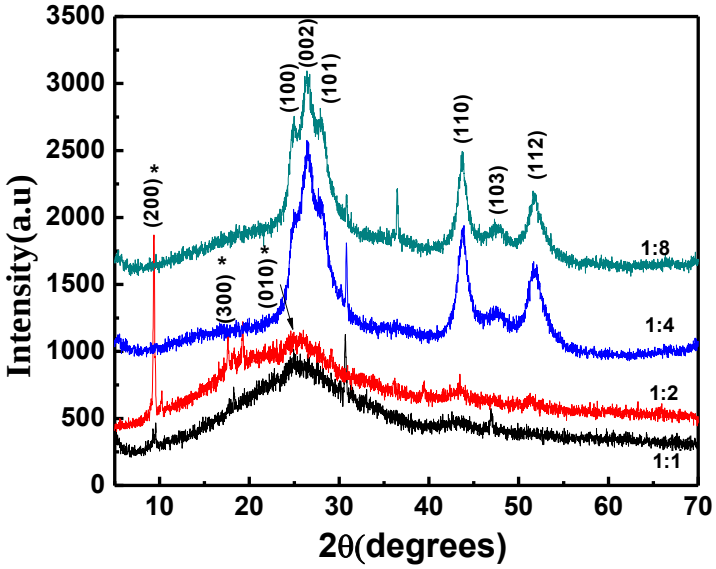

Figure 5.5 XRD Spectra of P3HT-CdS nanocomposite at different concentrations

Fig. 5.5 shows the diffraction patterns of polymer, CdS and P3HT-CdS nanocomposites this XRD analysis confirmed the in situ formation of CdS nanoparticles. The diffraction peaks at, (200),(300) and (010) can be associated with the P3HT as reported by C. Borreiello et al and S. Masala et a and at 24.99 26.53 27.92 43.83 47.79 51.75 may be assigned to (100) (002) (101) (110) (103) (112)planes of the CdS material, respectively, which are consistent with those in the literature[3] and from the JCPDS card (no. 65-3414) confirms the formation of Hexagonal phase of CdS nanoparticle in polymer nanocomposites. The crystalline peaks of P3HT decreases as we increased the ratio of nanoparticle precursor in polymer nanoparticle

composite. The dimension of CdS nanoparticle in nanocomposite and CdS without composite can be calculated using Scherrer equation [19]

$$d=0.9\lambda/\beta Cos\theta$$

where β is the line width at an angle 2θ λ is X-ray wave length.

Using this formula we can observe the particle size of CdS nanoparicle without polymer is 7 nm and for nanocomposites of polymer :CdS 1:8 and 1:4 is 6 nm and 5nm respectively shows as we increase the amount of polymer the in polymer nanoparticle composite precursor the particle size is decreases. Here the P3HT can act as a macromolecule template to control the geometrical development of CdS nanocrystals.

5.3(f) Structural Property-SEM Study

In order to understand the morphology of as synthesized CdS nanoparticles in polymer matrix scanning electron microscopy (SEM) was preformed. Fig.5.6. gives the typical morphologies of the P3HT-CdS films prepared at 120 °C with CdS of 60 mg. shows the presence of large micrometersized agglomerates on the film surface, show CdS nanoparticles uniformly distributed over the film surface

To further investigate the composition of the CdS in composite film, the energy dispersive X-ray spectroscope (EDS) spectrum (Fig 5.6) was obtained. EDS analysis of the CdS-polymer composite demonstrates that the chemical component consists of Cd, C, Cl and S. and Table shows approximate relative ratio of Cd: S ≈1 : 1. This ratio agrees with the nominal CdS statiometry.

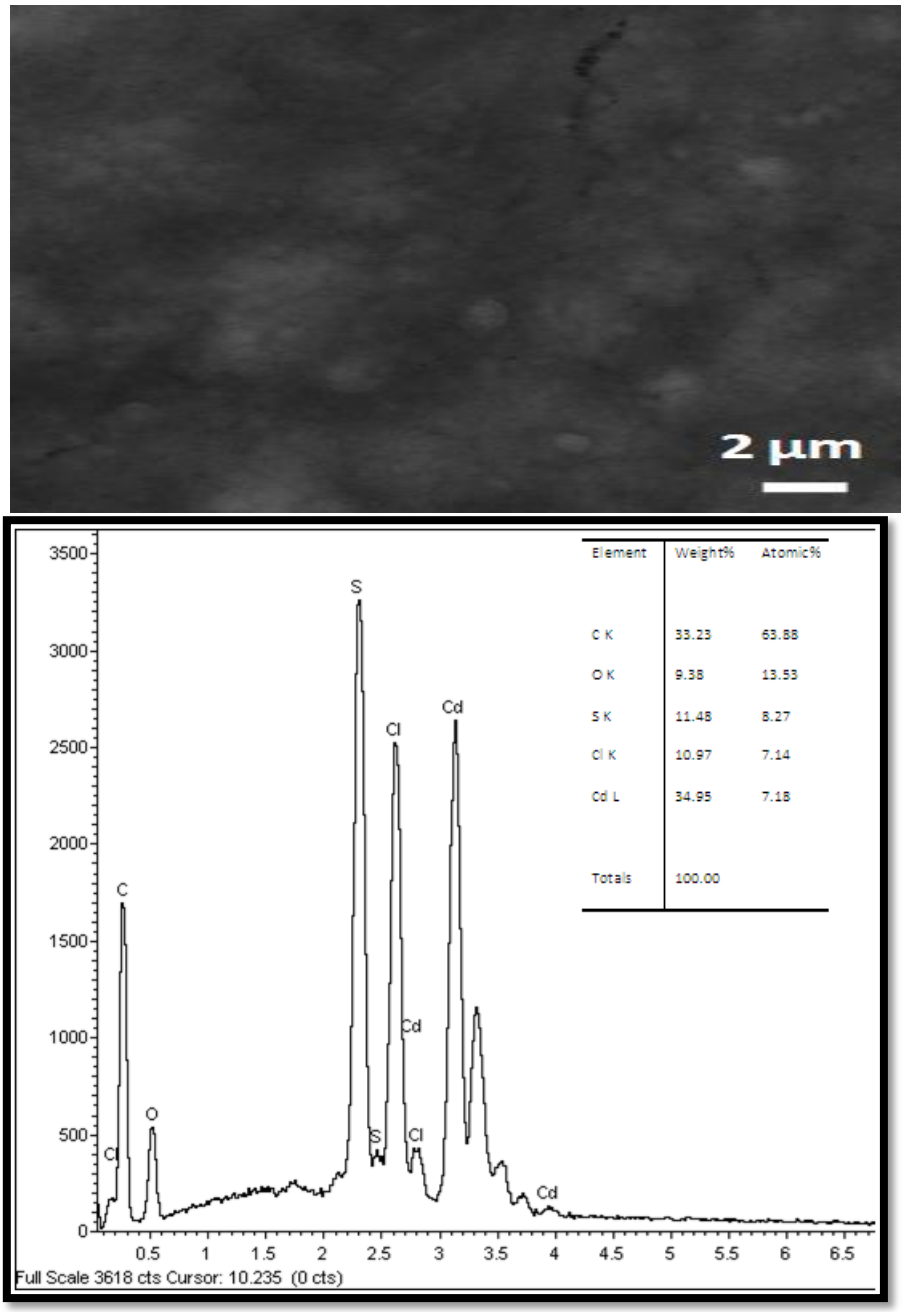

Figure 5.6 SEM micrographs and EDS of CdS nanoparticles in P3HT

5.3(g) Structural Property-AFM Study

The three-dimensional AFM images of neat P3HT and P3HT-CdS nanocomposites are shown in Fig 5.7. The AFM image of the neat P3HT film (above) shows closely packed polymer

nodules, leading to a rather high surface roughness of 40 nm. Contrary to this, the images of the P3HT-CdS nanocomposite (below) reveal a relatively smooth featureless topography and the surface roughness was about 18 nm. The ability of P3HT-CdS film to soak more electrolyte permits a larger ion loading (for the same value of applied potential) and this leads to an improved redox activity and higher contrast ratio in comparison to neat P3HT.

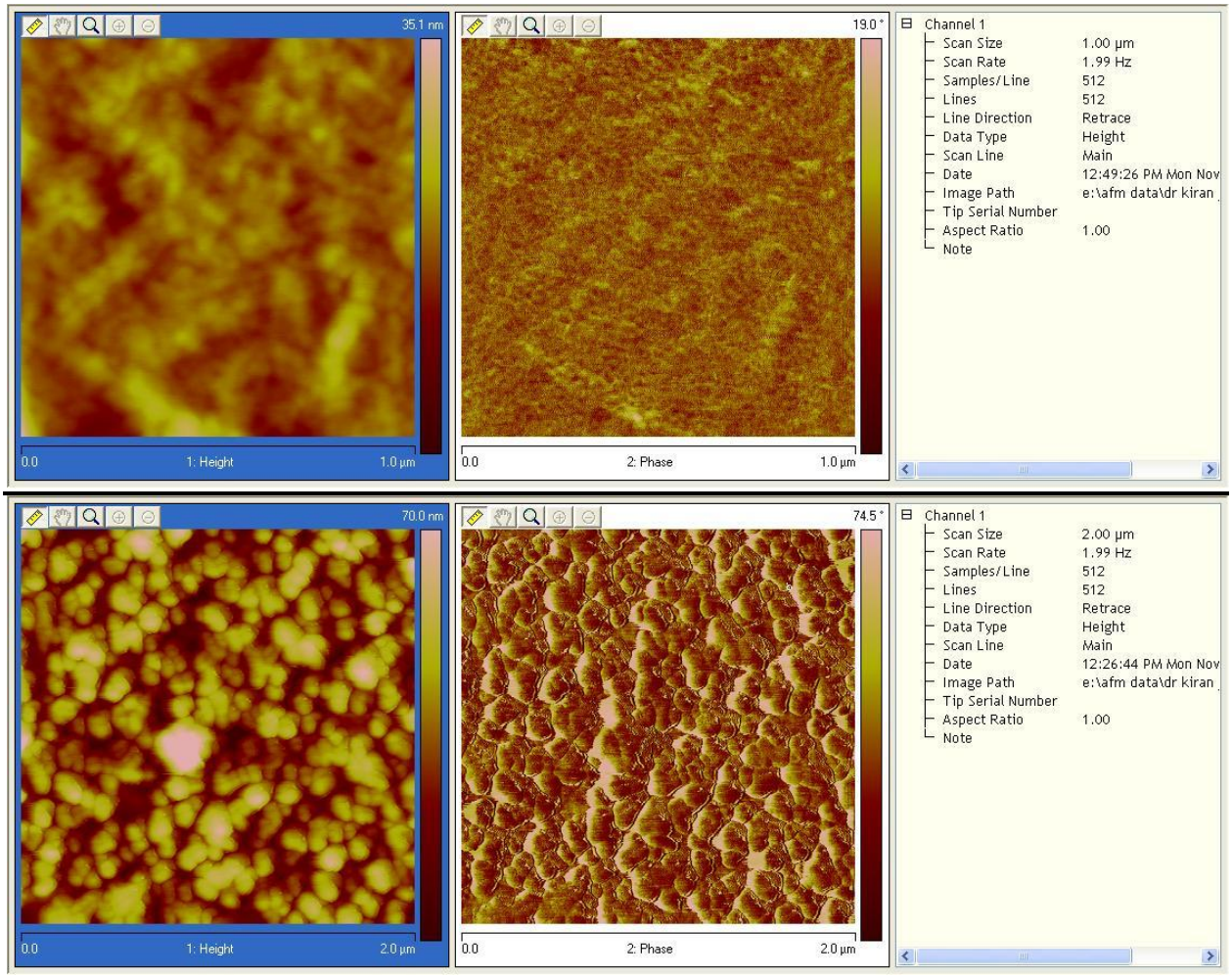

Figure 5.7 AFM Images of P3HT and P3HT-CdS nanocomposite

5.3 (h) Structural Property-TEM Study

Transmission electron microscopy (TEM) image and electron diffraction patterns of the synthesized P3HT-CdS nanocomposites 1:4 at 110 °C are shown in Fig.5.8 as in Fig.5.8 (a),(b),(c) A difference in contrast at different places indicates that the CdS nanocrystals are capped by P3HT. However, this interaction between polymer and nanoparticles indicates that

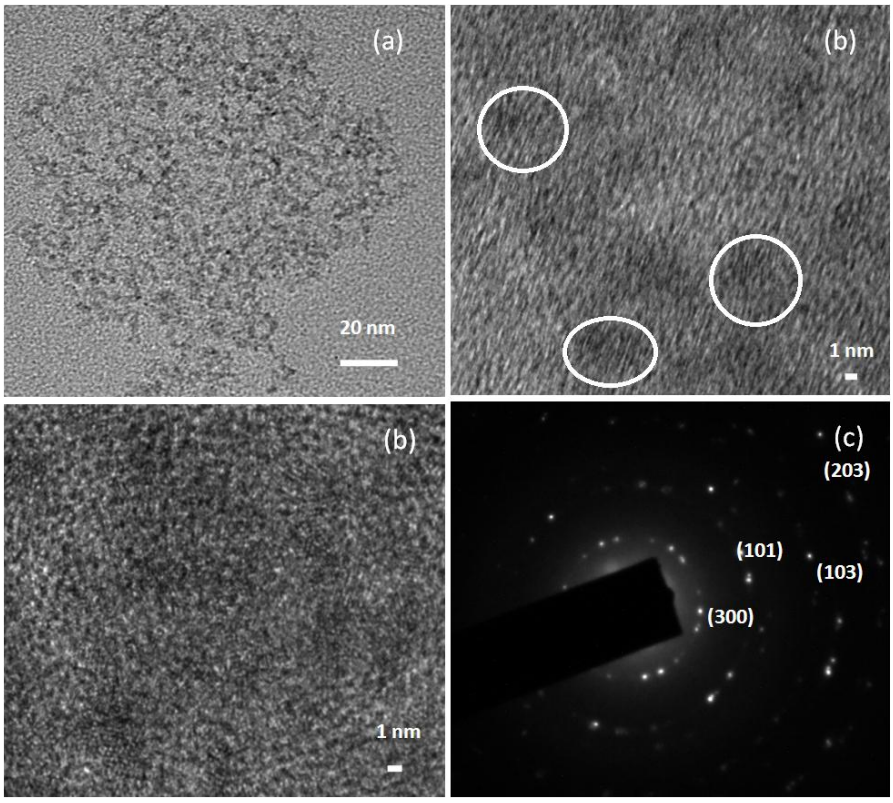

Figure 5.8 (a)TEM images of the synthesized P3HT-CdS (1:4) at 120 °C (b)-HRTEM images of P3HT-CdS (c)-SAED Pattern of P3HT- CdS

nanocomposites have potential for the charge transfer at polymer-nanoparticles interfaces, which results in the PL quenching. The mechanism of this interaction has revealed that the sulfur atom of P3HT can interact with the CdS nanoparticles by dipole-dipole interaction and CdS nanocrystals have been deposited uniformly and compactly on or in-between the P3HT

chains to form nanoparticles Fig. 5.8(a) shows the formation small sized monodispersed circled CdS nanoparticles of average size 4nm. Fig.5.8 (b) shows the high magnification images of corresponding nanoparticles ,the presence of sharper lattice fringes in high-resolution image shows crystallnity of nanoparticles and these results are good agreement with XRD results nanoparticles.The selected area electron diffraction pattern of CdS nanocrystal(Fig.5.8(c)) confirms the single crystalline nature of nanoparticles and the CdS nanoparticles with plane (101), (103) and (203) of diffraction rings, corresponding to d spacing 3.135nm, 1.9nm and 1.36nm.Plane (300) of diffraction ring corresponding to d spacing 4.96nm denotes the Polymer i.e P3HT.

5.4 Results and discussions: - CdPbS/P3HT nanocomposite

5.4(a) Spectral study (FTIR)

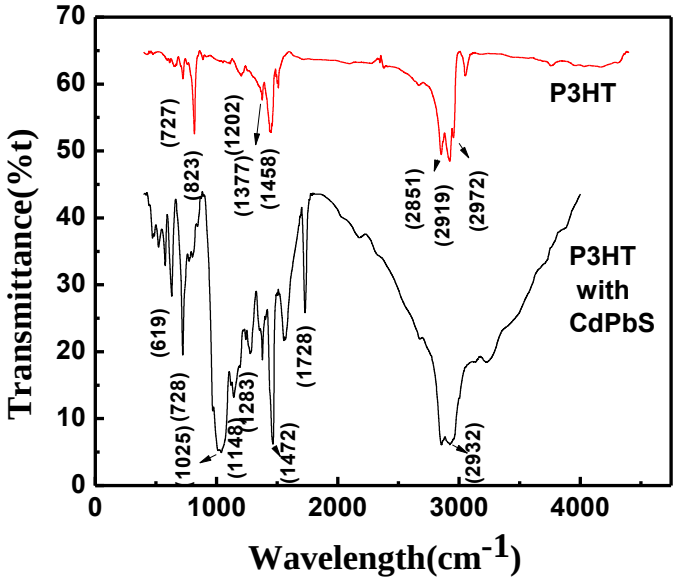

Figure 5.9 FTIR spectra of CdPbS nanoparticles in P3HT and P3HT

In our case all FTIR spectra were recorded with a single beam Perkin Elmer instrument (Spectrum BX-500) FT-IR Model spectrophotometer.The success of formation of P3HT-CdPbS nanocomposites have been confirmed by the Fourier transform infra-red (FT-IR) spectra as shown in Fig.5.9. Strong absorption bands of P3HT at 2851, 2919 and 2972 cm^{-1} have been assigned to the asymmetric C–H stretching vibrations in $–CH_3$, $–CH_2$, and the symmetric C–H stretching vibration in $–CH_2$ respectively. They are ascribed to the alkyl-side chains. The bands at 1458, 1377 cm^{-1} are due to the thiophene ring stretching and methyl deformation respectively. The C-C vibrations appear at 1202 cm^{-1} while absorption band at 823 cm^{-1} and 727 cm^{-1} have been assigned to the aromatic C-H out-of plane stretching and methyl rocking respectively. In nanocomposites of P3HT-CdS, the intensity of peaks corresponding to C-S bond and aromatic C-H out-of plane stretching decreases. Also a shift by 25 cm^{-1} (from 1110 to 1135 cm^{-1}), to the higher energy region of C-S characteristic band has been observed in P3HT-CdPbS, indicating the enhancement of the C-S bond energy. Moreover, the characteristic band of thiophene ring shows a redshift from 822 to 816 cm^{-1} with the increase of concentration of CdPbS in polymer matrix.

5.4(b) Optical Property-UV Study

CdPbS nanocrystals synthesized directly in the conducting polymer, P3HT, are specifically designed for opto-electronic applications. This makes it important to examine the changes in the steady-state absorption and photoluminescence spectra due to the formation of the CdPbS nancorystals. Fig. 5.10(A) shows the UV–Visible absorption spectra of CdPbS-polymer nanocomposite. The heating to 120ºC starts decomposition of xanthates and CdPbS nucleation and the consequent formation of CdPbS nanocrystals.

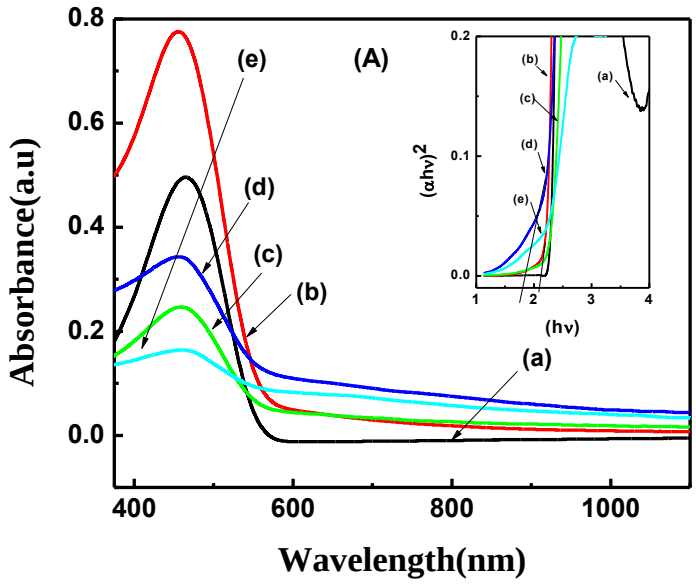

Fig. 5.10 (A) Absorption spectra (inset shows Tauc's plot) of P3HT and P3HT-CdPbS nanocomposites films synthesized at different ratio of P3HT and CdPbS (a) P3HT (b) P3HT with CdPbS 1:1 (c) P3HT with CdPbS 1:2 (d) P3HT with CdPbS 1:4 (e) P3HT with CdPbS 1:8.

The CdPbS nanocrystals absorb well from the near-IR through to the UV and thus add significantly to the total absorbance measured in the composite solution as compared to the pure P3HT solution. Care was taken to ensure that the concentration of P3HT in all solutions was kept constant. This allows any changes in the optical spectra to be attributed to the CdPbS nancorystals. The peaks in the absorption spectra in Fig. 5.10(A) at 500 nm, are attributed to the P3HT[12] which corresponds to the π-π* transition of the conjugated chain in the P3HT[11-16] and the samples with CdPbS additions however present a strong adsorption within a broad range between 400 and 600 nm, the intensity of which increases with the concentration of CdPbS additive, which is the characteristic absorption of the CdPbS

material. Since CdPbS is a direct transition semiconductor, its absorption coefficient (α) and bang-gap (E_g) satisfy the equation:

$$(\alpha h\nu)^2 = A(h\nu - E_g) \qquad (1)$$

The band gap (E_g) is obtained by extrapolation of the plot of $(\alpha h\nu)^2$ *vs.* ($h\nu$) as in Fig. 5.10(inset) and the taucs plot shows the band gap of CdPbS –polymer nanocomposite changes from 2.3 eV, to 1.7 eV as we increase the concentration of CdPbX from 0 to 120 mg these results reveals with increase in polymer concentration the particle size of CdPbS is decreases as the band gap increases.

5.4(c) Optical Property-PL Study

Fig. 5.11 shows the photoluminescence emission spectra of P3HT and CdPbS/P3HT composites.It shows there is a decrease in the intensity of this photoluminescence as we increase the concentration of CdPbX and the reduction of PL intensity is increased with increasing concentration of CdPbS in the composite matrix This reduction of PL intensity is due to the CdPbS nanocrystals formation in polymer matrix also due to photogenerated charge transfer between the CdPbS and P3HT. The photoluminescence quenching can be used as a powerful tool for evaluation of charge transfer from the excited polymer to the nanoparticles.

Once the photogenerated excitons are dissociated, the probability for recombination should be significantly reduced. Reduced PL intensity of the composites relative to the pristine P3HT indicates that charge transfer, thereby exciton dissociation at interface of CdPbS and

P3HT occurred. This PL quenching experiment provides us with good evidence that the nanoparticles will be able to transfer their excited state hole to the polymer.

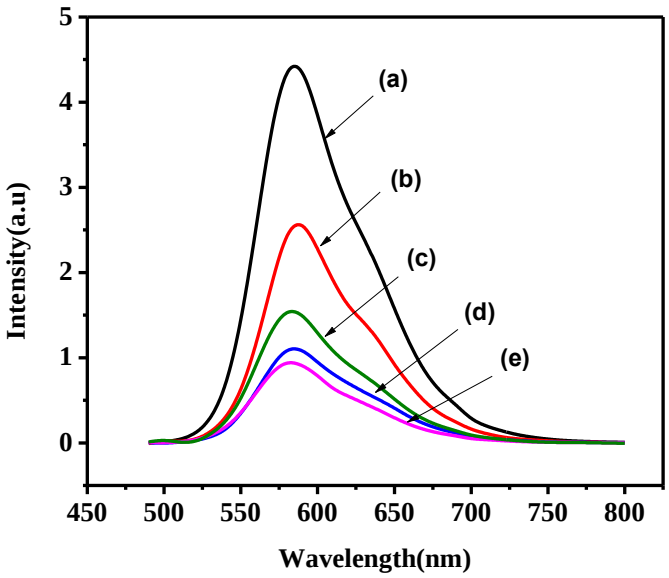

Figure 5.11 (a) PL spectra of P3HT and P3HT-CdPbS nanocomposites synthesized at different ratio of P3HT and CdPbS (a) P3HT (b) P3HT with CdPbS 1:1 (c) P3HT with CdPbS 1:2 (d) P3HT with CdPbS 1:4 (e) P3HT with CdPbS 1:8

Charge transfer take place in conjugated polymer-semiconductor nanocrystals composites at the interface where the P3HT with a higher electron affinity transferred electron onto CdPbS with relatively lower electron affinity. In conversion, the polymer absorb the solar photons (charge generation), the electron is transferred to the CdPbS nanocrystals and the hole potentially can transfer to the polymer (charge separation). This is a well known effect of the ultrafast electron transfer from the donor to acceptor, and it is expected to increase the exciton dissociation efficiency in photovoltaic devices.Reduction in QY of polymer/nanocrystal composites compared to that of pristine P3HT, implying that a large

amount of singlet excitons are not able to radiate onto ground state and they dissociate at the polymer/nanocrystals interface.

5.4(d) Optical Property-Time Resolved Fluoroscence Study

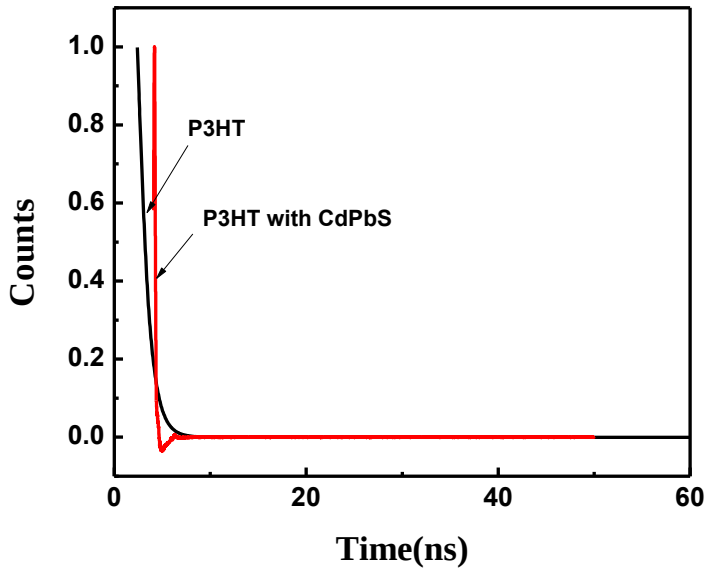

Figure5.12 TRF spectra for P3HT and P3HT with CdPbS

In order to understand electron transfer dynamics, lifetime measurement studies were performed. Fig.5.12 shows the PL decay curve for P3HT and for P3HT–CdPbS nanocomposites. The rate of PL decay times at which the PL intensity decreases to 1/e of its initial value are used to compare the life time of P3HT and P3HT-CdPbS.

The emission intensity recorded at the emission maximum exhibited a monoexponential decay

$$I(t) = A \exp(-t/\Gamma)$$

where I is the normalized emission intensity, A is pre-exponential factor, t is the time after pulsed-laser excitation, and Γ is lifetime. The decays of both samples are fitted with single exponential. Excitation wavelength used during measurements is 480nm.The kinetic parameters of the P3HT and P3HT-CdPbS emission decay analysis are summarized in Table 2. These result shows the life time of P3HT decreased from 0.9 ns to 0.1 ns on addition of CdPbS indicates efficient charge transfer in P3HT-CdPbS nanocomposite. Also there is more decrease in lifetime values in P3HT–CdPbS nanocomposites as we increase the amount of CdPbS .

	Γ(ns)
P3HT	0.92115
P3HTwith CdPbS(120 mg)	0.185

Table 2:TRF data

5.4(e) Structural Property-XRD Study

Fig. 5.13 shows the diffraction patterns of polymer, CdPbS and P3HT: CdPbS nanocomposites. This XRD analysis confirmed the in situ formation of CdPbS nanoparticles. The diffraction peaks at, (200),(300) and (010) can be associated with the P3HT as reported by C. Borreiello et al and S. Masala et al and at 26.87^0, 30.77^0,43 75^0,54.13^0 may be assigned to (111) (200) (220) (311) planes of the CdPbS material, respectively, which are consistent with those in the literature and from the JCPDS card (no. 65-0241) confirms the formation of Hexagonal phase of CdPbS nanoparticle in polymer nanocomposites.

The crystalline peaks of P3HT decreases as we increased the ratio of nanoparticle precursor in polymer nanoparticle composite. The dimension of CdPbS nanoparticle in nanocomposite and CdPbS without composite can be calculated using Scherrer equation[19]

$$d=0.9\lambda/\beta\cos\theta$$

where β is the line width at an angle 2θ, λ is X-ray wave length.

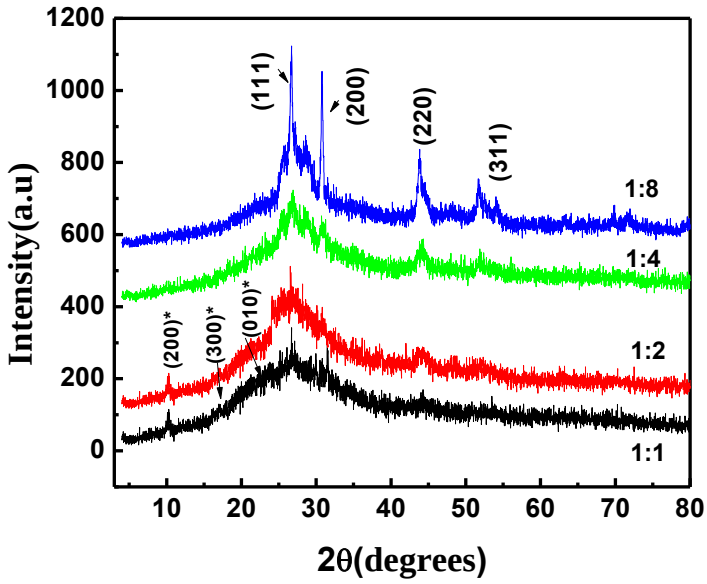

Figure 5.13 XRD spectra of P3HT with different ratios of CdPbS i.e 1:1,1:2,1:4,1:8

Using this formula we can observe the particle size of CdPbS nanoparicle without polymer is 20 nm and for nanocomposites of polymer :CdPbS 1:8 and 1:4 is 18 nm and 9nm respectively shows as we increase the amount of polymer the in polymer nanoparticle composite precursor the particle size is decreases. Here the P3HT can act as a macromolecule template to control the geometrical development of CdPbS nanocrystals.

5.4(f) Structural Property-TEM Study

Transmission electron microscopy (TEM) image and electron diffraction patterns of the synthesized P3HT-CdPbS nanocomposites 1:8 at 120 °C are shown in Fig.5.14 as in Fig.5.14

(a) and Fig.5.14 (b) . A difference in contrast at different places indicates that the CdPbS nanocrystals are capped by P3HT. However, this interaction between polymer and nanoparticles indicates that nanocomposites have potential for the charge transfer at polymer-nanoparticles interfaces,

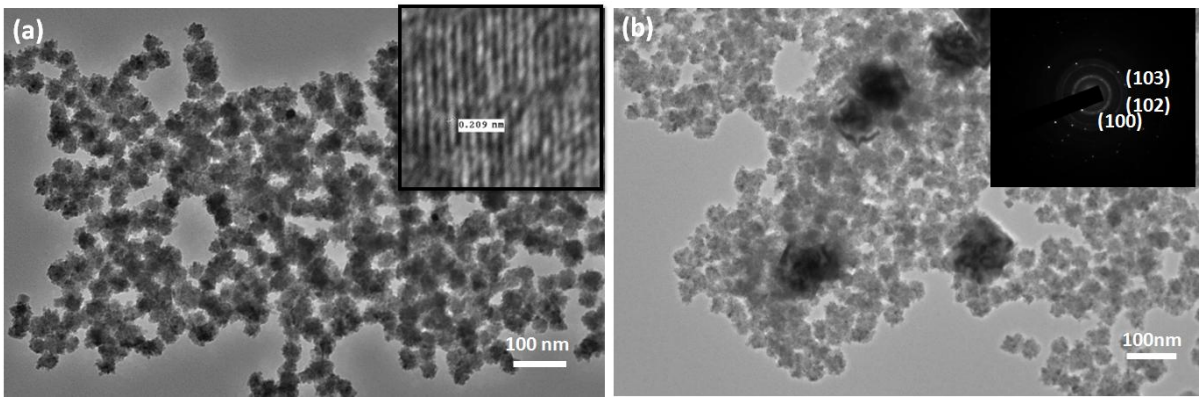

Figure 5.14 (a)TEM images of the synthesized P3HT-CdPbS (1:8) at 120 °C(inset shows HRTEM image) (b)TEM image of P3HT-CdPbS(inset shows SAED Pattern of P3HT-CdPbS).

which results in the PL quenching. The mechanism of this interaction has revealed that the sulphur atom of P3HT can interact with the CdPbS nanoparticles by dipole-dipole interaction and CdPbS nanocrystals have been deposited uniformly and compactly on or in-between the P3HT chains to form nanoparticles. Fig. 5.14(a) ,5.14(b) shows the formation small sized monodispersed circled CdPbS nanoparticles of average size 18nm. Fig.5.14(a) inset shows the high magnification images of corresponding nanoparticles ,the presence of sharper lattice fringes in high-resolution image shows crystallnity of nanoparticles and these results are good agreement with XRD results nanoparticles.The selected area electron diffraction pattern of CdPbS nanocrystal(inset of Fig.6.14(b)) confirms the single crystalline nature of

nanoparticles and the CdPbS nanoparticles with plane (100), (102) and (103) of diffraction rings, corresponding to d spacing 3.68nm, 2.23nm and 1.89nm.

5.5 CONCLUSIONS

In conclusion, the successful synthesis of CdS/CdbS nanoparticles in a P3HT matrix without need of any surfactant has been demonstrated. In summary, reproducible, and simple solution-based process for the fabrication of the CdS/CdPbS absorber layer UV-vis absorption . This synthetic route is robust, low-cost, and environmentally friendly and could be applicable to many semiconductor systems for fabrication of high quality electro-optic devices. In summary, we have shown a simple one-pot procedure for producing highly crystalline, monodisperse CdS/ CdPbS nanocrystals at elevated temperatures in P3HT. SAED showed that the nanocrystals had a rock-salt crystal structure.

5.6 References

1. C. Groves, O. G. Reid, and D. S. Ginger, Acc. Chem. Res. **5**, 612 (2010).

2. S. Dayal, N. Kopidakis, D. C. Olson, D. S. Ginley, and G. Rumbles, Nano Lett. **10**, 239 (2010).

3. W. U. Huynh, J. J. Dittmer, W. C. Libby, G. L. Whiting, and A. P. Alivisatos, Adv. Funct. Mater. **13**, 73 (2003).

4. D. Cui, J. Xu, T. Zhu, G. Paradee, S. Ashok, and M. Gerhold, Appl. Phys. Lett. **88**, 183111 (2006). H. C. Liao, S. Y. Chen, and D. M. Liu, Macromolecules **42**, 6558 (2009).

5. S. Dayal, N. Kopidakis, D. C. Olson, D. S. Ginley, and G. Rumbles, J. Am. Chem. Soc. **131**, 17726 (2009).

6. A. Stavrinadis, R. Beal, J. M. Smith, H. E. Assender, and A. A. R. Watt, Adv. Mater. **20**, 3105 (2008).

7. M. T. Khan, M. Bajpai, A. Kaur, S. K. Dhawan, and S. Chand, Synth. Met. **160**, 1530 (2010).

8. B. K. Kuila and A. K. Nandi, J. Phys. Chem. B **110**, 1621 (2006). R. D. McCullough, Adv. Mater. **2**, 93 (1998).

9. J. Xu, J. Hu, X. Liu, X. Qiu, and Z. Wei, Macromol. Rapid Comm. **30**, 1419 (2009).

10. J. Xu, J. Wang, M. Mitchell, P. Mukherjee, M. Jeffries-EL, J. W. Petrich, and Z. Lin, J. Am. Chem. Soc. **129**, 12828 (2007).

11. Y. Y. Lin, T. H. Chu, S. S. Li, C. H. Chuang, C. H. Chang, W. F. Su, C. P. Chang, M. W. Chu, and C. W. Chen, J. Am. Chem. Soc. **131**, 3644 (2009).

12. H. C. Leventis, S. P. King, A. Sudlow, M. S. Hill, K. C. Molloy, and S. A. Haque, Nano Lett. **10**, 1253 (2010).

13. H. Xin, O. G. Reid, G. Ren, F. S. Kim, D. S. Ginger, and S. A. Jenekhe, ACS Nano, **4**, 1861 (2010).

14. K. M. Coakley and M. D. McGehee, Chem. Mater. **16**, 4533 (2004).

15. B. G. Kim, M. S. Kim, and J. Kim, ACS Nano, **4**, 2160 (2010).

16. S. Zhang, P. W. Cyr, S. A. McDonald, G. Kostantatos, and E. H. Sargent, Appl. Phys. Lett. **87**, 233101 (2005).

17. J. Xu, J. Hu, X. Liu, X. Qiu, and Z. Wei, Macromol. Rapid Comm. **30**, 1419 (2009).

18. H.Y. Chen, M. K. F. Lo, G. Yang, H. G. Monbouquette, and Y. Yang, Nat. Nanotech. **3**, 543 (2008).

19. B. Cullity, Elements of X-ray Diffraction, 2nded. Addison-Wesley, Redding, 1978.

CHAPTER-6

Colloidal Nanocrystals of Kesterite and Wurtzite-Type Cu_2ZnSnS_4: Facile Noninjection Synthesis and Formation Mechanism

6.1 Introduction

To be sustainable, future electronic materials must deliver desirable optoelectronic properties while containing only abundant and benign elements. While silicon can satisfy these requirements, it has well known limitations that necessitate the use of other materials in several important applications. Unfortunately, many of these other materials, such as GaAs or CdTe, have rare and toxic elements. The field of sustainable electronics (or sustronics) aims to develop new electronic materials that avoid these problems.

One example is Cu_2ZnSnS_4(CZTS), which is emerging as a promising new sustainable semiconductor for solar cells.CZTS has a high absorption coefficient ($\sim 10^4 cm^{-1}$) and an electronic bandgap (~1.5 eV)[1]that is nearly ideal for photovoltaics. Indeed, thin-film $Cu_2ZnSn(S,Se)$ solar cells were recently demonstrated with an overall power conversion efficiency of 9.7%[2].

To improve upon this result, one potential strategy would be to develop nanostructured CZTS. For example, semiconductor nanocrystals (or colloidal quantum dots)[3]have been proposed as a general route to high-efficiency, low-cost photovoltaic devices[4,5].These

materials are solution processible and, due to quantum confinement, exhibit optical properties that are tunable with nanocrystal size. In materials where the electronic levels can be changed through composition and quantum confinement, one can independently control both the effective band gap, and the location of the lowest unoccupied electronic level (e.g., electron affinity). Thus, multilayered devices containing films of quantum dots of different sizes could yield inexpensive multijunction solar cells[6].However, the best quantum-dot solar cells to date[7,8] have utilized lead chalcogenide nanocrystals that do not satisfy sustainability goals. CZTS nanocrystals could solve this problem while preserving the advantages of quantum dots.

Recently, several synthetic approaches to CZTS nanocrystals have been reported[9-12]. Herein we resolve the issues by demonstrating a simple synthesis that provides CZTS nanocrystals with diameters ranging in increasing order. This allows us to observe the effect of quantum confinement in the optical absorption spectra.

6.2 Synthesis of of Kesterite Type Cu_2ZnSnS_4 Colloidal Nanocrystals

6.2(a) Introduction

Our nanocrystals were synthesized from copper, zinc, and tin diethyl dithiocarbamate complexes. Because these molecules decompose thermally to produce their corresponding Sulphides [13], CZTS nanocrystals can be obtained when stoichiometric mixtures of these three complexes are heated together. However, since their decomposition temperatures are 220^0C, 240^0C, and 175^0C, respectively, premature decomposition of one can result in unwanted phases such as SnS_2 and Cu_2S .To avoid this, we utilized the addition of oleylamine, which can lower the decomposition temperature of all three complexes to a

narrow temperature range[14].The mechanism of oleylamine promoted thermal decomposition of metal alkyldithiocarbamate complexes was investigated by Jung et al. who hypothesized that oleylamine coordinates with the thiocarbonyl carbon of the dithiocarbamate ligand and accelerates decomposition[14].Thus, simultaneous decomposition of the copper, zinc, and tin dithiocarbamate complexes can be triggered by the sudden injection of oleylamine into a mixture of the three complexes.The amine is added when the mixture temperature is below that needed for the decomposition of the individual complexes, but above that needed for the decomposition of the complexes in the presence of the amine.

This approach leads to nucleation and subsequent growth of CZTS nanocrystals.The concentration of the nuclei available for growth is determined by the amount of oleylamine that is injected. By varying this amount and the growth temperature, we were able to tune the average diameter of the nanocrystals. Specifically, the final nanocrystal size decreased with an increase in added oleylamine and with a decrease in the growth temperature.Attenuated-total-reflection Fourier transform infrared spectra of the nanocrystals showed that the nanocrystals are capped both with oleylamine and oleic acid ligands.

6.3 Synthetic Procedure for Kesterite type Cu_2ZnSnS_4 colloidal nanocrystals.

Precursor's formation

Synthesis of Copper Diethyldithiocarbamate [Cu $(dedc)_2$]:

9.0 g of sodium diethyldithiocarbamate was dissolved in 150 mL of distilled water and added dropwise to a solution of 4.23 g of copper chloride in 50 mL distilled water (85 mg/mL) with

constant stirring. The black precipitate that formed upon reaction was filtered and washed multiple times with ultra-high purity water before drying in a desiccator. $Cu(dedc)_2$ crystals were dried overnight in vacuum before use.

Synthesis of Zinc Diethyldithiocarbamate [Zn $(dedc)_2$)]:

9.0 g of sodium diethyldithiocarbamate was dissolved in 150 mL of distilled water and added dropwise to a solution of 3.38 g of zinc chloride in 50 mL of distilled water (68 mg/mL) with constant stirring. The white precipitate that formed upon reaction was filtered and washed multiple times with ultra-high purity water before drying in a desiccator. $Zn(dedc)_2$ crystals were dried overnight in vacuum before use.

Synthesis of Tin Diethyldithiocarbamate [Sn $(dedc)_4$]:

12.85 g of sodium diethyldithiocarbamate was dissolved in 200 mL of distilled water and added dropwise to a solution of 2.5 g of tin tetrachloride in 50 mL of distilled water (50 mg/mL) with constant stirring. The orange precipitate that formed upon reaction was filtered and washed multiple times with ultra-high purity water before drying in a desiccator. Orange crystalline powder of $Sn(dedc)_4$ crystals were dried overnight in vacuum before use.

Synthesis of CZTS Nanocrystals:

The CZTS nanocrystals were synthesized under dry nitrogen gas using a Schlenk line. In a typical synthesis, 18 mL of octadecene and 2 mL of oleic acid were mixed in a 100 mL three-neck flask. 27 mg of Cu $(dedc)_2$, 13.6 nm of $Zn(dedc)_2$, and 26.7 mg of $Sn(dedc)_4$ were then added to this mixture and the flask was connected to the Schlenk line and degassed multiple times at 60 °C. The crystals dissolved on stirring to give a brown solution. The contents of

the flask were heated to the synthesis temperature and a specific volume of oleylamine was injected into the mixture. The nanocrystal size was tuned by changing the temperature and the amount of oleylamine that was injected. For example, to carry out synthesis of first sample, 3 mL of oleylamine was injected into the flask at 150 °C to initiate nucleation. The nanocrystals were then allowed to grow for 4 minutes before quenching the reaction by immersing the flask in water. For the synthesis second sample nanocrystals, a mixture of 1.5 mL of oleylamine and 1.5 mL of octadecene were injected into the flask at 150 °C. For the synthesis of third and fourth sample CZTS nanocrystals, the injection was performed at 175 °C. To avoid premature decomposition of Sn $(dedc)_4$ at this temperature, $Sn(dedc)_4$ was not dissolved and heated in the reaction flask with the other complexes. Rather, Sn $(dedc)_4$ was dissolved in oleylamine and octadecene and injected into the flask. All other steps of the synthesis and purification steps remained the same. Specifically, for third synthesis nanocrystals, $Sn(dedc)_4$ was dissolved in a mixture of 1.5 mL of oleylamine and 1.5 mL of octadecene and injected into the flask at 175 °C. For fourth sample nanocrystals, Sn $(dedc)_4$ was dissolved in a mixture of 0.75 mL of oleylamine and 2.25 mL of octadecene and injected into the flask at 175 °C.Two more samples were prepared same as above conditions instead synthesis temperature was changed to 175^0C and 200^0C stabilized for 30 minutes.

The nanocrystals were precipitated from the dispersion using reagent alcohol and were centrifuged for 5 minutes at 4000 rpm. The supernatant was discarded and the nanocrystals were redispersed in toluene. The precipitation and dispersion steps were repeated multiple times to remove excess oleylamine and oleic acid. Finally, the nanocrystals were dispersed in toluene and stored for later use.

6.4Results and discussions

6.4(a) TGA/DTA Study

Thermal decomposition of precursor was studied by Thermo gravimetric Analysis (TGA) and Differential Scanning Calorimetry (DSC) of samples. Thermo gravimetric analysis of Copper,Zinc and Tin Diethyldithiocarbamate respectively was carried out from room temperature to 300^0C. The TGA curves in Fig.6.1(a),Fig. 6.1(b) and Fig. 6.1(c) shows that significant weight losses (WL) takes place in temperature region starting at 200^0C until 300^0C and is because of thermal decomposn of diethyldithiocarbamate complex but as evident from figures decomposition is not complete even at 300^0C. The end products are copper,zinc and tin sulphides respectively along with volatile compounds. Since the decomposition occurs around 200°C , the synthesis was carried out near to this temperature only.

The DSC plot in Fig. 6.1(a),Fig. 6.1(b) and Fig. 6.1(c) reveals several peak and dips. The sharp dips at temperatures 216^0C in Fig. 6.1(a)190^0C,80^0C ,238^0C in Fig. 6.1(b) and 84^0C,166^0C,229^0C,279^0C in Fig. 6.1(c) represents that the reaction is endothermic and peaks at temperature 270^0C in Fig. 6.1(b) represents that the reaction is exothermic The enthalpy changes associated with the events occurring are given by the area under the sharp dips. In general, the heat capacity will also change over the region.

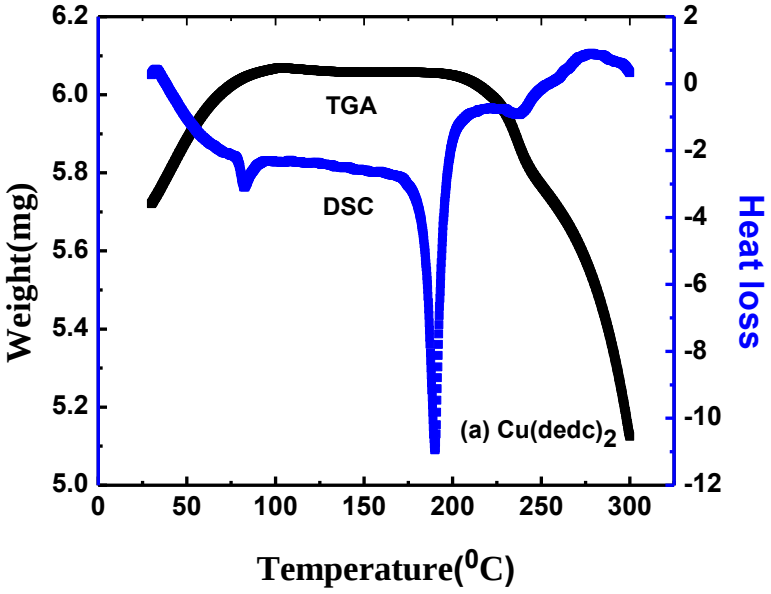
TGA
DSC
(a) Cu(dedc)2
Weight(mg)
Heat loss
Temperature(0C)

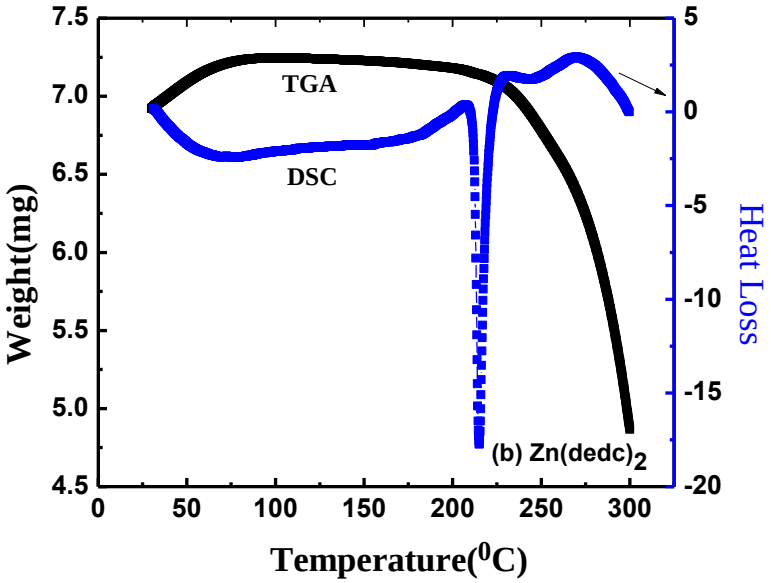
TGA
DSC
(b) Zn(dedc)2
Weight(mg)
Heat Loss
Temperature(0C)

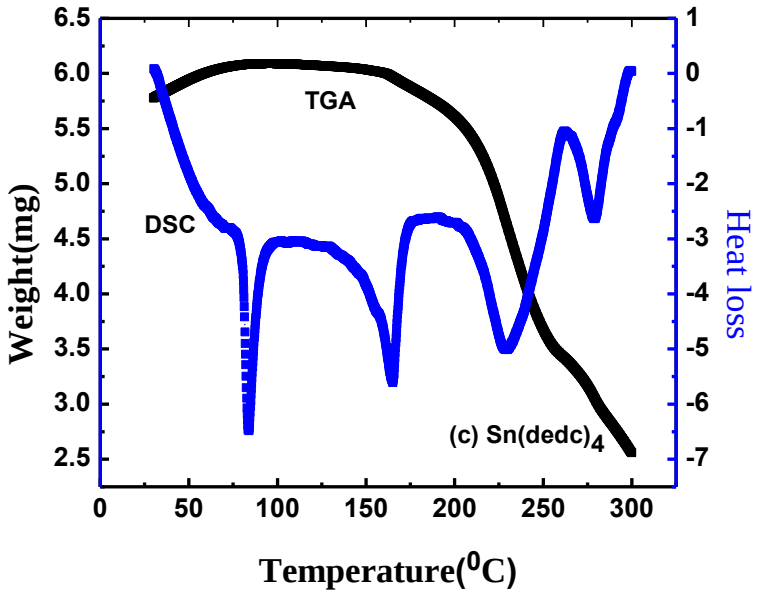

Figure6.1 Thermogravimetric Analysis and Differential Scanning Calorimetry of (a) Copper Diethyldithiocarbamate (b) Zinc Diethyldithiocarbamate (c) Tin Diethyldithiocarbamate

6.4(b) Spectral study-FTIR

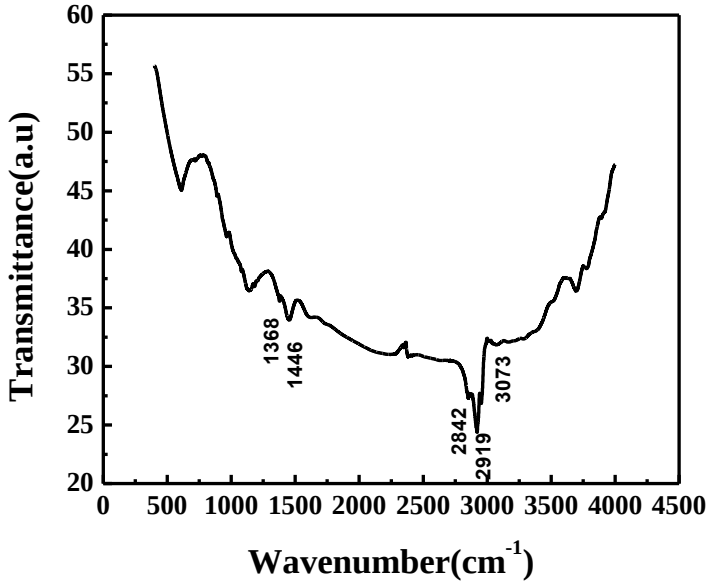

Figure 6.2 FTIR Spectra for CZTS

The success of formation of CZTS nanoparticles have been confirmed by the Fourier transform infra-red (FT-IR) spectra as shown in Fig.6.2.In case of CZTS nanoparticles band appearing around 3073 cm^{-1} indicates the presence of amine group. Peak clearly seen at 2919cm^{-1} in CZTS are due to -C=CH- stretching.

Peak observed at 2842 cm^{-1} is due to C-H stretch. The carbonyl group from carboxyl salt is present which is confirmed by $–COO^-$ symmetric stretch present at approx. 1446cm^{-1} and $–COO^-$ asymmetric stretch present at approx. 1368cm^{-1} . The FTIR data suggests that both oleylamine and oleic acid act as capping ligands for the nanocrystals.

6.4(c) Optical property – UV Absorption study

Fig.6.3 exemplifies the absorption spectra of CZTS films as a function of size synthesized at different conditions as described in experimental part above. It can be seen from the spectra that there exist a strong blue shift which shows absorption onset. The band gap energy, Eg, was calculated using the Tauc's relation, $(\alpha h\upsilon)^{1/n} = A(h\upsilon - E_g)$, where A is a constant and n is equal to 1/2 for direct allowed transitions. The estimation of band gap from the plot of $(\alpha h\upsilon)^2$ verses $(h\upsilon)$ is shown in Fig.6.4. Band gap values are obtained by extrapolating the linear part of the absorption curves to intercept the energy axis ($\alpha h\upsilon=0$). Different conditions are represented in the taucs plot that shows a significant shift of band gap.Fig.6.4(a) and (b) are prepared at 150^0C for different amount of oleylamine added stabilized for 4 minutes.Fig.6.4(c) and (d) are prepared at 175^0C for different amount of oleylamine added stabilized for 4 minutes.Fig.6.4(e) is prepared at 150^0C stabilized for 30 minutes.Fig. 6.4(f) is prepared at 175^0C stabilized for 30 minutes.In this case, the estimated Eg values are found to

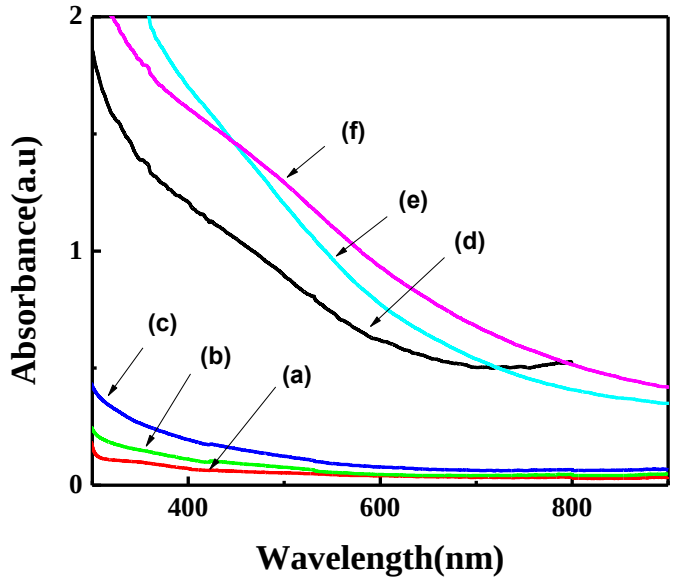

Figure6.3 Absorption spectra of CZTS prepared at different conditions

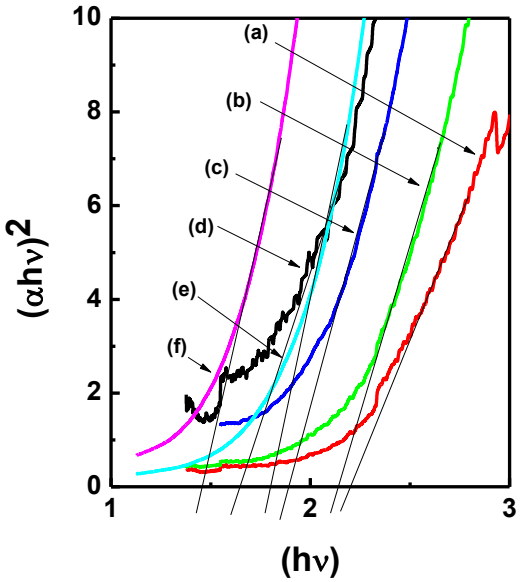

Figure 6.4 Estimation of band gap from Tauc's Plot.

vary between 1.45eV (bulk) to 2.2eV for the samples prepared at different conditions. This clearly indicates a considerable decrease in the band gap. Thus, the observed large modification in the band gap confirms the formation of quaternery CZTS alloy and the existence of strong quantum confinement in this system

In general, the optical transitions of a bulk semiconductor should shift to higher energy if the optically excited electron hole pair is confined within the nanocrystal boundary[15-16]. The edge of the optical absorption spectrum as well as the lowest energy absorption peak shift to higher energy as the diameter decreases .There was no photoluminescence from the nanocrystals.

6.4(d) Optical property – PL study

Fig.6.5 (a), (b) shows the emission intensity profiles of P3HT: CZTS composite in chloroform as a function of volume of CZTS prepared at two different conditions. As evident in Fig. 6.5 (b) a more systematic decrease in emission intensity of P3HT: CZTS composite is observed with increase in the CZTS concentration as compared to Fig. 6.5 (a). This shows that there is more efficient electron transfer occurring, leading to the formation of separated electron-hole pairs that subsequently recombine non-radiatively. It is important to note here that the quenching of the polymer luminescence, while significant, is not complete even at high nanocrystal concentrations. This could be due to the occurrence of phase segregation in the composite material.

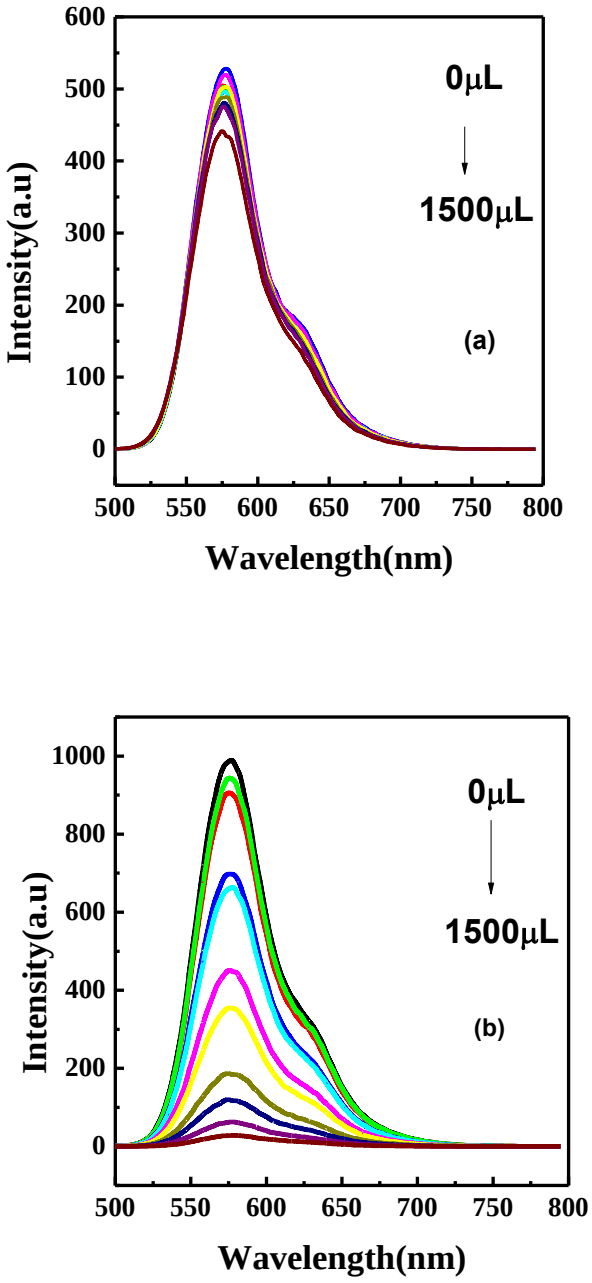

Figure6.5 Emission intensity profiles of P3HT-nanoparticle composite in chloroform in the presence of different concentrations CZTS prepared at two different conditions.

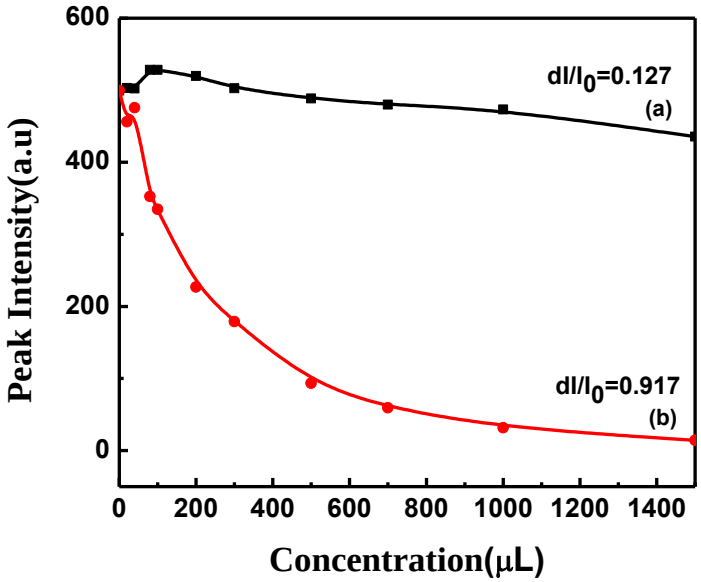

Figure 6.6 Emission intensity profile as a function of concentration of CZTS for P3HT: CZTS composite prepared at different conditions

If the CZTS nanocrystals were randomly dispersed in the polymer matrix, absolute complete quenching could have been expected. The emission intensity profile of P3HT : CZTS composite as a function concentration of CZTS (Fig. 6.6) prepared at two different conditions shows the rates of PL decay for P3HT : CZTS is 0.127 for first preparatory condition P3HT:CZTS is 0.917 for second preparatory condition respectively confirms the efficient electron transfer in P3HT:CZTS composite.

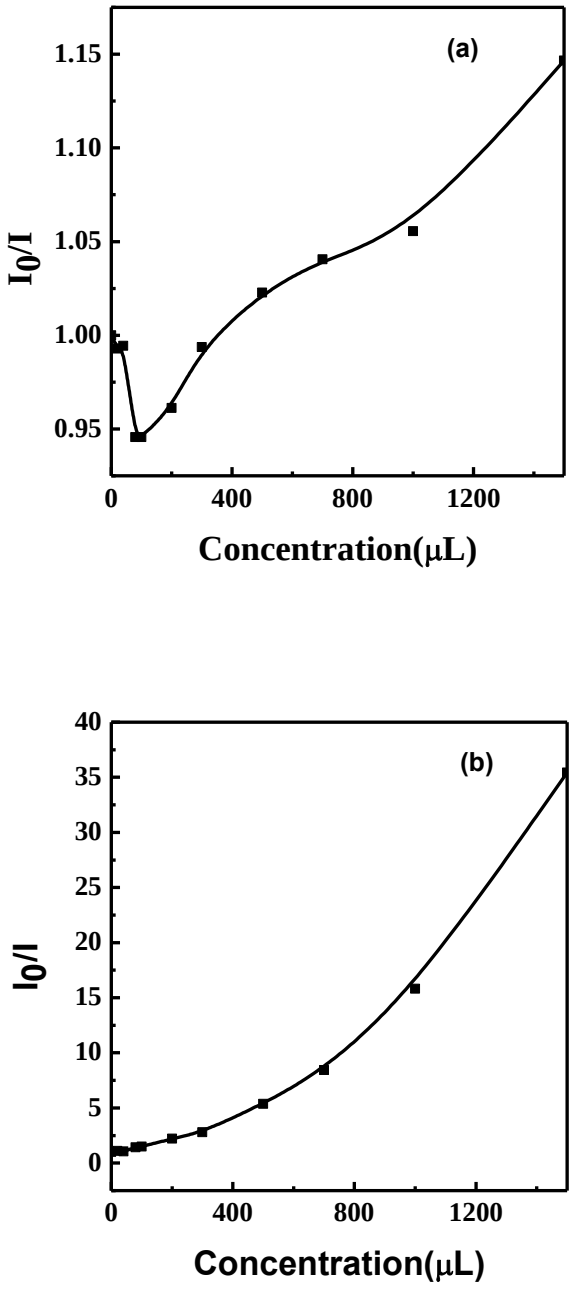

Figure 6.7 Stern Volmer plots of P3HT: CZTS nanocomposite prepared at different conditions

A plot known as a Stern–Volmer plot is shown in Fig.6.7(a-b) for P3HT:CZTS nanocomposites prepared at two different conditions. However, as evident in Fig.6.7 (a-b), nonlinear Stern–Volmer plots with negative deviation from linearity are obtained. Such nonlinear Stern–Volmer plots can occur in the case of heterogeneous quenching (collisional

or static) if some of the fluorophores are less accessible than others[17-18]. The Stern–Volmer quenching constant for P3HT:CZTS is0.1504 X $10^3 M^{-1}$ for first preparartory condition and 10.9 X 10^3 M^{-1} for second preparatory condition respectively. Here, it is evident that P3HT:CZTS nanocomposites, show higher values of quenching constants (i.e. high rate of quenching) for second preparatory condition and thus efficient charge transfer as compared to first preparatory condition resulting in efficient charge transfer across P3HT:CZTS nanocomposites.

6.4(e) Optical properties – Time Resolved Fluoroscence study

In order to understand electron transfer dynamics, lifetime measurement studies were performed. Fig.6.8 shows the PL decay curve for P3HT and for P3HT–CZTS nanocomposites.

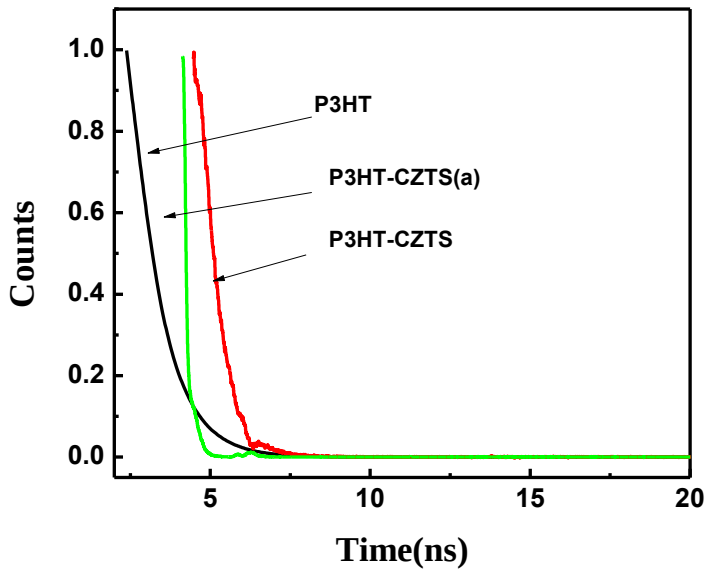

Figure 6.8 TRF Spectra for P3HT and P3HT-CZTS (at different conditions)

The rate of PL decay times at which the PL intensity decreases to 1/e of its initial value are used to compare the life time of P3HT and P3HT-CZTS.

The emission intensity recorded at the emission maximum exhibited monoexponential decay

$$I(t) = A \exp(-t/\Gamma)$$

where I is the normalized emission intensity, A is pre-exponential factor, t is the time after pulsed-laser excitation, and Γ is lifetime. The decays of both samples are fitted with single exponential. Excitation wavelength used during measurements is 480nm.The kinetic parameters of the P3HT and P3HT-CZTS emission decay analysis are summarized in Table. These result shows the life time of P3HT decreased from 0.9 ns to 0.135 ns on addition of CZTS indicates efficient charge transfer in P3HT-CZTS nanocomposite. Also there is more decrease in lifetime values in P3HT–CZTS nanocomposites as perform the synthesis at two different temperatures i.e.150^0C and 175^0C .

	Γ(ns)
P3HT	0.92115
P3HTwith CZTS(150^0C)	0.748
P3HTwith CZTS(175^0C)	0.13485

6.4(f) Structural properties-XRD study

The wide-angle powder X-ray diffraction pattern of the nanocrystallites is shown in Fig 6.9 above.The XRD peaks are broadened compared to those of the bulk CZTS which is an indication that the particles are in the nanosize regime.

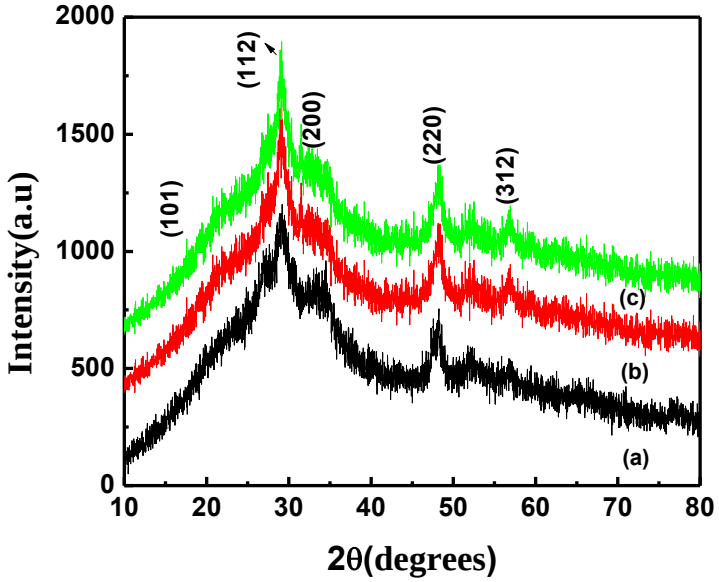

Figure 6.9 XRD diffraction pattern of CZTS prepared at different conditions

In Fig.6.9 (a) is prepared at 150^0C with 1.5ml amount of oleylamine,(b) is prepared at 175^0C with 1.5ml amount of oleylamine and (c) is prepared at 175^0C with 0.75ml amount of oleylamine all together stabilized for 4 minutes. However, the(112), (220), and (303) planes of kesterite CZTS are clearly distinguishable in the diffraction pattern,other peaks are observed at(101)and(200) which are consistent from JCPDS card(no.26-0575).The mean crystallite diameter,d, can be calculated by the Scherrer formula[19],

$$d=0.9\lambda/\beta\text{Cos}\theta$$

where λ is the X-ray wavelength,and β is the full width at half maximum of the diffraction peak on the 2θ scale.The size of the crystallites was determined using the (112) reflection at 28.91^0 (2θ) and the calculated value is found to be 5nm for (a),8nm for (b) and10nm for (c) for Fig6.8.

6.4(g) Structural property-SEM-EDS Study

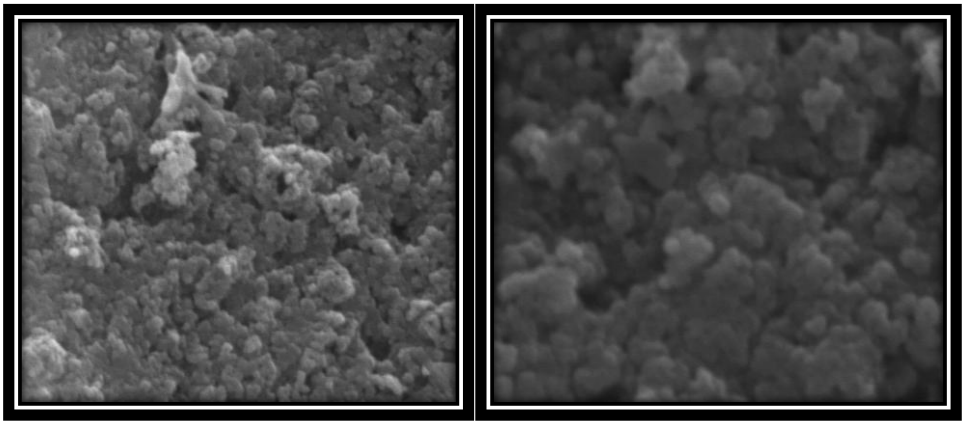

Figure 6.10 SEM images of CZTS

In order to understand the morphology of as synthesized CZTS nanoparticles scanning electron microscopy (SEM) was preformed. Fig.6.10 gives the typical morphologies of the CZTS films prepared at 175^0C shows the presence of large micrometersized agglomerates on the film surface, show CZTS nanoparticles uniformly distributed over the film surface

To further investigate the composition of the CZTS, the energy dispersive X-ray spectroscope (EDS) spectrum (Fig.6.11) was obtained. EDS analysis of the CZTS demonstrates that the chemical component consists of Cu, Zn, Sn and S. and Table shows approximate relative ratio of Cd: Zn:Sn:S ≈2:1:1:4. This ratio agrees with the nominal CZTS statiometry

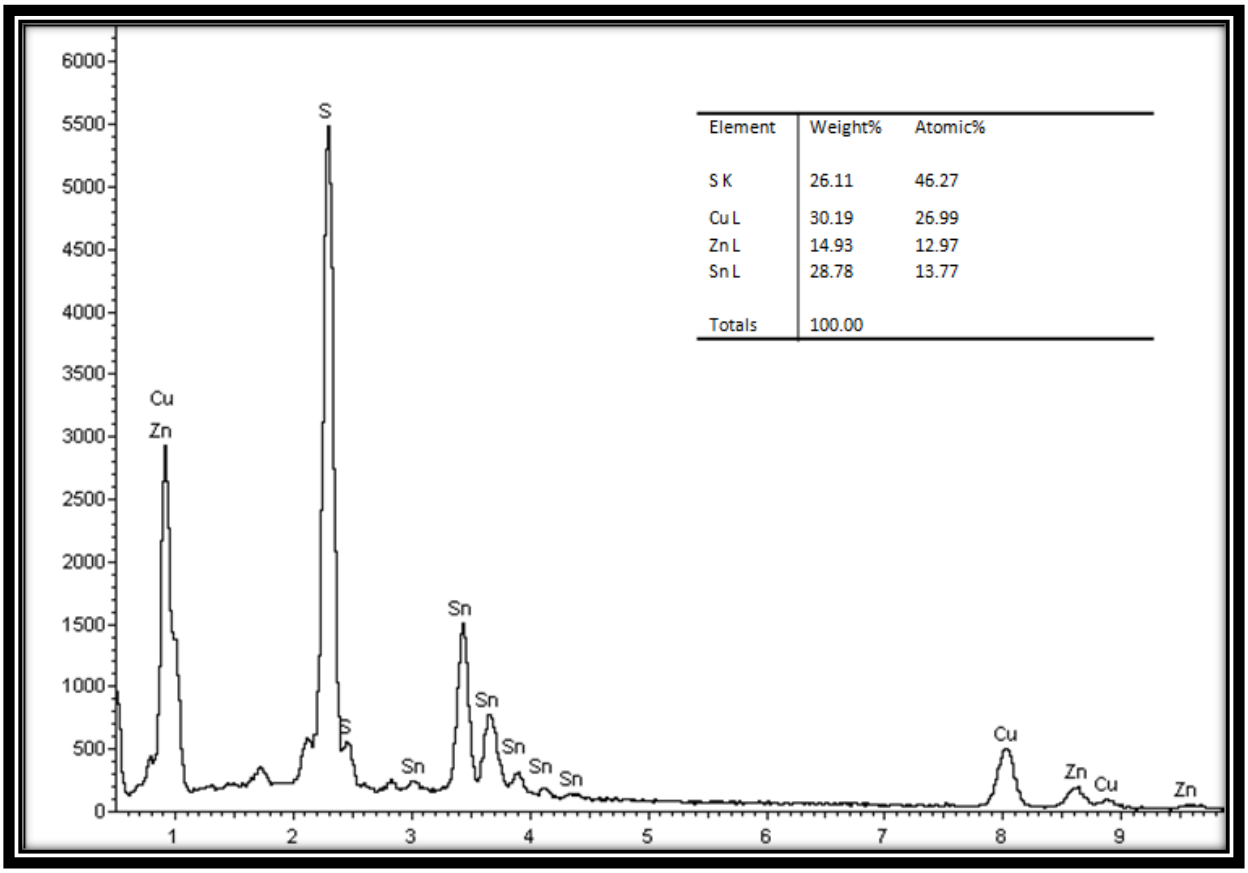

Figure 6.11 EDS pattern for CZTS

6.4(h) Structural property-TEM Study

Transmission electron microscopy (TEM) image and electron diffraction patterns of the synthesized CZTS nanoparticles at 175 °C are shown in Fig.6.12. Fig 6.12(a) shows the formation small sized monodispersed circled CZTS nanoparticles of average size 10 nm. Fig6.12(b) shows the high magnification images of corresponding nanoparticles ,the presence of sharper lattice fringes in high-resolution image shows crystallnity of nanoparticles and these results are good agreement with XRD results nanoparticles. The selected area electron diffraction pattern (SAED) of CZTS nanocrystal in Fig 6.12 (c) confirms the single crystalline nature of nanoparticles and the CZTS nanoparticles with plane (112), (220) and (312) of diffraction rings, corresponding to d spacing 3.18nm, 1.95nm and 1.69nm.

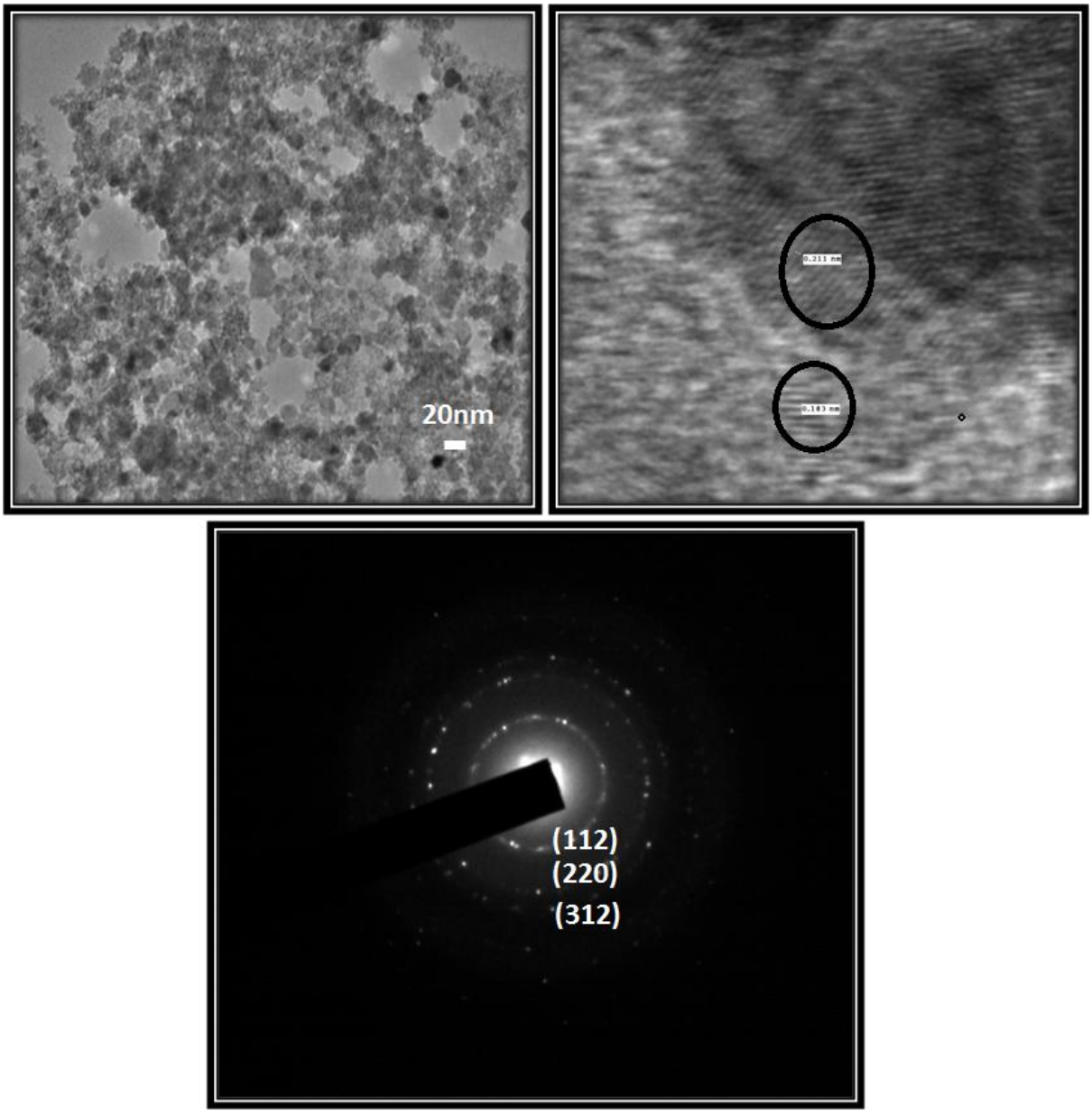

Figure 6.12 (a)TEM image of kesterite type CZTS (b)HRTEM image of kesterite type CZTS (c)SAED pattern of CZTS

6.5 Conclusion

In summary, we report a synthesis of CZTS nanocrystals where the average nanocrystal diameter could be changed controllably. Characterization using HRTEM, XRD, and SEM confirm the phase purity of the CZTS nanocrystals. Our smallest nanocrystals exhibit shifts in their optical transitions which are consistent with quantum confinement.

6.6 Formation of Wurtzite type CZTS nanocrystals-Introduction

With the increasingly serious energy crisis, research on high efficient but low cost solar cells becomes more important.Among numerous types of solar cells, the $CuIn_xGa_{1-x}S(Se)_2$(CIGS) thin-film solar cell has attracted great interest due to its high power conversion efficiency and fine stability[20-21].However, the low availability of indium and/or gallium increases the production costs and hinders the development of CIGS thin-film solar cells[22-23].For years, scientists have been trying to find a substitute for CIGS that avoids using costly elements. Cu_2ZnSnS_4(CZTS), which is a structural analogue to CIGS, has drawn much attention because of its earth-abundant composition[24-26].As a direct-gap semiconductor with a high absorption coefficient, CZTS is suitable in the application of thin-film solar cells. The reported photoelectric conversion efficiency of the CZTS-based solar cell has reached as high as 6.7%,[27]which promotes the research on CZTS. On the other hand, the wet chemical approach to fabricate semiconductor films in solar cells using nanocrystal dispersion was put forward.[26,28,29]This technique enables cheaper fabrication of photovoltaic films than the traditional physical methods, benefiting from the progress in synthesizing high quality semiconductor nanocrystals. Therefore, producing CZTS thin-film solar cells by a nano-

chemical route may illuminate the way of reducing the high cost of solar energy. In the last two years, the CZTS nanocrystals have attractedintensive investigation.[29-31]Herein, we report new wurtzite phase CZTS nanocrystals synthesized with the assistance of dodecanethiol.The traditionally obtained CZTS is always in the kesterite or stannite phase, which features a tetragonal crystal cell.[31-35]But wurtzite phase CZTS, different from the traditional ones,has a hexagonal crystal cell. In this structure, the sulfur anionsare hexagonally close packed to form the frame of the cell structure and then the cations occupy a half of the tetrahedral interstices of the sulfur frame. The band gap of the new wurtzite phase CZTS was measured as 1.4 eV. As a benefit from the ligands used in the synthesis, the shape of the as-obtained wurtzite CZTS nanocrystals can be well controlled. These nanocrystals can also be well dispersed in non-polar solvent and simply fabricated into the CZTS film by the direct liquid coating method. [28]The film has a photoelectric response. Our report shows that this new wurtzite CZTS has potential in the application of photovoltaic devices.

Herein, we provide a facile noninjection synthetic route for preparing monodisperse anisotropic CZTS nanocrystals that adopt a WZ-type crystal structure. The noninjection or“heating up” approach to colloidal nanocrystals is better in terms of synthetic reproducibility, more convenient for manipulation, and more suitable for large-scale production as compared to the hot-injection method.

6.7 Synthetic Procedure for Wurtzite type Cu_2ZnSnS_4 colloidal nanocrystals

In a typical synthesis, $[Cu(dedtc)_2]$ (36.0 mg, 0.1 mmol), $[Zn(dedtc)_2]$ (18.1 mg, 0.05 mmol), $[Sn(dedtc)_4]$ (35.6 mg, 0.05 mmol), dodecanethiol(5 mL) and trioctylamine(5 mL) were placed in a 50 mL three-neck flask and the reaction mixture was degassed at 100^0C for 20–30 min. The clear yellow solution that formed was then heated under Ar to 250^0C with vigorous stirring. A change in color from yellow to topaz to dark brown was observed at around 220–240^0C. The resulting mixture was kept stirring at 250^0C under Ar for 30 min before placing in a H_2O bath, allowing the mixture to cool to 40^0C. Ethanol was added to precipitate the nanocrystals, and this was followed by centrifugation. The solid obtained was washed thoroughly with methanol.

6.8 Results and Discussions

6.8(a) Optical Property-UV absorption study

We have determined the band gap of our nanometer sized WZ-type CZTS nanocrystals from the absorption spectrum shown in Fig.6.13 .From the plot of the square of $\alpha h\upsilon$ (in which α=absorption coefficient; $h\upsilon$=photon energy) versus the photon energy(Fig. 6.14) , Eg is estimated to be 1.6 eV. The observed value is only slightly larger than the band gap reported in the literature for CZTS nanocrystals with the ZB-derived tetragonal structure (i.e.,Eg=1.5 eV)

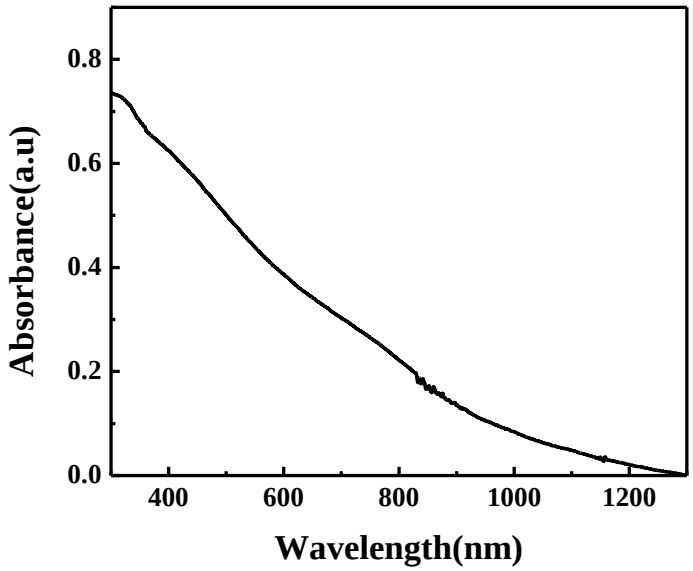

Figure 6.13 UV plot of Wurtzite type Cu_2ZnSnS_4 colloidal nanocrystals

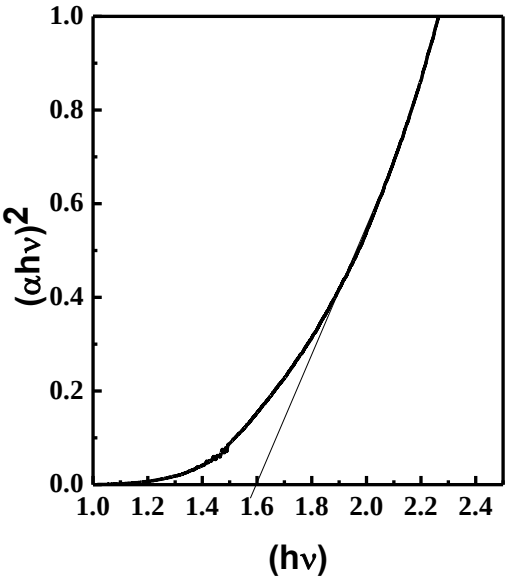

Figure 6.14 Taucs plot of Wurtzite type Cu_2ZnSnS_4 colloidal nanocrystals

This value falls within the optimum band gap range for solar energy conversion in a single-junction device. The photovoltaic properties of this WZ-related CZTS phase will be the subject of further research.

6.8(b) Structural Property-XRD study

Fig. 6.15 shows the XRD patterns of the as-synthesized CZTS nanocrystals. It is noticed that the XRD patterns do not match accurately with the standard pattern of kesterite CZTS (JCPDS 26-0575). Instead, the experimental XRD patterns can be indexed to a new wurtzite phase CZTS. While the crystal cell of kesterite CZTS is an analogue to vertically expanded binary zinc-blende ZnS, wurtzite CZTS could be considered as the derivative of wurtzite ZnS.

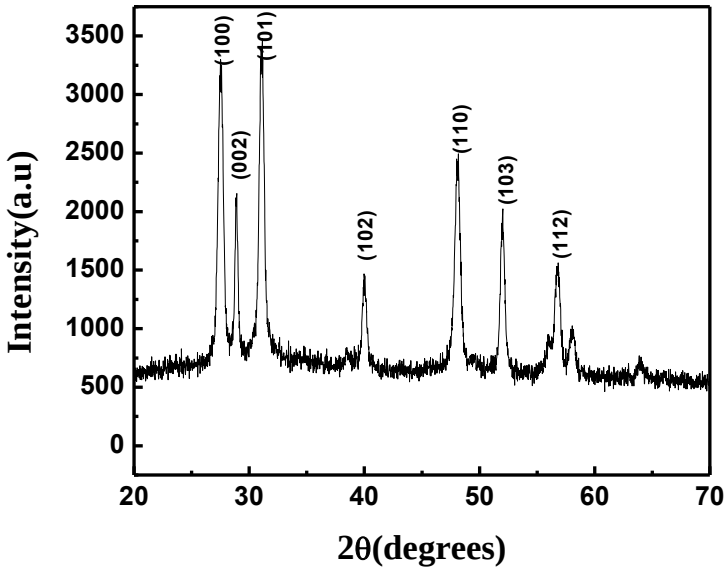

Figure 6.15 XRD Spectra of Wurtzite type Cu_2ZnSnS_4 colloidal nanocrystals

Therefore, the wurtzite CZTS crystal cell was constructed based on the wurtzite ZnS cell .In this structure, sulfur anions are hexagonally close packed; Cu(I),Zn(II) and Sn(IV) cations randomly occupy a half of the interstices of the sulfur anions. The experimental patterns of kesterite and wuetzite kinds of nanocrystals match well with the simulated pattern, indicating

these nanocrystals have a wurtzite structure. The mean crystallite diameter,d, can be calculated by the Scherrer formula[19],

$$d=0.9\lambda/\beta\text{Cos}\theta$$

where λ is the X-ray wavelength,and β is the full width at half maximum of the diffraction peak on the 2θ scale.The size of the crystallites was determined using the (110) reflection at 24.04^0 (2θ) and the calculated value is found to be 17nm for Fig.6.15.

The key factor deciding the formation of wurtzite CZTS rather than kesterite CZTS is considered to be the dodecanethiol used in the reaction. Dodecanethiol could react with the metal cations to produce metal thiolates, which would decompose into corresponding sulphides at certain temperature.[37-39]These thiolates help to balance the different reactivities of cations in solution. Due to the strong coordination with the metal cations exposing on the surface of nanocrystal, dodecanethiol also assists to passivate the obtained wurtzite CZTS. It is rational to speculate that dodecanethiol adjusts the chemical environment preferring the formation of hexagonal structures, which also occurred in the synthesis of wurtzite $CuInS_2$[36].

In colloidal nanocrystal synthesis, the presence of organic surfactants or capping ligands is known to strongly influence the crystallographic phase, morphology, and growth of the nanocrystals.Thus,the formation of metastable phases can be induced with proper selection of surfactants.Our study shows that the presence of long-chain alkanethiols such as hexadecanethiol (HDT) and dodecanethiol (DDT) is pivotal in producing WZ-type CZTS nanocrystals .By contrast, oleylamine (OM) is found to be effective in promoting the formation of the ZB-derived CZTS structure . While trioctylamine (TOA) does not influence

the crystallographic phase, its use in combination with alkanethiols results in nanocrystals that are well-separated and highly monodisperse.

6.8(c) Structural Property-TEM study

In order to gain insights into the formation mechanism of our WZ-type CZTS nanocrystals, the growth process in the presence of DDT was monitored at 250^0C. The TEM images in Fig. 6.16 and XRD patterns reveal that at a reaction time of 30 min,only WZ-type CZTS

nanocrystals that are elongated in shape are observed indicating that the $Cu_{1.94}S$ portion has been converted to WZ-type CZTS. It is worth noting that when $[Cu(dedtc)_2]$ is solely decomposed in the presence of DDT, $Cu_{1.94}S$ is obtained exclusively as the thermolysis product.The above-mentioned observations indicate that the growth process begins with nucleation of $Cu_{1.94}S$ nanocrystals. This is immediately followed by nucleation and anisotropic growth of WZ-type CZTS onto one side of the $Cu_{1.94}S$ nanocrystals, resulting in $Cu_{1.94}S$ –CZTS heterostructured nanocrystals. As the reaction progresses, interdiffusion of the cations between the two components occurs, which eventually leads to purely WZ-type CZTS nanocrystals.

As the binary copper sulfide that initially forms serves as the starting point for the nucleation and growth of CZTS,the crystal structure of the generated CZTS is dictated by the structure of the copper sulfide seed. Binary copper sulfides (Cu_xS, x=1–2) exist in a variety of phases, which can be influenced by the organic surfactant used in the synthesis.In our synthesis using DDT, the Cu_xS that forms is monoclinic $Cu_{1.94}S$ (djurleite), the anion sublattice of which can be described as a hexagonal close packing (hcp) array of sulfur ions.

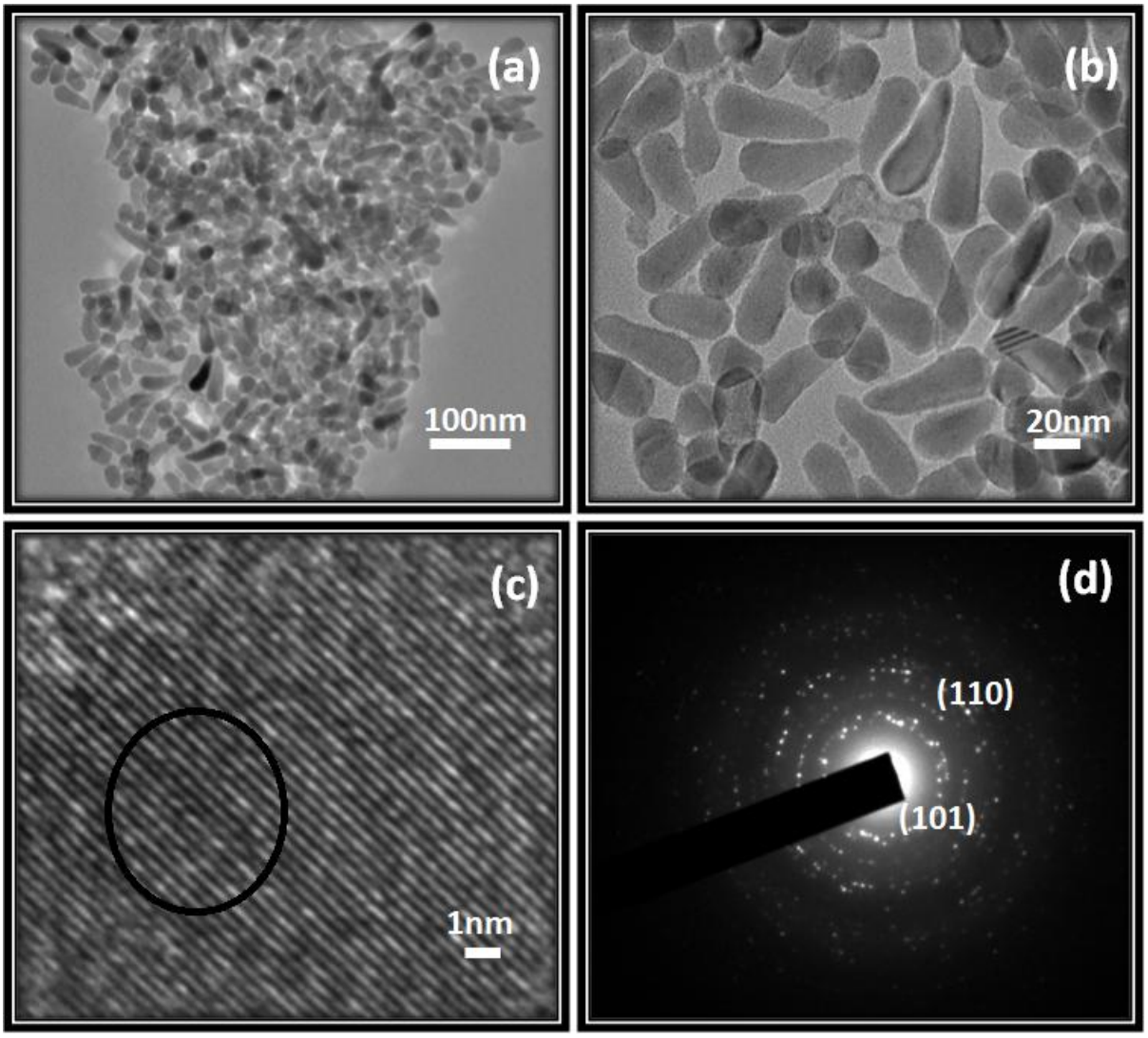

Figure 6.16 (a),(b) TEM images of Wurtzite type Cu_2ZnSnS_4 colloidal nanocrystals (c) HRTEM images of Wurtzite type CZTS (d) SAED pattern of wurtzite type CZTS.

As a result, the CZTS that nucleates and grows onto the initial $Cu_{1.94}S$ exhibits the WZ-related crystal structure, in which the sulfur anions are also in a hexagonal close-packed arrangement. With the similar anionic framework of $Cu_{1.94}S$ and WZ-type CZTS, the interdiffusion of cations between the two materials becomes possible as there is little lattice distortion, resulting in the eventual conversion of the $Cu_{1.94}S$ segment to WZ-type CZTS. The cationic vacancies and the high mobility of Cu ions in nonstoichiometric $Cu_{1.94}S$ are also believed to facilitate the conversion.

Transmission electron microscopy (TEM) image and electron diffraction patterns of the synthesized CZTS nanoparticles at 250 °C are shown.Fig. 6.16(a-b) shows the formation of elongated nanocrystals with one end (base) being much wider than the other (tip). The nanocrystals are nearly monodisperse. The high-resolution TEM images displayed in Fig.6.16(c) reveal continuous lattice fringes, which is indicative of the single-crystalline nature of the nanocrystals. The selected area electron diffraction pattern (SAED) of CZTS nanocrystal in Fig. 6.16(d) confirms the single crystalline nature of nanoparticles and the CZTS nanoparticles with plane (101) and (110) of diffraction rings, corresponding to d spacing 3.3nm and 1.9nm.

6.9 Conclusion

In summary, nanocrystalline CZTS has been colloidally synthesized through a facile noninjection route, which involves the surfactant-assisted thermolysis of metal dithiocar-bamates. The organic surfactant used in the synthesis is found to influence thecrystallographic phase of the CZTS nanocrystals. XRD measurements show that the CZTS nanocrystals prepared in the presence of alkanethiols adopt the recently reported WZ-related crystal structure. By contrast, the presence of oleylamine favors the formation of the more widely studied ZB-derived CZTS phase. Our investigation on the formation mechanism of the WZ-type CZTS nanocrystals reveals that the growth process involves the initial formation of $Cu_{1.94}S$ nanocrystals, which serve as the starting point for the nucleation and growth of WZ-type CZTS. From optical absorption data, the band gap of the WZ-type CZTS nanocrystals is estimated to be 1.6 eV,which is optimal for solar cell applications.

6.11 References

1. H. Katagiri, K. Jimbo, S. Yamada, T. Kamimura, W. S. Maw,T. Fukano, T. Ito and T. Motohiro, Appl. Phys. Express, 2008,1, 041201.
2. T. K. Todorov, K. B. Reuter and D. B. Mitzi, Adv. Mater., 2010,22, E156.
3. Nanocrystal Quantum Dots, ed. V. I. Klimov, CRC Press,Boca Raton, 2nd edn, 2010.
4. W. U. Huynh, J. J. Dittmer and A. P. Alivisatos, Science, 2002,295, 2425.
5. Kongkanand, K. Tvrdy, K. Takechi, M. Kuno and P. V. Kamat,J. Am. Chem Soc., 2008, 130, 4007.
6. T. Franzl, T. A. Klar, S. Schietinger, A. L. Rogach andJ. Feldmann, Nano Lett., 2004, 4, 1599.
7. R.Debnath, J.Tang, D. A.Barkhouse, X.H. Wang,A. G. Pattantyus-Abraham, L. Brzozowski, L. Levina andE. H. Sargent, J. Am. Chem. Soc., 2010, 132, 5952.
8. J. M. Luther, J. B. Gao, M. T. Lloyd, O. E. Semonin, M. C. Beardand A. J. Nozik, Adv. Mater., 2010, 22, 3704.
9. Q. Guo, H. W. Hillhouse and R. J. Agrawal, J. Am. Chem. Soc.,2009, 131, 11672.
10. C. Steinhagen, M. G. Panthani, V. Akhavan, B. Goodfellow,B. Koo and B. A. Korgel, J. Am. Chem. Soc., 2009, 131, 12554.
11. S. C. Riha, B. A. Parkinson and A. L. Prieto, J. Am. Chem. Soc.,2009, 131, 12054.
12. P. Dai, X. Shen, Z. Lin, Z. Feng, H. Xu and J. Zhan, Chem.Commun., 2010, 46, 5749.
13. D. Pan, L. An, Z. Sun, W. Hou, Y. Yang, Z. Yang and Y. Lu,J. Am. Chem. Soc., 2008, 130, 5620.
14. Y. K. Jung, J. I. Kim and J.-K. Lee, J. Am. Chem. Soc., 2010,132, 178.
15. A. L. Efros and A. L. Efros, Sov. Phys. Semicond., 1982, 16, 772.
16. L. E. Brus, J. Chem. Phys., 1984, 80, 4403.

17. J. R. Lakowicz Principles of fluorescence spectroscopy, 2nd edn. Kluwer, New York (1999).

18. H. Sharma, S. N. Sharma, G. Singh, S. M. Shivaprasad, Colloid Polym Sci, **285**, 1213 (2007).

19. K.K. Nanda, S.N. Sahu, Adv. Mater. 13 (2001) 280.

20. I. Repins, M. A. Contreras, B. Egaas, C. DeHart, J. Scharf,C. L. Perkins, B. To and R.Noufi, Progr. Photovolt.: Res. Appl.,2008, 16, 235–239.

21. K. Ramanathan, G. Teeter, J. C. Keane and R. Noufi, ThinSolid Films, 2005, 480, 499–502.

22. C. Wadia, A. P. Alivisatos and D. M. Kammen, Environ. Sci.Technol., 2009, 43, 2072–2077.

23. B. A. Andersson, Prog. Photovoltaics, 2000, 8, 61–76.

24. H. Katagiri, Thin Solid Films, 2005, 480, 426–432.

25. J. S. Seol, S. Y. Lee, J. C. Lee, H. D. Nam and K. H. Kim, Sol.Energy Mater. Sol. Cells, 2003, 75, 155–162.

26. T. Todorov and D. B. Mitzi, Eur. J. Inorg. Chem., 2010, 17–28.

27. H. Katagiri, K. Jimbo, W. S. Maw, K. Oishi, M. Yamazaki,H. Araki and A. Takeuchi, Thin Solid Films, 2009, 517, 2455–2460.

28. M. G. Panthani, V. Akhavan, B. Goodfellow, J. P. Schmidtke,L. Dunn, A. Dodabalapur, P. F. Barbara and B. A. Korgel, J. Am.Chem. Soc., 2008, 130, 16770–16777.

29. Q. J. Guo, H. W. Hillhouse and R. Agrawal, J. Am. Chem. Soc.,2009, 131, 11672–11673.

30. P. C. Dai, X. N. Shen, Z. J. Lin, Z. Y. Feng, H. Xu and J. H. Zhan,Chem. Commun., 2010, 46, 5749–5751.

31. T. Kameyama, T. Osaki, K. Okazaki, T. Shibayama, A. Kudo,S. Kuwabata and T. Torimoto, J. Mater. Chem., 2010, 20,5319–5324.

32. Persson, J. Appl. Phys., 2010, 107, 053710.

33. S. C. Riha, B. A. Parkinson and A. L. Prieto, J. Am. Chem. Soc.,2009, 131, 12054–12055.

34. A. Shavel, J. Arbiol and A. Cabot, J. Am. Chem. Soc., 2010, 132,4514–4515.

35. A. Fischereder, T. Rath, W. Haas, H. Amenitsch, J. Albering,D. Meischler, S. Larissegger, M. Edler, R. Saf, F. Hofer and Trimmel, Chem. Mater., 2010, 22, 3399–3406.

36. D. C. Pan, L. J. An, Z. M. Sun, W. Hou, Y. Yang, Z. Z. Yang andY. F. Lu, J.Am. Chem. Soc., 2008, 130, 5620–5621.

37. Z. B. Zhuang, Q. Peng, B. Zhang and Y. D. Li, J. Am. Chem. Soc.,2008, 130, 10482–10484.

38. S. H. Choi, K. An, E. G. Kim, J. H. Yu, J. H. Kim and T. Hyeon,Adv. Funct. Mater., 2009, 19, 1645–1649.

39. R. G. Xie, M. Rutherford and X. G. Peng, J. Am. Chem. Soc.,2009, 131, 5691–5697.

.